2007

UNDERSTANDING AND OPTIMIZING THE HARLEY SURFACE EFFECT SHIP

Jeffrey C. Harris
University of Rhode Island, clark115@gmail.com

UNDERSTANDING AND OPTIMIZING THE HARLEY SURFACE EFFECT SHIP

BY

JEFFREY C. HARRIS

A THESIS SUBMITTED IN PARTIAL FULFILLMENT OF THE

REQUIREMENTS FOR THE DEGREE OF

MASTER OF SCIENCE

IN

OCEAN ENGINEERING

UNIVERSITY OF RHODE ISLAND

2007

MASTER OF SCIENCE THESIS

OF

JEFFREY C. HARRIS

APPROVED:

Thesis Committee:

Major Professor _____

_____

_____

_____

DEAN OF THE GRADUATE SCHOOL

UNIVERSITY OF RHODE ISLAND

2007

ABSTRACT

Calm water towing tank results completed in August 2002 for a 2.3 m Harley surface effect ship model, a seal-less, twin air cushion, catamaran design, are presented. Results are extrapolated to 25 and 100 m length scales. Separately, a boundary integral method is used to solve for fully nonlinear potential flow wave resistance of moving pressure patches. The resulting algebraic system is solved using a restarted version of GMRES combined with a fast multipole algorithm. The Dirichlet-Neumann boundary value problem is solved at each time step using a second-order Taylor series approximation of a mixed Eulerian-Lagrangian time integration. Twin pressure patches are used to approximate the Harley surface effect ship, and comparison with towing tank resistance tests are presented. The wetted surface area and wave resistance for each case are compared to experimentally estimated values.

ACKNOWLEDGMENTS

I would like to thank all who made this project possible, including, but definitely not limited to: Stéphan T. Grilli, my advisor, who kept me realistic and has worked on the BEM model for many years; Hong Gun Sung, the postdoc who developed the moving pressure patch version of the BEM code; the late John Hopkinson, who was president of VibTech, Inc., made this project possible, and helped fund my work for a year and a half; Aaron Bengston, who helped get me up to speed in the beginning; Larry Simoneau who provided occasional help with hardware; Howard Harley, the driving force behind the development of the Harley SES design, and of course the many others who helped along the way in smaller ways.

PREFACE

Advanced marine vehicles often require unique designs with many engineering challanges. These include planing hulls, hydrofoils, and hovercraft – each of which require specific changes to the hull, engines, and equipment that are not needed for a pure displacement monohull. Typically the efficiency of a high speed ship deteriorates at low speed. Such a hullform may also have special structural requirements. They may also have poor seakeeping in high seas.

By combining advantages of a displacement, planing, and surface effect ships (SESs), the Harley SES is an attempt to design an efficient platform for high speed sealift. This thesis was born out of an attempt to quantify the performance of this SES during the first stages of construction of a prototype, the 25 m (82 ft) *Gladius* in 2004. Because the prototype was never completed, very little information on the performance of this design, now a decade old, was published. At present, research on the design has all but stopped, although one may hope that with increasing interest in high speed ships, the Harley SES could be further developed. This thesis is a compilation of the best physical and numerical experiments and the resulting analysis conducted to date on the Harley concept.

Manuscript 1 covers experimental results from 2.3 m model resistance tests completed in August 2002 at the Institute for Marine Dynamics (IMD). The main interest is in recovering the hydrodynamic drag and quantifying the cushion airflow parameters during the tests. A secondary goal is to explain sensor glitches and excessive noise during some of these tests.

Manuscript 2 attempts to explain the hydrodynamic drag measured during the model testing. Using a 3-D fully nonlinear potential flow (FNPF) wave model and twin pressure patches appropriate to represent the Harley SES air cushions, the wavemaking drag is predicted. While this has not yet been developed into a design tool, these

predictions are compared to and help explain the results from Manuscript 1.

The appendix contains the towing tank test matrix and photos of the model tests as well as the *Gladius* prototype under construction.

TABLE OF CONTENTS

ABSTRACT ii

ACKNOWLEDGMENTS iii

PREFACE iv

TABLE OF CONTENTS vi

LIST OF TABLES ix

LIST OF FIGURES x

MANUSCRIPT

1 Transport efficiency of the Harley surface effect ship 1

1.1 Introduction 1

1.1.1 SES history 3

1.1.2 Harley patent 5

1.1.3 Previous studies 5

1.1.4 Objectives and Tasks 9

1.2 Background 10

1.2.1 Resistance components 10

1.2.2 Cushion airflow 15

1.2.3 Comparing ship performance 18

1.3 Methods 19

1.3.1 Tank setup 19

1.3.2 Model setup 24

Page

1.4 Results . . . 27

1.4.1 RPM tests . . . 27

1.4.2 Air drag tests . . . 29

1.4.3 Resistance tests . . . 30

1.5 Discussion . . . 37

1.5.1 Shallow water effects . . . 37

1.5.2 Wavemaking drag . . . 38

1.5.3 Prototype extrapolation . . . 40

1.6 Summary . . . 41

List of References . . . 42

2 On the wavemaking drag of a twin-cushion surface effect ship . . . 46

2.1 Introduction . . . 46

2.1.1 Harley SES: a case study . . . 47

2.1.2 Background . . . 49

2.2 Methodology . . . 53

2.2.1 Solving Laplace's equation . . . 54

2.2.2 Time-updating the free-surface . . . 59

2.2.3 Evaluation of integral properties . . . 64

2.3 Results . . . 65

2.4 Discussion . . . 71

2.4.1 Model spin-up . . . 71

2.4.2 Long-term stability . . . 78

2.4.3 Experimental comparison . . . 78

2.5 Summary 79

List of References 81

APPENDIX

Experimental information 87

A.1 IMD test matrix 87

A.2 Photos of IMD test setup 89

A.3 Photos of *Gladius* construction 106

BIBLIOGRAPHY 114

LIST OF TABLES

Table		Page
1	Scale factors in terms of length scale, λ.	14
2	Averaged (and tared) drag measurements (N).	31
3	Corrected mean drag measurements (N).	31
4	Selected inlet pressure measurements (in Pascals).	32
5	Selected trim measurements (in degrees).	33
6	Selected draft (at tow point) measurements (in mm).	33
7	Difference in air cushion gap (mm) underneath range finder between trial runs and at rest. Faulty measurements are marked as N/A.	34
8	Changes in free-surface elevation within the air cushion underneath the range finder (mm). Faulty measurements are marked as N/A.	35
9	Mean pressures (in Pa) tared records (and reference value) for resistance tests at 45 kg, 9 m/s, and 4140 RPM. The difference between the values is the measured pressure. Notice the inconsistencies between the tests, and even the reference values.	35
10	Estimated wavemaking drag (N) for 445 N displacement tests. Clearly additional data would be useful.	39
11	WSA (m^2) estimates for selected tests.	40
12	Estimated power requirements of the *Gladius*.	40
13	Main NWT parameters used for numerical test cases (dimensionless values)	66
14	Main dimensionless variables for moving pressure patches used for test cases.	67

LIST OF FIGURES

Figure		Page
1	Harley SES concept hullform, patented 1996.	6
2	16.8 m prototype of the HSC-SES.	8
3	Underwater view of Harley model during testing at SSPA [22].	9
4	Schematic view of a once proposed 25 m *Gladius* prototype of the HSC-SES.	11
5	Artist's depiction of possible 50 m HSC-SES.	12
6	Diagram of SES cushion leakage.	15
7	View of CAD drawing of HSC-SES demihull stern; note air gap.	16
8	View of CAD drawing of HSC-SES demihull bow; note air gaps on both sides.	17
9	Towing tank setup. Note the tubing for airflow from the carriage.	20
10	Schematic of tow setup at IMD; model was free to heave, pitch, and roll.	21
11	Air blower used for IMD tests.	22
12	View of an RPM test, with air ducts attached from forward side.	23
13	Schematic of air cushion dimensions on the 2.3 m HSC-SES model; the length of each air cushion is 149 cm with a beam of 23 cm; the separation between the two air cushions is approximately 23 cm. The waterline length, L_{WL}, is slightly greater than the length of the cushions. The cushion area is then 0.68 m^2.	25
14	Top view of sensor locations on the HSC-SES model at IMD; static pressure sensors p_a, p_b, p_c, and p_d measured air pressures within the cushions, whereas p_1 measured the pressure in the port cushion air inlet. The range finder measured the air gap R in the starboard cushion 107 cm from the stern.	25

Figure **Page**

15 Camera views around the hull during testing at IMD (view towards stern, top left; outside view, top right; view from cushion inlet, bottom left; between demihulls, bottom right). 26

16 Comparison of measured momentum drag, mean, standard deviation, and 95% confidence interval for the mean, with theoretical. Note that the airflow in the tests was either 0.28, 0.36, or 0.53 m^3/s. . . . 28

17 Tow force measured during air drag tests; mean, standard deviation, and 95% confidence interval for mean compared to curve-fit of 0.30 m^2 cross-sectional area. Because the mean of the measured air drag closely follows a quadratic fit with speed, the results seem credible. 29

18 Tow carriage speed measured during an 8 m/s air drag measurement. Notice the high frequency vibrations. 30

19 Definition of trim angle, θ, and draft at tow point, d_0. 32

20 Faulty range finder measurement during 29 kg, 6 m/s, 3000 RPM test, possibly due to water spray within the air cushion. Note that air cushion height over keel is 18 cm. 34

21 Tow carriage speed (U, m/s), fan speed (RPM), tow force (D_{meas}, N), trim (θ, ^{o}), and draft (d_0, mm) for 1.5 m/s, 1800 RPM (0.23 m^3/s) test. Notice the lack of vibrations when the air blower is off, even when the model is moving. 36

22 Hypothesized bow wave caused by supercritical flow conditions. 37

23 Schematic of free-surface caused by HSC-SES at a high speed, U; ΔR is the change in free-surface elevation. 39

24 Harley SES concept hullform, patented 1996. 48

25 Schematic of 3D-NWT of length X_0, width W_0, and depth H_0, moving at speed $U_B(t)$ with the specified free surface disturbance. 54

26 Definition of a 3D-MII element in Cartesian boundary coordinate system with indication of tangential and normal vectors at an arbitrary point., with : $(\circ)$ 4x4 overlapping element; $(\bullet)$ middle interval used in the integrations. 56

27 Parameters for twin moving pressure patch problem. 65

Figure **Page**

28 Evolution of free-surface for case 1 for t= 3.6, 7.2, and 10.8. 68

29 Evolution of free-surface for case 2 for t= 2.4, 4.8, and 7.2. 69

30 Evolution of free-surface for case 3 for t= 1.8, 3.6 and 5.4. 70

31 Quasi-steady free-surface established after 300 timesteps for each case (for t= 18, 12, and 9, respectively). 72

32 Wave resistance coefficient for each test case. 73

33 Close-up of instabilities for the last three timesteps (339–341) of case 1. 74

34 Kinetic energy of NWT for each test case. Note the instability in case 1 at the end of the test run. 75

35 Potential energy of NWT for each test case. Note the instability in case 1 at the end of the test run. 76

36 Relative volume change to NWT for each test case (i.e., ratio of difference in NWT volume from initial conditions to the initial NWT volume). 77

37 Comparison of quasi-steady state NWT free-surface elevation (z) within starboard pressure patch with experimentally measured water surface wave height (at $x = 5.0$) for cases 1–3. Notice the coarseness of the discretization. 80

MANUSCRIPT 1

Transport efficiency of the Harley surface effect ship

1.1 Introduction

In recent years there has been broad interest in high speed ships, not only for special purpose military craft, but also for passenger ferries and commercial sealift [1]. One of the most promising hullforms for high speeds is the Surface Effect Ship (SES). This manuscript details current knowledge about one such vessel.

SES designs have been in existance since 1960 [2] and, essentially are a more efficient, specialized version of a hovercraft used for traveling over water. SES designs are among the most efficient vessels at high Froude numbers; with a very shallow draft, the wavemaking drag is low, yet unlike dynamically supported craft such as hydrofoils, an SES also has a small wetted surface area (WSA) and therefore a low friction drag. The disadvantage is that a SES does require extra power, weight, and machinery to operate the lift fans generating the airflow in the cushions. Typically between 10 and 50% of the displacement of an SES is due to payload (e.g., cargo), which is less than what is typically obtainable for a large cargo ship of around 70 to 80% [3].

A standard SES design consists of a single rectangular pressure patch, contained by two slender sidehulls and fore and aft flexible seals [4]. This so-called air cushion is a region of nearly uniform air pressure which is actively created by a number of lift fans. Air leaks out underneath the fore and aft seals. While the hydrodynamic resistance of the sidehulls will be higher than that of a hovercraft and the hull geometry is more complicated, the decreased air leakage area can provide for an increase in overall efficiency.

Aerostatic lift is potentially one of the most efficient forms of sealift possible. At high speeds, skin friction is the greatest source of power consumption for a ship. This has resulted in basic research into how air lubrication of the water within a hull's bound-

ary layer may reduce frictional drag [5, 6]. Hydrostatic and hydrodynamic lift (e.g., hydroplaning) inherently require the existence of wetted surface area over which friction occurs, which means that there is a limit to how much lift is physically possible for a given speed and engine power. Aerostatic lift has no such limitation, since pressure is applied to the water surface without physically touching the hull. At very high speeds, frictional drag is the dominant form of resistance, and limiting the wetted surface area to the sidehulls and seals is highly advantageous.

Despite these potential advantages, SES hullforms have been used for only a few large vessels. This is partly due to the significant dead weight and power requirements for the lift fan engines. Often lightweight construction is required for SES designs to be practical. Historically this meant using aluminum (e.g., for the SES-100B [3]), but more recently high performance composite materials have been considered. Air blowers spin at such high speeds that water droplets can cause damage to the fan blades, and so they are prone to break down. Another factor is the complexity of the skirt or flexible seal systems featured in most designs; predicting the drag caused by such seals is difficult because of their nonlinear response [7]. They wear out and may cause resonant vibrations in the air cushion. While the cobblestone effect, which is an unwanted motion of an SES caused by a Helmholtz resonance of the air cushion itself [4], can occur for any SES, seals can also vibrate themselves, which is a phenomenon known as skirt bounce [8].

Few seal-less SES designs have been proposed, and their optimum design is unknown. Within a few years of the construction of the first SES, seals were added to reduce air leakage. A traditional SES may have only the simplest of sidehulls, relying heavily on the forward skirt for smoothly traveling over waves, whereas with a seal-less design, the hull itself must accomodate the possibility of incoming waves, while minimizing air leakage areas and without being detrimental to the overall performance.

While traditional SESs are understood well enough that current research focuses on the more difficult time-dependent cases of seakeeping and ride-control (e.g., by Bertin [9]), this paper will deal with only the calm water drag prediction for a new SES design. Examples of seal-less SES include the SeaCoaster hullform developed by Don Burg of Air Ride Inc. of Miami, Florida, and the Russian river craft known as Linda from the Zelenodolsk Shipyard in Russia [1]. Another seal-less design is the Harley SES, which is the focus of the remainder of this paper.

1.1.1 SES history

The SES concept was invented in 1960 by Allen Ford [2]. Since then, similar designs have been proposed which feature lift fans that pressurize the air underneath the rigid hull of a ship, to create an air cushion that provides lift (e.g., air cushion vehicles, captured air bubbles). Each design has a slightly different way of pressurizing the air cushions and minimizing air leakage.

Almost immediately, there was a discussion of large scale, high speed, long range SES designs [10]. The U.S. Navy conducted an extensive research program in the 1970s to develop larger and faster SESs, resulting in several testships, most notably the SES-100A and the SES-100B [3], as well as the XR-1 and the XR-5 [4]. Notable air cushion crafts were also developed in Canada, France, Germany, Japan, the United Kingdom, and the USSR at that time. While skirt development, particularly in the related air cushion vehicles, continues today [8], the wavemaking and frictional drag for a SES are similar enough that a nearly formulaic design procedure could be produced from early SES development [11], depending on design parameters. However, sidehull designs have remained fairly simple and some research which did concern advanced sidehull designs was classified [4].

In 1979, the U.S. Navy SES devlopment was severely affected when the 3K-SES project (a 3000 ton, 80-knot design) was canceled. Research for military and commer-

cial use since then has mainly been centered in Europe and Asia. For instance, there was a substantial SES development program in Germany [12, 13], the Japanese government funded *Hisho* in 1994 [1], a 170-m demonstrator aimed at developing a new high speed sealift platform, and the Royal Norweigen Navy commissioned *KNM Skjold* in 1999, a SES designed to be a fast patrol craft.

U.S. Navy SES design research changed in the 1980s, with the Surface Ship Continuing Concept Formulation (CONFORM) Program [14] studying the surface effect catamaran (SECAT) concept [15]. The SECAT design was essentially two air cushions placed side-by-side (a catamaran), connected by a bridging structure. The project included both theoretical studies into the wavemaking resistance [16, 17], as well as measurements with a 33-ft prototype that was constructed [18]. The SECAT required many fans, not only to pressurize the air cushion, but also to pressurize the seal bags (used in one type of seal design) [16]. As such, it was much more complicated than the HSC-SES. The advantage of the SECAT over other designs at the time was that two high L/B air cushions have much lower wave resistance than a single low L/B air cushion, while maintaining the roll stability and high structural height. The hard-structure clearance of a SES can be taken as a rough estimate of the significant wave height of the seas the vessel can handle [15].

This is by no means a complete overview of SES investigations. There are many good references on SES studies, design, and technology, with substantial overviews by Mantle [4] and Yun and Bliault [7]. Numerical studies of moving pressure patch drag are also a classic problem, which most notably was studied by Doctors and Sharma [19]. Currently work is centered more on SES seakeeping from both a numerical and experimental side, such as ride control systems for dealing with the cobblestone effect [9].

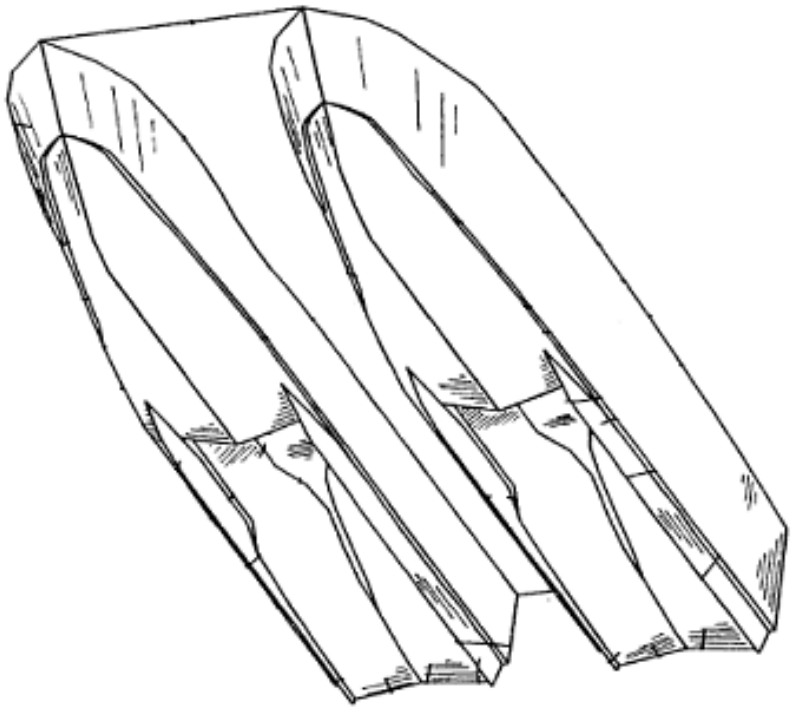

Figure 1. Harley SES concept hullform, patented 1996.

1.1.2 Harley patent

The Harley SES was proposed by Howard Harley of Harley Shipbuilding Corporation (HSC) of Bartow, Florida, and was patented in 1996. The HSC-SES, as it is referred to in this paper, is a catamaran with rigid hulls having two air cavities (i.e., cushions), each pressurized from airflow inlets at the bow. Each demihull of the ship consists of a deep-V bow with a step separating it from the air cushion, a lift fan at the bow which forces pressurized air into the air cushion, two thin sidehulls or fins which contain the air cushion, and an inverted-V transom stern (Fig. 1) [20].

Although HSC built several large scale models, including 26- and 65-ft prototypes and a fast ferry, further development and refinement of the Harley design has mainly been conducted by Ocean Dynamics Inc., a former collaboration of HSC and Vibtech Inc., of Wickford, Rhode Island. As a result, several design changes were made

to the relative dimensions of the hull, particularly in regards to the cushions, since the initial patent. It is currently thought that the optimal spacing between the demihulls is equal to their width, with air cushions having a length-beam (L/B) ratio 6.5 and extending from the SES stern to a point 65% of the way to the bow (i.e., 65% of the length overall).

1.1.3 Previous studies

Initial studies were conducted by Howard Harley in the 1990s using over 40 2.3 m (7.5 ft) composite models being towed on a lake, using a load cell to measure total drag. No airflow measurements were made, but it was noticed that unless some dynamic lift is included (e.g., deep-V bows for planing lift), the efficiency of the design for large displacements was limited. This finding may imply that the draft towards the bow needs to be small enough for the seal-less air cushion to act efficiently. Various towing tank tests were then conducted at Stevens Institute at this point.

In the next phase, 7.9 m (26 ft) and 16.8 m (55 ft) prototypes were built in 2001–2, as well as several small ferries for commercial use. The 7.9 m design had a 3.0 m (10 ft) beam, substantially wider than any later design, and reached 27 m/s (52 kts) with a 115 hp outboard motor and 1724 kg (3800 lb) displacement. The 16.8 m prototype, with 985 kW (1320 hp) propulsion and a 112 kW (150 hp) blower reached 23 m/s (45 kts) at a displacement of 7.98 tons [21]. The air cushions covered only 50% of the hulls' length at this point. The latter craft was later extended to 19.8 m (65 ft) and larger engines installed, reaching more than 31 m/s (60 kts) during trials. Unfortunately, since none of these vessels have the same relative dimensions (i.e., are geosims), such as the aspect ratio of the air cushions, it is difficult to assimilate and compare this information.

Latorre et al. [21] studied a microbubble drag reduction (MBDR) scheme, both during towing tank tests of a 2.3 m HSC-SES model at the NASA/Langley seawater tank, and full-scale trials of the 16.8 m prototype (Fig. 2). This showed that drag reductions of

Figure 2. 16.8 m prototype of the HSC-SES.

5–15% was possible by injecting air bubbles along the sidehulls. This study also has the first estimate of wetted surface area (WSA) of the boat at speed. Unfortunately, scaling laws appropriate to the physics of microbubble drag reduction are not well understood.

Other tests were conducted at SSPA in Sweden, initially in 2001 [22], which most notably included an underwater photograph of the Harley design, which shows the typical wetted areas of the hull (Fig. 3). The photo also shows air bubbles that seem to be entrained at the bow; these could reduce the frictional drag of the hull, even without the active production of air bubbles used by Latorre et al. Allenström et al. (2001) referred to the design as an Air Lifted Catamaran (ALC), or Skirtless SES, which they are independently developing. The most recently published work on this hullform was conducted by the same research group in 2004 [23]. Despite their access to data on these hullforms at multiple length scales, their presentation of the physical aspects is still questionable; they appear to estimate the drag for two air cushions as twice the drag of one cushion, rather than considering the interaction between the two (in fact, they

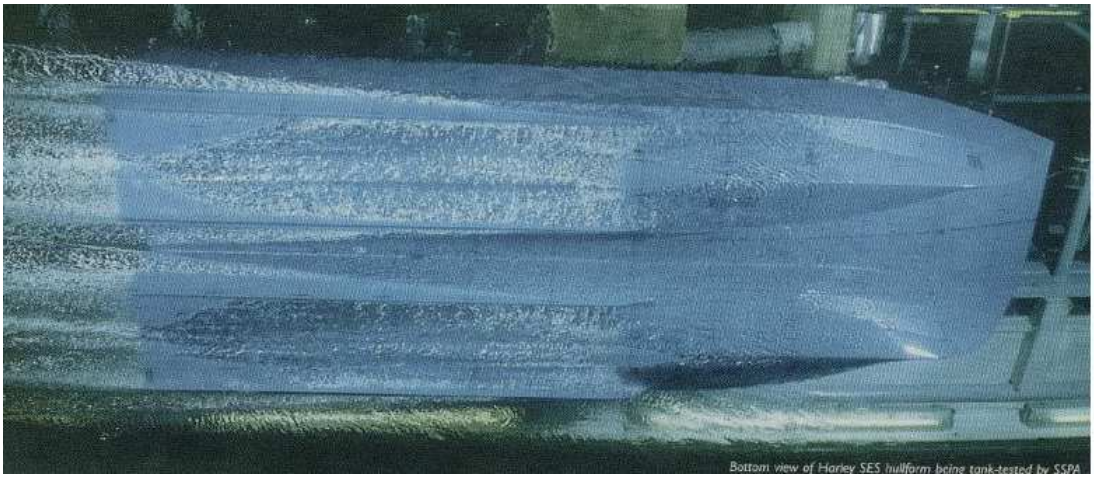

Figure 3. Underwater view of Harley model during testing at SSPA [22].

comment that their wavemaking drag estimate seems too high).

Other studies focused on applications of the HSC-SES; because the hullform has a shallow draft, a full-scale prototype should be able to approach an undeveloped shoreline (i.e., an adverse port situation) much more easily than a typical cargo ship. To this effect, Vibtech proposed using a Rapidly Deployable Causeway System (RDCS) to be stowed onboard the ship. Both experimental [24] and numerical [25] tests were performed on this design.

Unfortunately, the majority of the tests performed on the HSC-SES are poorley documented. Notably the WSA still cannot be clearly estimated, and airflow to the cushions was never precisely measured. The purpose of resistance tests is to determine the power necessary to achieve desired speed at a given displacement, and part of this power is the power required to produce the airflow to the air cushions. If the airflow is poorly known in either the models or the prototypes, then this could result in either too optimistic or pessimistic estimates of the powering requirements of a full-scale HSC-SES.

1.1.4 Objectives and Tasks

The most controlled tests so far were conducted at the Institute for Marine Dynamics (IMD, now Institute for Ocean Technology) in 2002. The present work is an analysis of the data obtained during those tests. In particular, based on proper scaling laws, a procedure is developed to predict the performance of full-scale HSC-SES prototypes (Fig. 4, 5). This is motivated because of prototype construction in the past few years, most recently the 25 m (82 ft) *Gladius*, which was partially completed at HSC in 2005 before funding expired. *Gladius* was supposed to achieve a speed of 31 m/s (60 kts), with 3730 kW (5000 hp) installed for propulsion and lift fan powering and would have a total displacement of 60 MT, with a payload fraction of around 50%. *Gladius* was designed to have a height between its keel and the top of its superstructure of 4.9 m.

The main problems faced involve dividing the measured resistance during tests into wavemaking and frictional drag. While the wavemaking drag of moving pressure patches is well understood, the exact pressure distribution is not. While frictional drag is well understood, the WSA was not measured at speed. Other corrections such as air drag and momentum drag are also important factors that are discussed. Because the WSA was not measured during the IMD tests, extrapolating the results to full-scale are made using crude estimates of wavemaking drag. While more tests with more realistic parameters are undoubtably needed to understand the full-scale performance of the HSC-SES, this manuscript covers much of what is quantitatively known.

1.2 Background

SES development so far has been a broad range of full-scale designs, model testing, and theoretical estimates. What follows is a brief summary of the theory relevant to the HSC-SES.

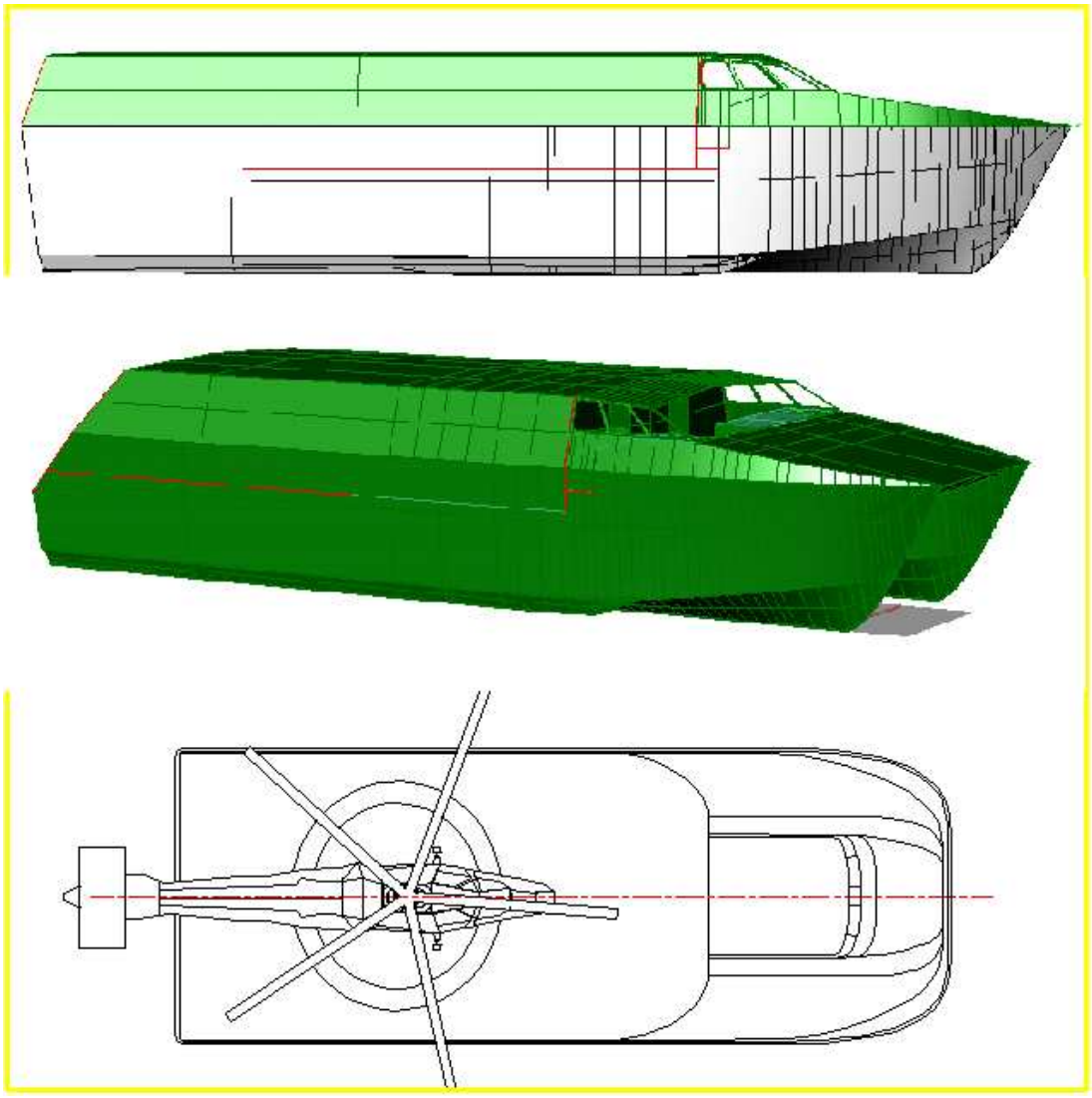

Figure 4. Schematic view of a once proposed 25 m *Gladius* prototype of the HSC-SES.

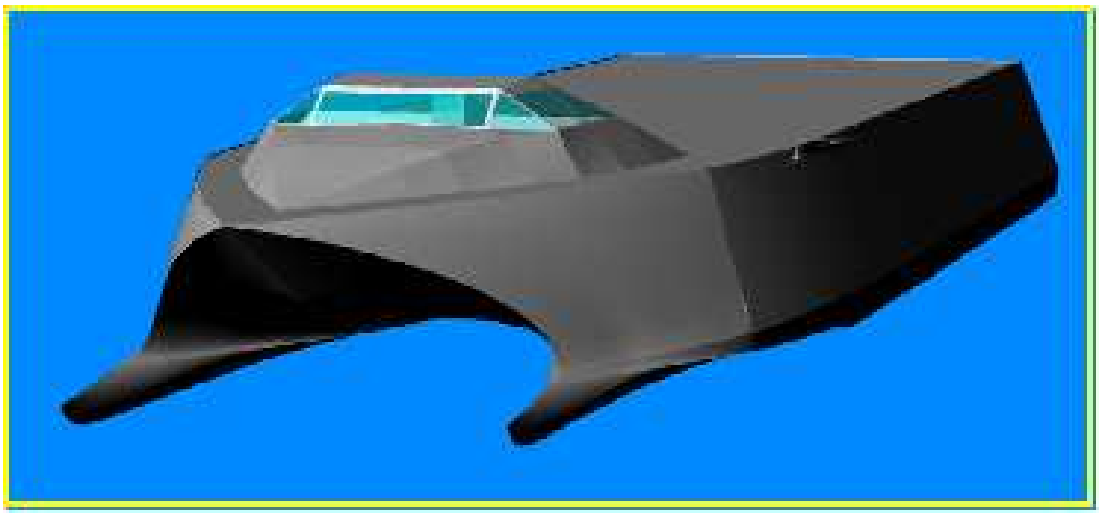

Figure 5. Artist's depiction of possible 50 m HSC-SES.

1.2.1 Resistance components

For practical purposes the total calm water resistance for a seal-less SES, D_T, can be considered the sum of different resistance components:

$$D_T = D_F + D_A + D_M + D_R \tag{1}$$

where D_F is frictional drag, D_A is air drag, D_M is momentum drag, and D_R is residual drag.

For SESs traveling at a given speed U through water of density ρ, frictional drag is estimated using a measurement of the wetted surface area (WSA), S_W, and using the ITTC-1957 model-ship correlation line [26] to determine the frictional drag coefficient, C_F:

$$D_F = \frac{1}{2} C_F \rho S_W U^2 \tag{2}$$

$$C_F = \frac{0.075}{(\log_{10} R_n - 2)^2} \tag{3}$$

$$R_n = \frac{U L_{WL}}{\nu} \tag{4}$$

where R_n is the Reynolds number, dependent on U, the waterline length of the ship, L_{WL}, and the viscosity of the water, ν.

Air drag is ideally estimated from the air drag coefficient, C_A, and cross-sectional area, S_A, as

$$D_A = \frac{1}{2} C_A \rho_a S_A U^2 \tag{5}$$

where ρ_a is the air density, but often, especially in towing tank measurements, this needs to be measured directly, instead. Measuring the air drag can be done in a wind tunnel, but another typical, but less accurate, procedure is to tow the model while lifted slightly out of the water, and then measuring the so-called tow force.

Momentum drag is caused by the lift fans on an SES; momentum is imparted onto the air that is forced into the air cushions by bringing the speed of that air to the same speed as the ship. For a given fan inlet area of A_i with airflow Q, this is equal to:

$$D_M = Q A_i U \tag{6}$$

though in some cases this drag is offset by the fact that there is a similar momentum thrust caused by air leaking from the air cushions. For model tests, this too can be measured, since the fan setup could be entirely different than it would be on an intended ship design.

After subtracting these drag components from the total drag, the residual drag (e.g., wavemaking drag, form drag) is dependent on the water's surface generated by the moving ship, which in turn is dependent on the nondimensional Froude number

$$F_n = \frac{U}{\sqrt{g L_{WL}}}. \tag{7}$$

Full-scale ship resistance for a given Froude number can be extrapolated by choosing a geometrically similar model (i.e., a geosim) and seeing what the drag is for that model at the same Froude number. For a length scale factor λ, WSA scales as λ^2, speeds scale as $\lambda^{0.5}$, etc. (Table 1). Then, after separately computing the frictional, aerodynamic, and momentum drags for the full-scale ship, the residual resistance Froude scales as well, as

Quantity	Scale	Quantity	Scale
Length	λ	Power	$\lambda^{3.5}$
Speed	$\lambda^{0.5}$	Displacement	λ^3
Area	λ^2	Force	λ^3
Pressure	λ	Airflow	$\lambda^{2.5}$

Table 1. Scale factors in terms of length scale, λ.

λ^3. The resistance must be split up into its separate components, because the frictional drag is affected by the Reynolds number, and the aerodynamic and momentum drags can be entirely different for a model, because often the ship superstructure is not reproduced at model scale for convenience.

Because residual resistance for an SES is almost entirely due to wavemaking resistance, and nearly all of this wavemaking resistance is due to the moving pressure patch (due to the pressurized air cushions), wavemaking resistance caused by moving pressure patches has been extensively studied (e.g., Doctors and Sharma [19], Tuck et al. [27]). There has been some study of twin cushion wave resistance, as well [16]. Note that wavemaking resistance is greatest at the so-called wavemaking hump, at a length Froude number typically between 0.5 and 1.0.

While ship geometry and drag forces can be extrapolated from one size to another, the center of gravity (i.e., lcg) is also important. Notice that because the air and momentum resistances can be vastly different for a model as opposed to a full-scale prototype, the trim angle is actually the variable which is constant between the two cases, and the effective lcg can be different than the actual, depending on the moments imposed on the model (e.g., a model with large air drag could have a larger trim angle than a prototype with a streamlined superstructure for the same lcg; the two would have different effective lcgs). Similar things are important for full-scale tests as well, such as the location and angle of the propulsion system.

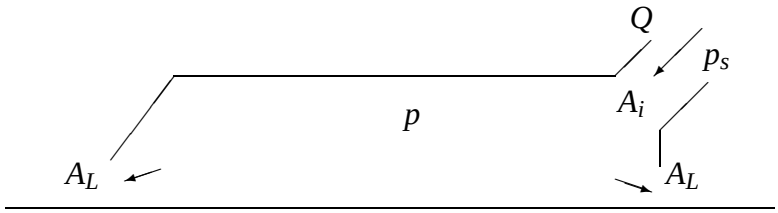

Figure 6. Diagram of SES cushion leakage.

1.2.2 Cushion airflow

While there have been several theories concerning air leakage from different types of air cushion vehicles [4], generally the steady-state airflow within an air cushion is rather simple; Bernoulli's equation can be used to find the relationship between the cushion pressure, airflow, and leakage area.

Using Bernoulli's equation, it is very important to note the difference between total, static, and dynamic pressure. Ignoring frictional losses (which is not always a valid assumption), the total pressure, p, within a cushion is constant and is the sum of the static and dynamic pressures:

$$p = p_s + \frac{1}{2}\rho_a v^2 \tag{8}$$

where p_s is the static pressure at a given point, and v is the air velocity at the same point; $\frac{1}{2}\rho_A v^2$ is the dynamic pressure. So if airflow Q is provided to an air cushion through an inlet of area A_i, the total pressure is given by

$$p = p_s + \frac{1}{2}\rho_a \frac{Q^2}{A_i^2} \tag{9}$$

where p_s is the static pressure in the air cushion inlet (Fig. 6).

A result of this, knowing that the static pressure outside of an air cushion is zero (compared to atmospheric pressure), the airflow is given by

$$Q = c_D A_L \sqrt{\frac{2p}{\rho_a}} \tag{10}$$

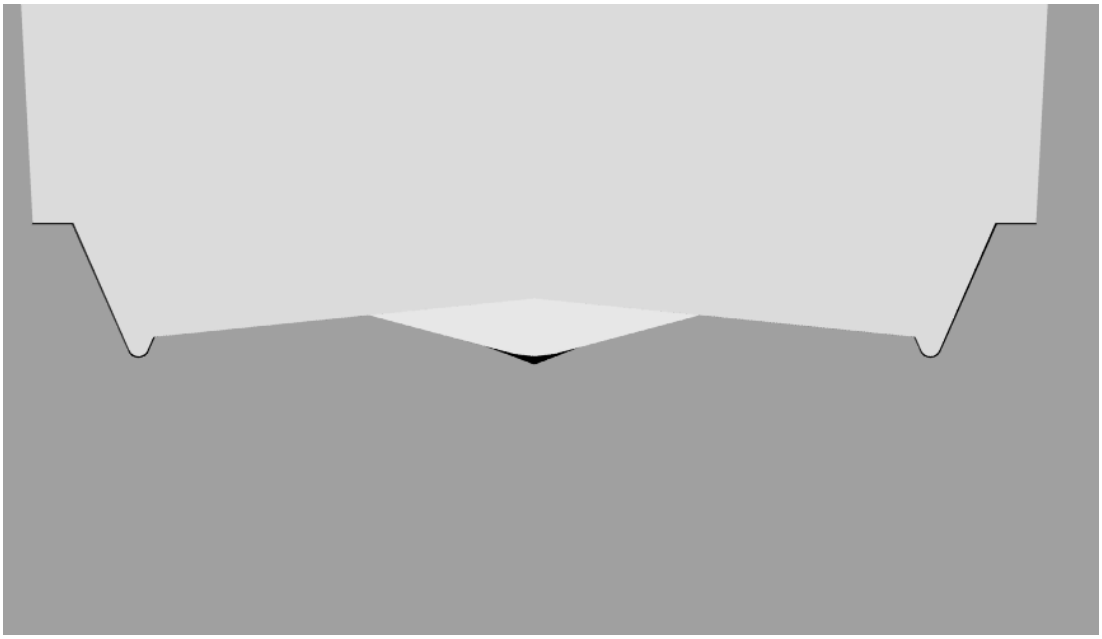

Figure 7. View of CAD drawing of HSC-SES demihull stern; note air gap.

where c_D is a discharge coefficient [28], and A_L is a leakage area. This discharge coefficient is required as a correction because the air leaving an opening such as an SES cushion will typically contract, so the effective leakage area is less than provided by a geometric calculation (e.g., air gap height times length of seals around air cushion). The discharge coefficient is thus some number between zero and one. For a typical SES, this discharge coefficient is 0.6. For a more streamlined flow like the flow out the stern of the HSC-SES, a discharge coefficient closer to 1.0 would be expected (Fig. 7). It would be more difficult to estimate a discharge coefficient or leakage area for the bow (Fig. 8).

There are a number of other ways to define the important parameters concerning airflow within the cushions; sometimes the cushion density (the ratio of the total cushion pressure to cushion length) is used; other times the flow coefficient, Q/US_C, for a cushion area S_C.

Because the leakage area has a generally unknown and varying value, the nondimensional airflow coefficient is instead based on the cushion area, S_C. The airflow

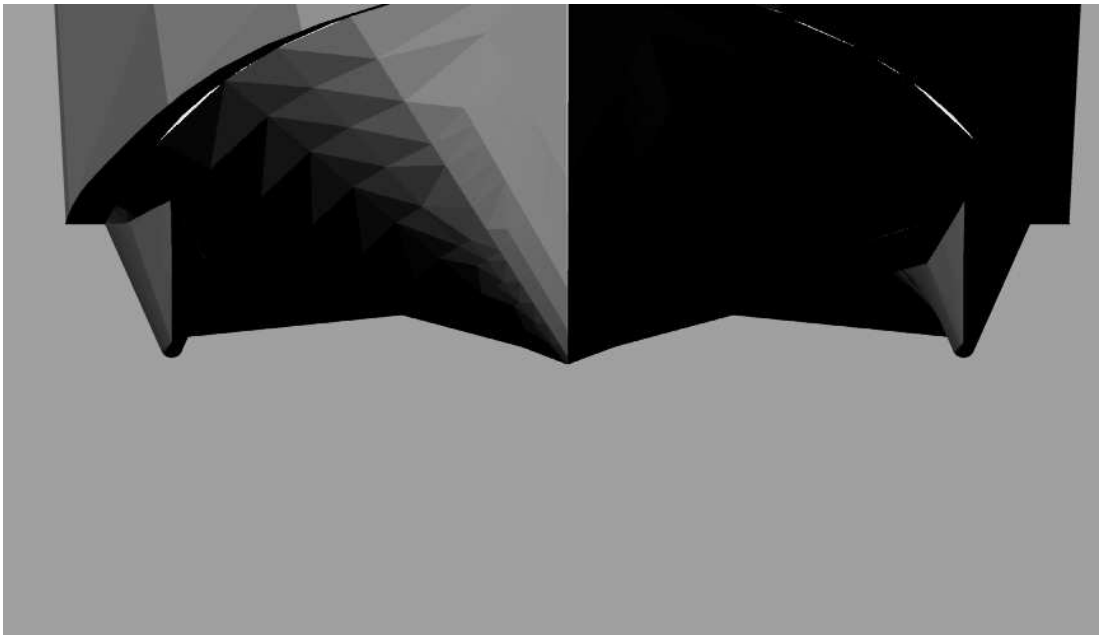

Figure 8. View of CAD drawing of HSC-SES demihull bow; note air gaps on both sides.

coefficient,

$$\bar{Q} = \frac{Q}{S_C \sqrt{2P/\rho_a}} \tag{11}$$

is a function of the cushion area, S_C, and P, the cushion total pressure. For an SES on calm water, $\bar{Q}$ is typically between 0.005 and 0.010, and preliminary design should start by assuming that $\bar{Q}$ is 0.005 [7].

Notice that for steady-state airflow, cushion parameters Froude scale. However, many aspects of air cushion dynamics do not Froude scale (e.g., cushion stiffness) [28].

1.2.3 Comparing ship performance

In order to then compare the performance of different ships, a nondimensional parameter known as the transport factor or transport efficiency, e_T, is used:

$$e_T = \frac{WU}{P} \tag{12}$$

where W is the displacement of the vessel, and P is the total power used by the vehicle. This is also known as the effective lift-to-drag ratio, because when neglecting power

loss due to the engine, transmission, and propulsion system, they are equivalent. For an SES, though, power consumption is not only due to the propulsion system, P_P, but also because of the lift fans, P_L:

$$e_T = \frac{WU}{P_P + P_L} \tag{13}$$

While supplying more airflow to the cushions of an SES will always decrease drag, eventually the added power required for the lift fans will be more than the decrease in propulsion power; there is an optimum amount of airflow, which was mentioned previously.

The most notable study of the relationship transport efficiency versus speed for all vehicles was published by von Karman and Gabrielli (1950) citekarman50. Most displacement ships operate at high transport efficiencies, between 10 and 100 (or higher, for large cargo ships), at Froude numbers below 1.0 [3]. Planing hulls are more efficient at higher speeds, but operate at lower transport efficiencies, between 1 and 10. SES hullforms tend to achieve transport efficiencies between 5 and 10 at these same speeds.

There have been studies of the performance of state-of-the-art ships. Typically these focus on the relationship between the transport efficiency and the volume Froude number, which depends on the ship displacement instead of length:

$$F_\nabla = \frac{U}{\sqrt{g\nabla^{1/3}}}. \tag{14}$$

where ∇ is the ship volume. Tests so far for the HSC-SES have focused on volume Froude numbers between 3 and 4, corresponding roughly to state-of-the-art transport efficiencies between 25 and 15, respectively [1].

The transport efficiency of a craft is directly proportional to its range, R, a relation known from classical physics as the Breguet range equation [29]:

$$R = \frac{e_T}{f} \log \frac{W}{W - W_{\text{fuel}}} \tag{15}$$

where f is the specific fuel consumption of the engine, and W_{fuel} is the displacement of the ship due to the fuel consumed. The projected near-term specific fuel consumption for a medium-speed diesel engine is 0.18 kg/(kW-hr) (0.29 lbf/(hp-hr)) or 4.80×10^{-3} km^{-1} [30]; current engines, depending on the load conditions, could be slightly higher.

1.3 Methods

The IMD towing tank test data mainly was used for analyzing the changes in hydrodynamic drag with increasing cushion airflow. Crude estimates of WSA were used to extrapolate performance to larger scales. Secondary analyses consisted of analyzing the magnitude of the oscillations in the pressure measured within the cushions.

1.3.1 Tank setup

A 2.3 m HSC-SES model (Fig. 9) was used for towing tank tests at the Clearwater tank of IMD, which has a total length of 200 m, a 12 m width, and a 7 m water depth (Fig. 10). The air blower was positioned on the tow carriage and air ducts connected the air blower to the air cushion inlets on the model (Fig. 11). The model was free to heave, pitch and roll.

The Clearwater tank is a freshwater tank; while the water temperature was not recorded, it is assumed to be 15 degrees Celsius. The tank is limited to a top speed of 9 m/s and tow forces of $\pm$250 N. No turbulence stimulation was used, but for nearly all tests, the Reynolds number was greater than 5×10^6 (the slowests tests at 2 and 4 m/s corresponded to Reynolds numbers of 2.6×10^6 and 5.2×10^6, respectively). While the waterline length (which determines the Reynolds number and thus the frictional drag coefficient) was not measured directly, observations indicated that it is roughly equal to the length of the air cushions, or 1.5 m, 65% of the length overall.

The depth of a towing tank becomes significant (i.e., deep-water assumption be-

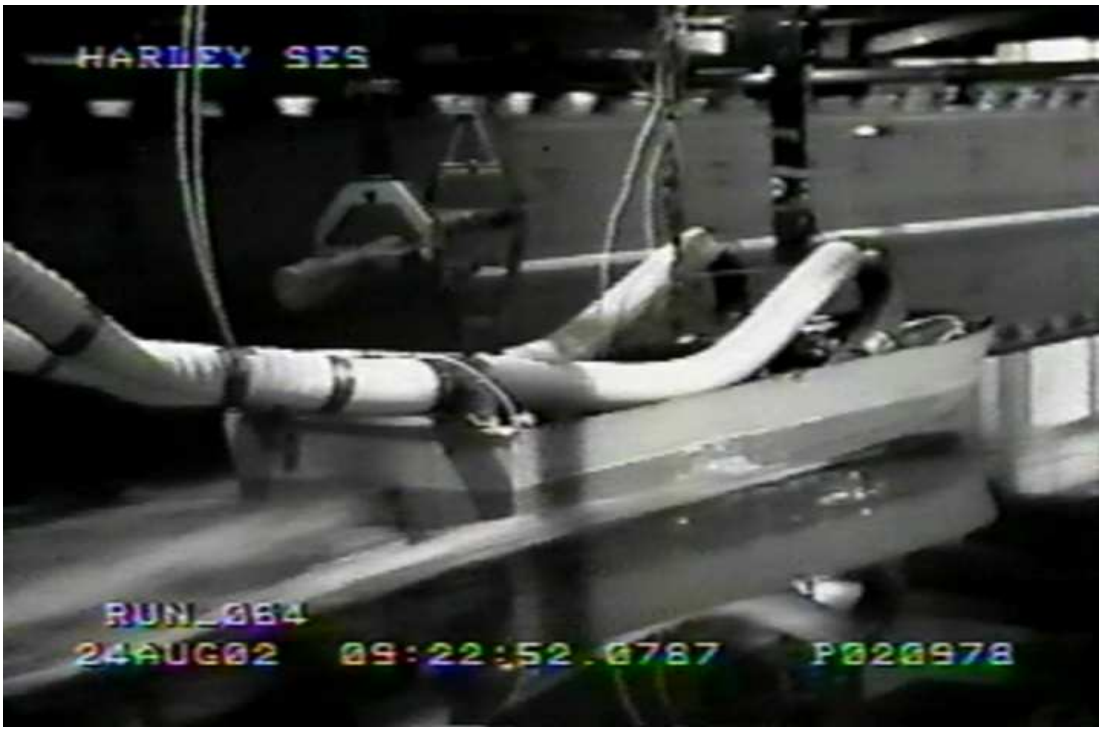

Figure 9. Towing tank setup. Note the tubing for airflow from the carriage.

comes invalid) for speeds around and above the critical speed, $\sqrt{gh}$, where h is the water depth, which is 8.3 m/s. Nondimensionally, the critical speed is reached when the depth Froude number, $F_d = U/\sqrt{gh}$, is 1.0.

The test matrix was principally focused on measuring resistance at test speeds of 2, 4, 6, 8, and 9 m/s, displacements of 29, 36, and 45 kg, and three different fan speeds (2400, 3000, and 4140 rpm). Because of the pressure losses within the air ducts between the air blower and air cushions, these fan speeds corresponded to near-constant airflow conditions of 0.28, 0.36, and 0.53 m^3/s. Airflow was determined by using fan vendor data and the average measured fan outlet pressure. The displacement was set with lead weights, and the lcg of the model was set to approximately 78 cm (31 in.) from the stern for all tests considered in this manuscript.

Three types of test runs were conducted: tests at zero forward speed with the air blower running at different speeds (RPM tests) to understand the momentum drag of the

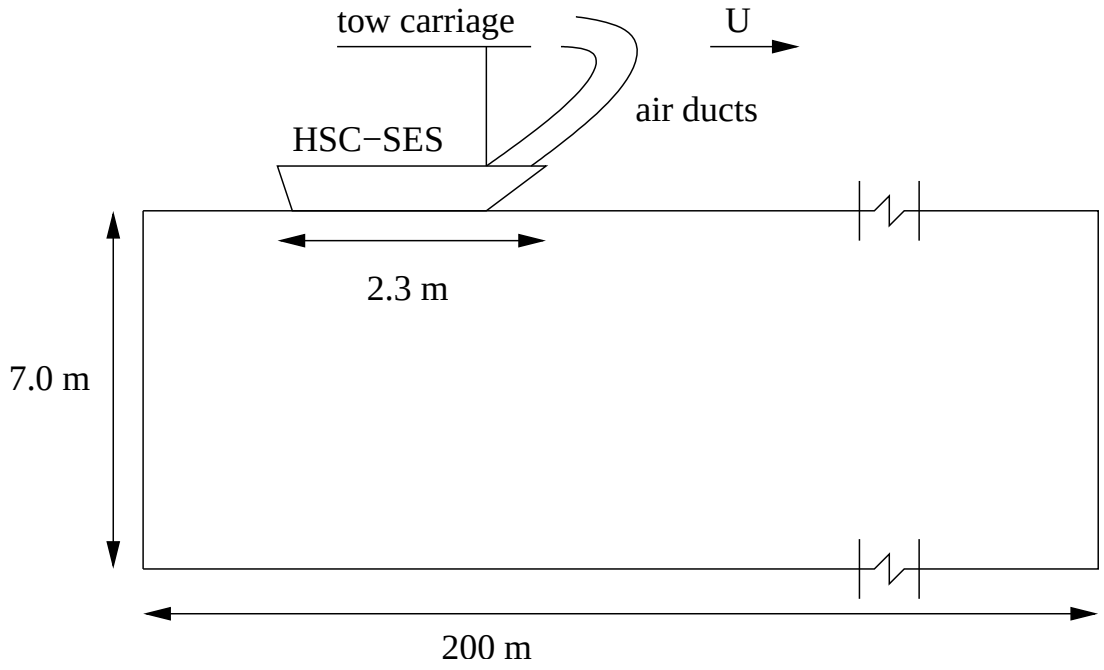

Figure 10. Schematic of tow setup at IMD; model was free to heave, pitch, and roll.

model setup (Fig. 12), resistance tests with the air blower running and at various speeds and displacements, and air drag tests with the model towed about 10 cm (4 in.) above the water surface.

1.3.2 Model setup

The 2.3 m HSC-SES model had a beam of 75 cm and was instrumented with a variety of pressure sensors to measure the air pressure wihin the air cushions and the air cushion inlets, a high frequency acoustic range finder to measure the air gap within the starboard air cushion at one point, and accelerometers to measure the surge and heave accelerations at the tow point (Fig. 14). All sensors were recorded at a sampling frequency of 50 Hz. Video cameras observing the sidehulls were unable to provide useful information about the WSA of the model (Fig. 15).

Each cushion was 1.5 m long and roughly 23 cm wide (Fig. 13), so the cushion area S_c was 0.68 m^2. The cushion inlets which attached to the air ducts were 10.8 cm in

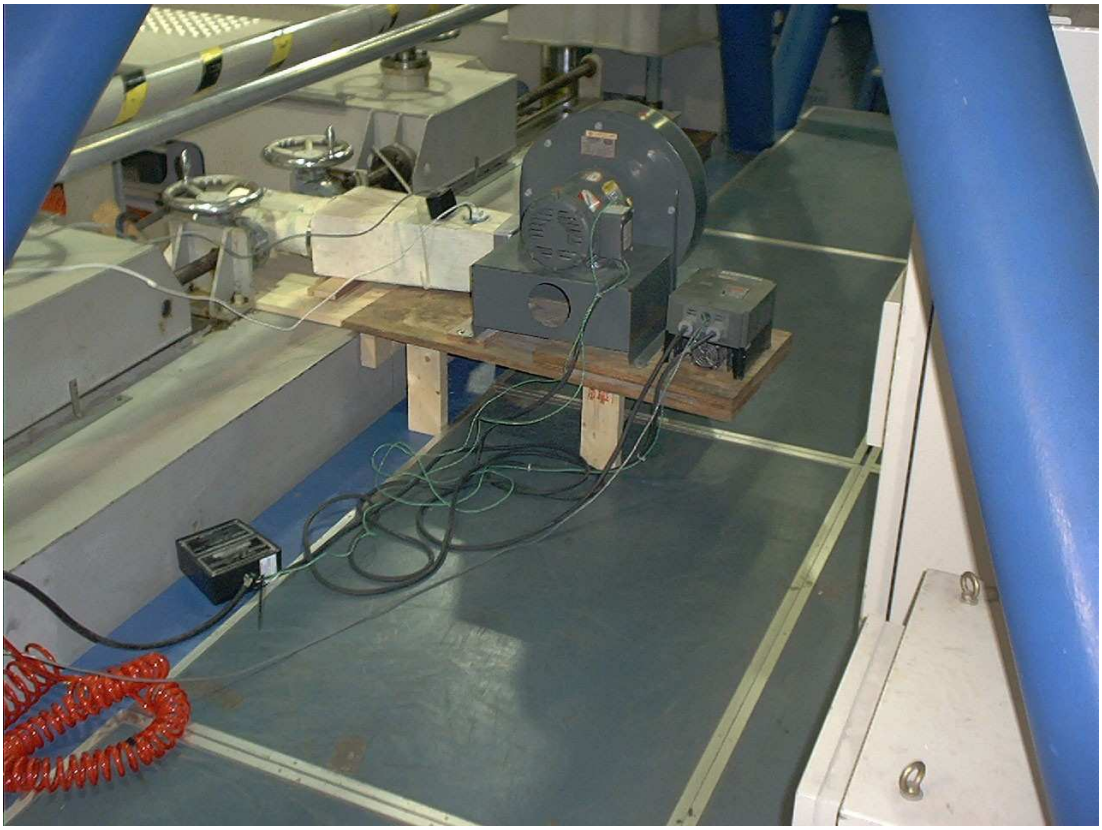

Figure 11. Air blower used for IMD tests.

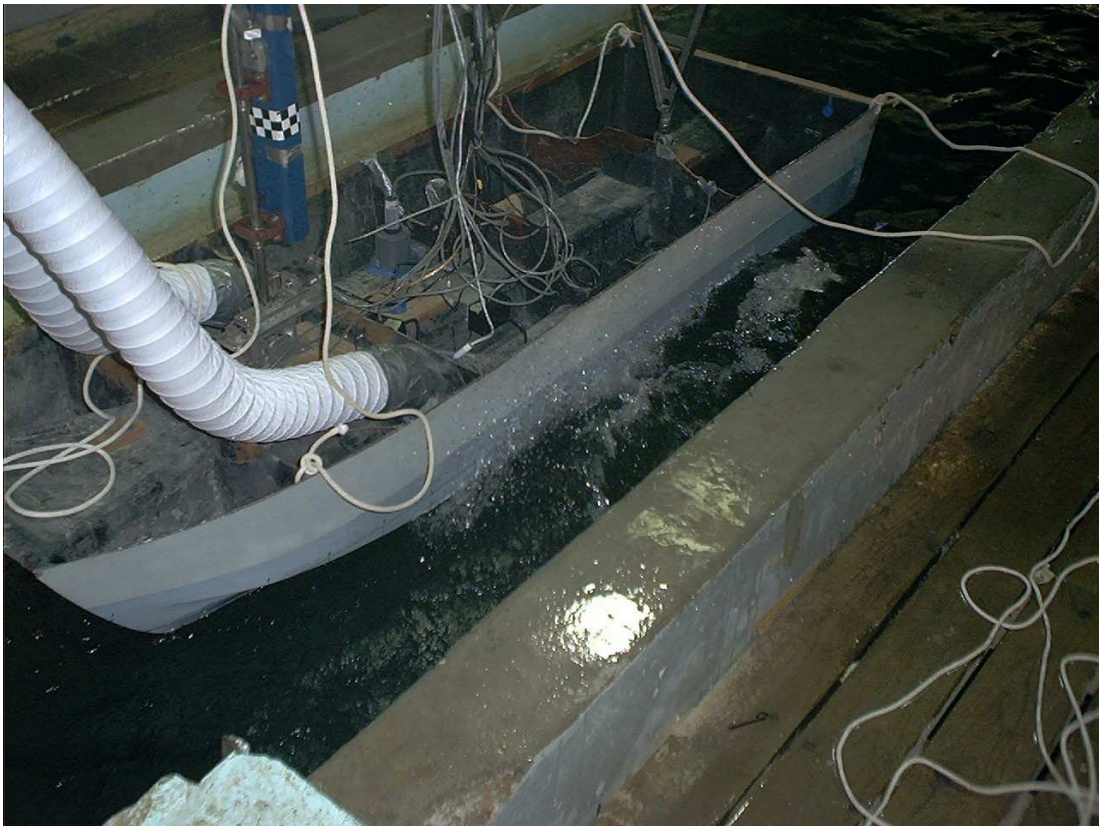

Figure 12. View of an RPM test, with air ducts attached from forward side.

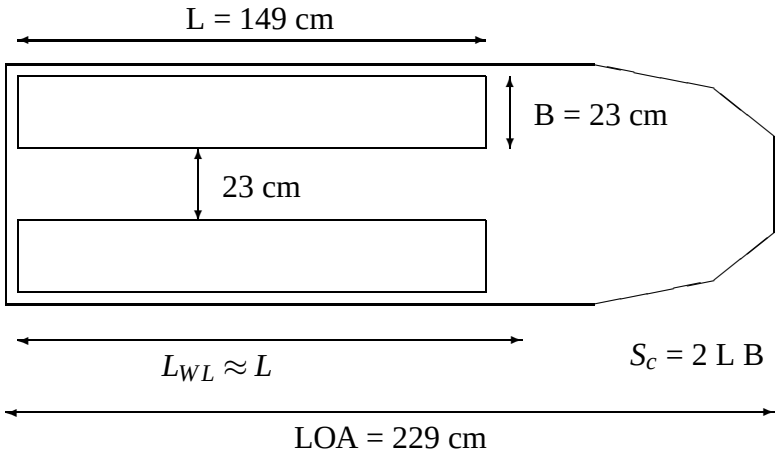

Figure 13. Schematic of air cushion dimensions on the 2.3 m HSC-SES model; the length of each air cushion is 149 cm with a beam of 23 cm; the separation between the two air cushions is approximately 23 cm. The waterline length, L_{WL}, is slightly greater than the length of the cushions. The cushion area is then 0.68 m^2.

diameter, and at an angle 30^o from horizontal. The height of the cushion above the keel was 18 cm. The leakage area between the sidehulls is approximately 23 cm across, and 2.5 and 3 cm higher than the keel at the stern and bow (Fig. 7,8). Since the cross-section the airflow leaks from is roughly triangular, the maximum possible leakage areas at the bow and stern are approximately 0.006 m^2 and 0.007 m^2, respectively. This results in a maximum possible leakage area of approximately 0.013 m^2 without air leaking underneath the keels of the sidehulls.

For the tests at IMD, the pressure sensors were installed by drilling small pressure ports in the air cushions and running small diameter tubing from these ports to the sensors, contained separately. The sensors then measured the difference in pressure between the air cushion at the specific pressure port and the outside air; because they were differential sensors, this data was tared using the average recorded pressures when the fans were off and the model was not moving. As seen in other studies by the David Taylor Naval Ship R&D Center [31], pressure sensors installed in such a manner (as opposed to flush-mount pressure transducers) can have static pressure errors on the order

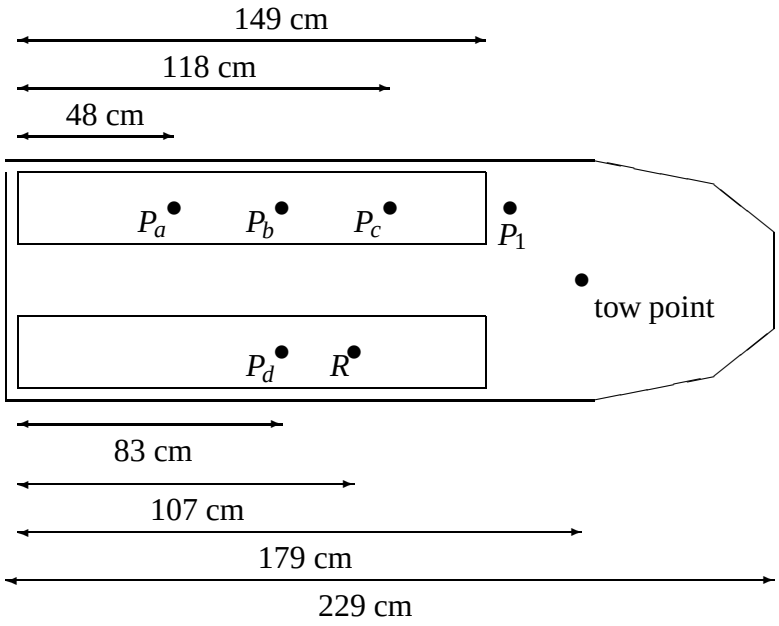

Figure 14. Top view of sensor locations on the HSC-SES model at IMD; static pressure sensors p_a, p_b, p_c, and p_d measured air pressures within the cushions, whereas p_1 measured the pressure in the port cushion air inlet. The range finder measured the air gap R in the starboard cushion 107 cm from the stern.

of 100 Pa due to water accumulating in the tubing. This type of error did not permit accurate measurements of average pressures within the cushions for much of the testing.

1.4 Results

Results are divided up into RPM, air drag, and resistance tests.

1.4.1 RPM tests

Seven different RPM tests were conducted for different displacements and lcgs. The results for a displacement of 29 kg, are presented herein. A significant vibration was present for much of the test, except for the lowest fan speed used (1200 rpm). The distinguishing feature of this low fan speed is that the total pressure applied to the air cushions was not sufficient to force air out from underneath the air cushions. From the video recordings of the tests, waves can be seen in the RPM tests moving aft, where air leaks out the sides of the cushions in gusts.

Figure 15. Camera views around the hull during testing at IMD (view towards stern, top left; outside view, top right; view from cushion inlet, bottom left; between demihulls, bottom right).

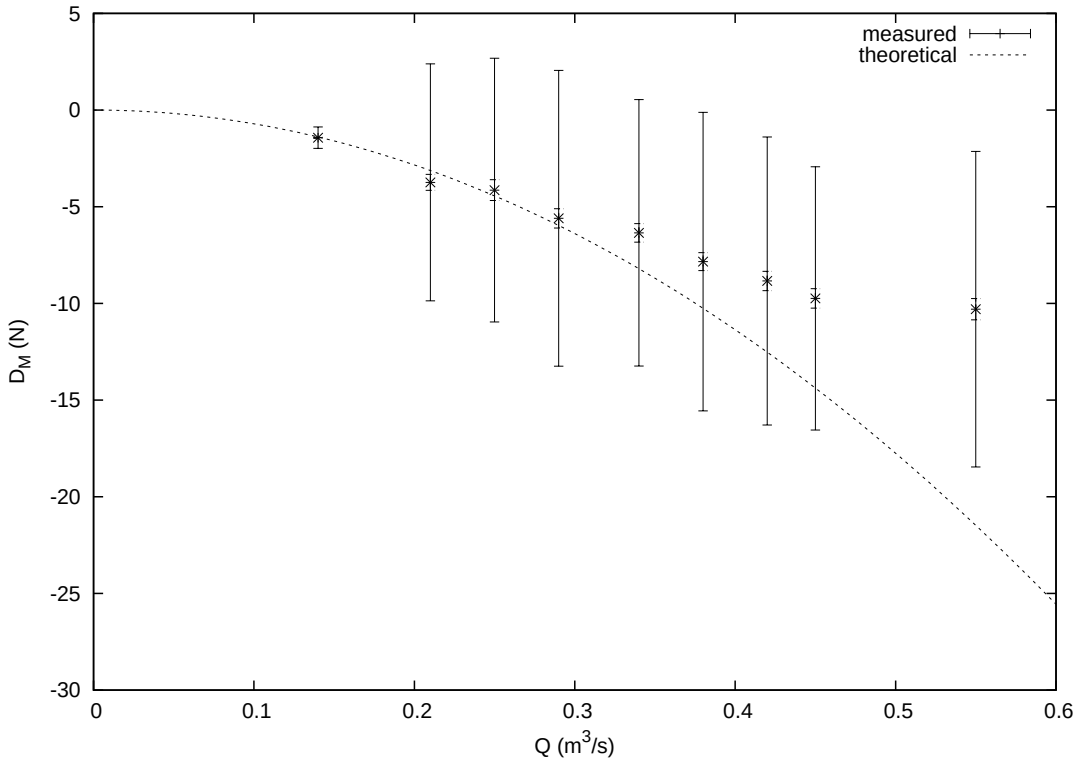

Figure 16. Comparison of measured momentum drag, mean, standard deviation, and 95% confidence interval for the mean, with theoretical. Note that the airflow in the tests was either 0.28, 0.36, or 0.53 m^3/s.

The momentum drag measured during a RPM test is caused by the airflow Q moving through air ducts of cross-section A_i changing speed to come to rest:

$$D_M = -\rho_a \frac{Q^2}{A_i}. \tag{16}$$

The measured results can be compared to this relationship (Fig. 16). Clearly, there is a substantial vibration as seen in the standard deviation of the measured momentum drag, and as mentioned earlier. For moderate airflows less than 0.3 m^3/s, the measured and theoretical results agree; for higher airflow, the deviation is likely due to excess airflow being forced forward out of the air cushions. Because it was observed that steady air leakage only happened from the bow, and not from the stern, this difference is probably not important for resistance tests.

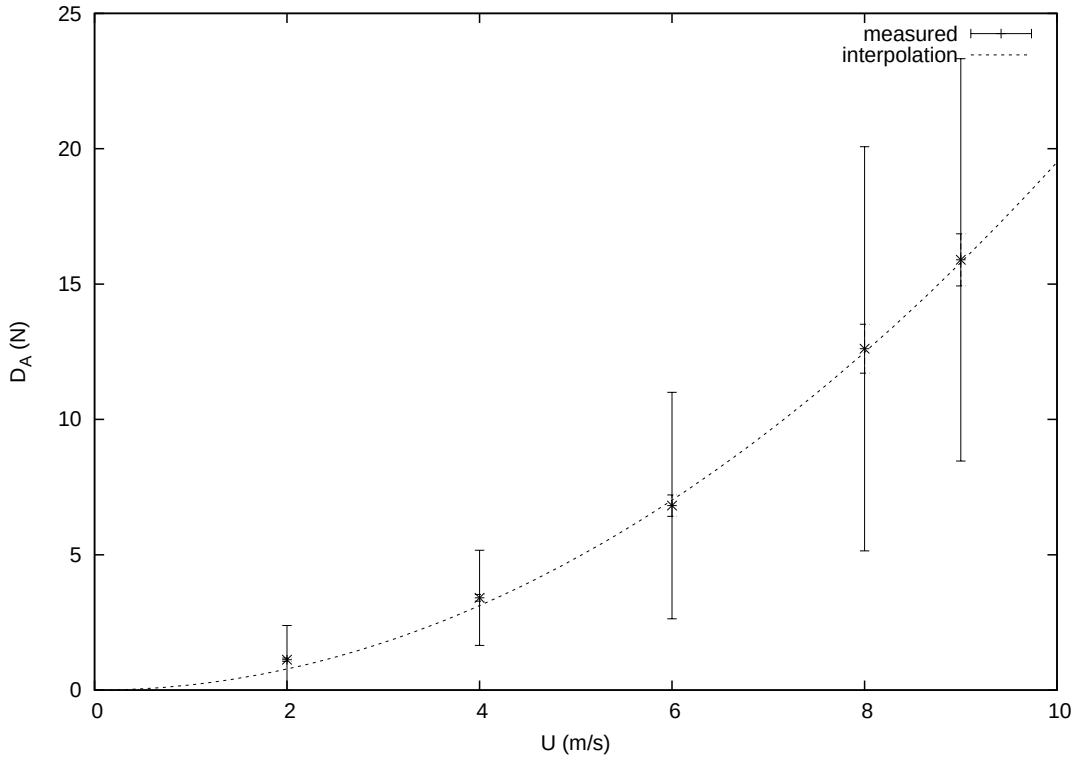

Figure 17. Tow force measured during air drag tests; mean, standard deviation, and 95% confidence interval for mean compared to curve-fit of 0.30 m^2 cross-sectional area. Because the mean of the measured air drag closely follows a quadratic fit with speed, the results seem credible.

1.4.2 Air drag tests

Air drag was measured by raising the model slightly out of the water and measuring the drag force when towed. The mean results vary with the square of the velocity, which is expected for a turbulent resistance measurement (Fig. 17). From (5), an effective cross-sectional area, $C_A S_A$ of 0.30 m^2 can be estimated for the model using a least-squares fit to the data.

The large standard deviation for the air drag measurements is most likely due to vibration of the tow carriage. The tow carriage is designed to measure forces over a range of $\pm$350 N range with a model hull in the water, so small vibrations would probably be damped, as compared to air drag measurements around 15 N. This vibration

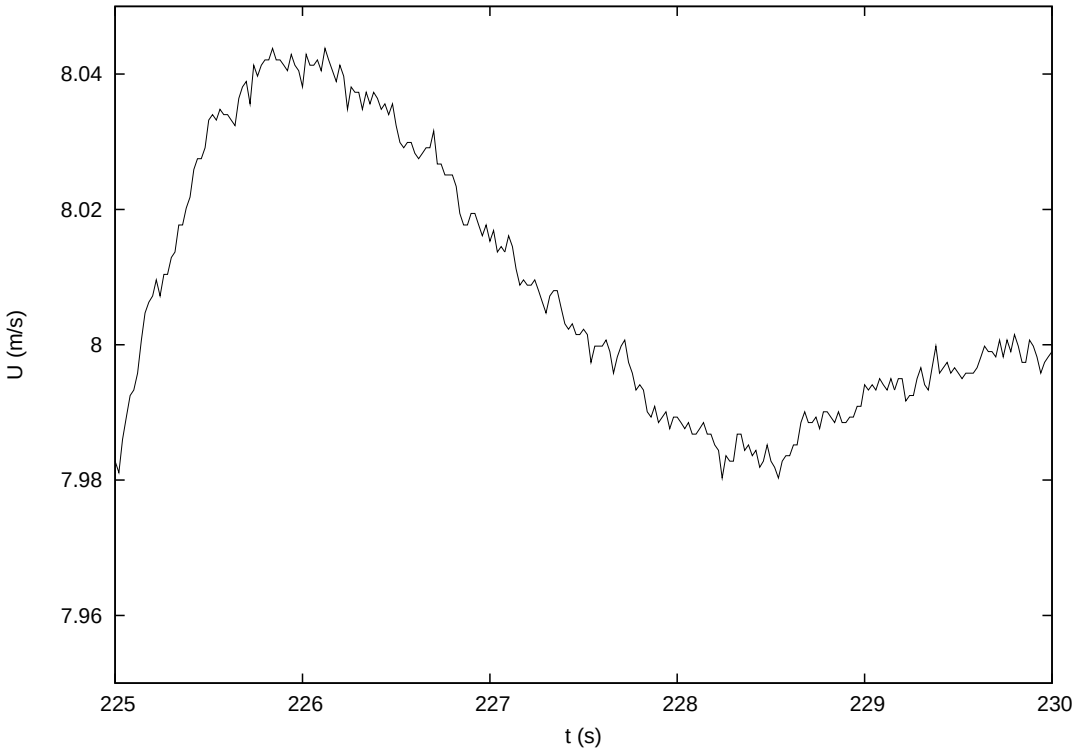

Figure 18. Tow carriage speed measured during an 8 m/s air drag measurement. Notice the high frequency vibrations.

can be seen in the measurement of the tow carriage speed (Fig. 18).

1.4.3 Resistance tests

Drag measured in resistance tests (Table 2) were corrected (Table 3) for momentum and air drag using (1), and cushion inlet pressures were measured (Table 4). Correction factors used momentum drag calculations, (16) (i.e., 5.57 N, 9.20 N, and 19.9 N for 2400, 3000, and 4140 RPM tests), and air drag estimates (Fig. 17). Notice that the corrected drag does not always decrease with increasing airflow; this could be due to a fault in how momentum drag is corrected, or it could simply be due to changes in WSA. Often, the air gap within the cushion detected by the range finder decreased with increasing airflow (Table 7).

The trim angle and draft of the model (Fig. 19) was recorded for each test (Ta-

Table 2. Averaged (and tared) drag measurements (N).

W (N)	RPM	2 (m/s)	4 (m/s)	6 (m/s)	8 (m/s)	9 (m/s)
	4140	13.45	32.09	43.70	47.33	50.97
445	3000	19.52	35.80	49.65	55.40	60.35
	2400	20.95	39.83	58.73	69.00	
	4140		20.39	30.32	39.57	
356	3000		24.69	37.56	45.60	
	2400		26.69	43.32	54.78	
	4140	1.41	13.67	23.42	33.99	52.16
289	3000		17.26	32.34	40.24	
	2400		19.64	36.43	47.27	

Table 3. Corrected mean drag measurements (N).

W (N)	RPM	2 (m/s)	4 (m/s)	6 (m/s)	8 (m/s)	9 (m/s)
	4140	32.28	48.64	56.83	54.67	55.03
445	3000	27.60	41.60	52.04	51.99	53.67
	2400	25.39	41.99	57.48	61.96	
	4140		36.94	43.46	46.91	
356	3000		30.49	39.95	42.19	
	2400		28.85	42.08	47.74	
	4140	20.24	30.21	36.56	41.33	56.22
289	3000		23.05	34.73	36.84	
	2400		21.80	35.19	40.22	

Table 4. Selected inlet pressure measurements (in Pascals).

W (N)	RPM	2 (m/s)	4 (m/s)	6 (m/s)	8 (m/s)	9 (m/s)
	4140	389.4	437.4	578.9	484.4	454.1
445	3000	452.1	482.8	605.4	560.9	534.3
	2400	468.5	508.4	614.3	606.4	
	4140		344.4	432.4	340.2	
356	3000		392.0	466.5	414.3	
	2400		400.9	461.0	446.6	
	4140	232.0	274.6	331.5	227.5	216.8
289	3000		316.5	367.8	305.3	
	2400		340.1	375.3	357.7	

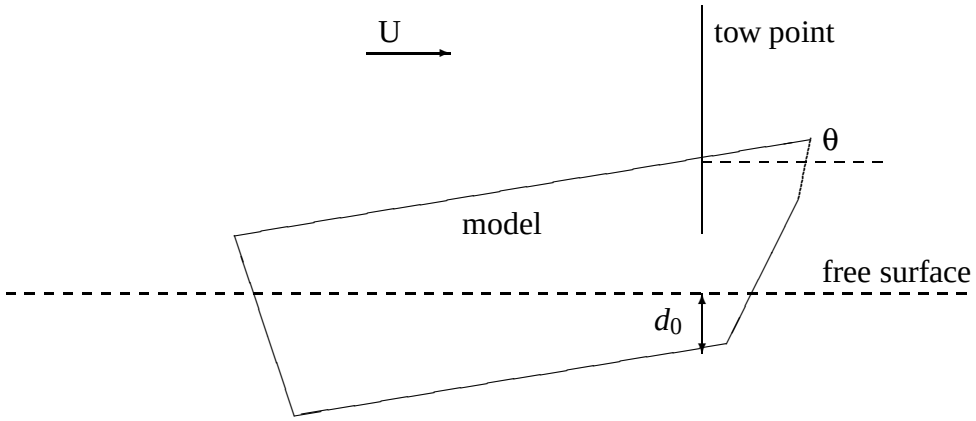

Figure 19. Definition of trim angle, θ, and draft at tow point, d_0.

bles 5,6). As well, the range finder data (Table 7), though sometimes erratic (e.g., Fig. 20), was corrected to measure the change in water surface height within the cushion below the range finder (Table 8).

At no point in the resistance tests were all pressures sensors within the cushions (i.e., p_a, p_b, p_c, p_d) functioning properly. This can be seen most readily with a triplicate of test runs at 45 kg, 9 m/s, and 4140 RPM (Table 9). For each test run, a reference pressure was recorded some time before the test, and then an average pressure during the test was recorded. Because the pressure sensors used were differential, the reference

Table 5. Selected trim measurements (in degrees).

W (N)	RPM	2 (m/s)	4 (m/s)	6 (m/s)	8 (m/s)	9 (m/s)
	4140	0.85	1.62	1.63	1.22	1.25
445	3000	1.02	1.66	1.38	1.04	1.20
	2400	1.03	1.78	1.47	1.10	
	4140		0.80	0.82	0.98	
356	3000		0.95	0.77	0.93	
	2400		0.96	0.79	0.75	
	4140	-0.30	0.10	0.17	0.71	1.07
289	3000		0.18	0.14	0.63	
	2400		0.29	0.28	0.49	

Table 6. Selected draft (at tow point) measurements (in mm).

W (N)	RPM	2 (m/s)	4 (m/s)	6 (m/s)	8 (m/s)	9 (m/s)
	4140	49.86	23.06	11.00	15.60	11.21
445	3000	50.30	23.13	18.72	18.26	12.10
	2400	49.88	23.85	20.20	24.19	
	4140		22.31	18.26	12.71	
356	3000		23.68	19.08	14.30	
	2400		24.26	19.68	20.74	
	4140	43.39	26.99	18.15	11.12	4.38
289	3000		25.59	22.91	14.67	
	2400		26.10	22.21	19.53	

Table 7. Difference in air cushion gap (mm) underneath range finder between trial runs and at rest. Faulty measurements are marked as N/A.

W (N)	RPM	2 (m/s)	4 (m/s)	6 (m/s)	8 (m/s)	9 (m/s)
	4140	73.8	66.0	58.3	52.8	53.6
445	3000	82.7	68.1	68.3	63.0	55.3
	2400	83.3	68.6	60.2	N/A	
	4140		54.0	50.9	43.2	
356	3000		58.2	56.8	47.2	
	2400		60.1	58.4	50.0	
	4140	N/A	N/A	N/A	N/A	N/A
289	3000		N/A	N/A	N/A	
	2400		N/A	N/A	N/A	

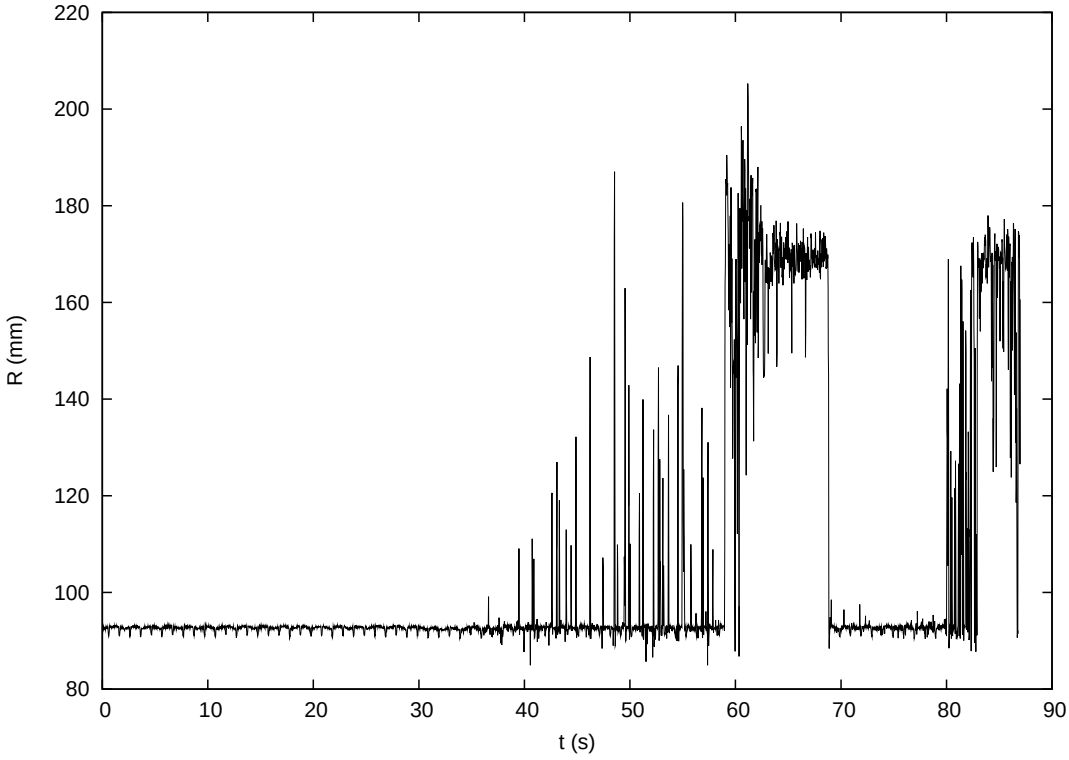

Figure 20. Faulty range finder measurement during 29 kg, 6 m/s, 3000 RPM test, possibly due to water spray within the air cushion. Note that air cushion height over keel is 18 cm.

Table 8. Changes in free-surface elevation within the air cushion underneath the range finder (mm). Faulty measurements are marked as N/A.

W (N)	RPM	2 (m/s)	4 (m/s)	6 (m/s)	8 (m/s)	9 (m/s)
	4140	-48.1	-23.5	- 4.9	0.5	5.0
445	3000	-59.5	-24.1	-18.3	-8.8	3.1
	2400	-59.9	-27.1	-15.5	N/A	
	4140		-11.9	-4.7	4.6	
356	3000		-18.2	-10.5	-0.2	
	2400		-21.7	-13.9	-5.7	
	4140	N/A	N/A	N/A	6.3	N/A
289	3000		N/A	N/A	N/A	
	2400		N/A	N/A	N/A	

Table 9. Mean pressures (in Pa) tared records (and reference value) for resistance tests at 45 kg, 9 m/s, and 4140 RPM. The difference between the values is the measured pressure. Notice the inconsistencies between the tests, and even the reference values.

p_a	p_b	p_c	p_d
2.534 (-1935.)	48.28 (-2314.)	1204. (-2125.)	796.2 (-2459.)
-4.988 (-1934.)	1175. (-2407.)	1369.3 (-2476.)	1231.5 (-2464.)
93.98 (-1913.)	1042. (-2396.)	865.5 (-1967.)	824.6 (-2115.)

reading was not zero, and the difference (or tared value) between the pressure measured during the test and the reference value was the actual air pressure in the cushion.

Similar to the RPM tests and air drag tests, the standard deviation of the recorded tow force during resistance tests was significant for all tests. This could be due to a number of things (e.g., instabilities of high airflow flowing through the cushions, oscillations within the air ducts, porpoising). This noise does not happen at larger scales, apparently, since the oscillations have never been observed on prototypes while moving. One early test (with an unrecorded weight), at 1.5 m/s and 1800 RPM (0.23 m^3/s) was run at speed both with and without the air blower turned on, and the results demon-

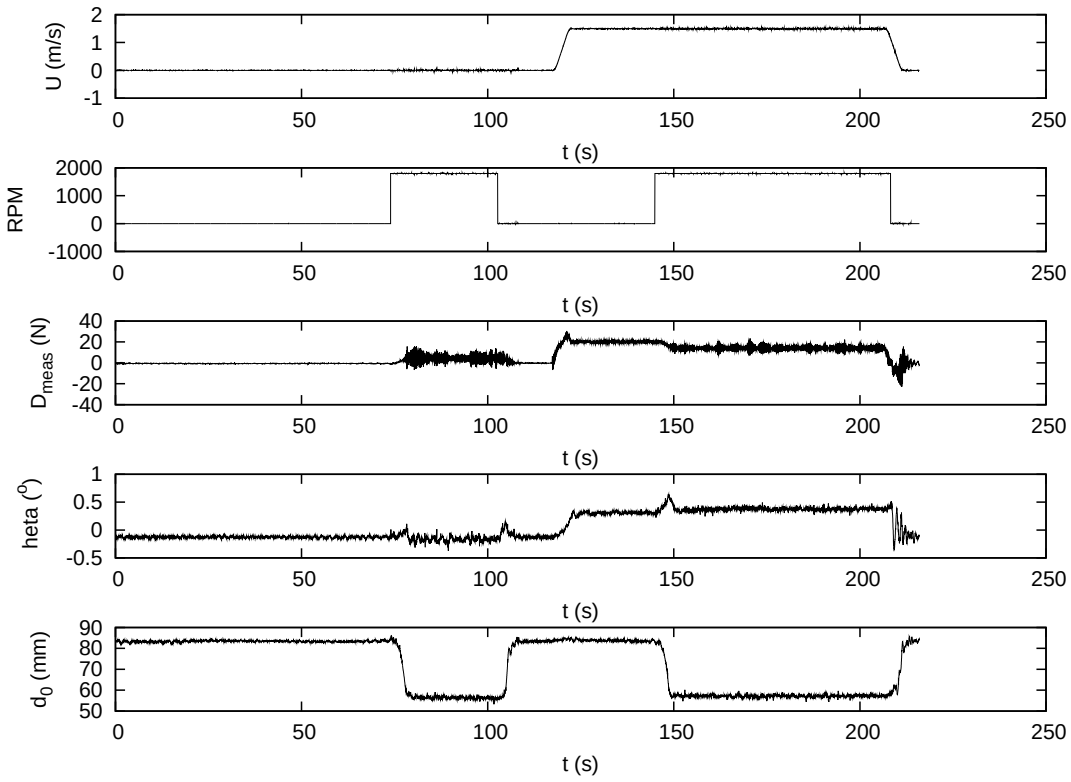

Figure 21. Tow carriage speed (U, m/s), fan speed (RPM), tow force (D_{meas}, N), trim (θ, ^{o}), and draft (d_0, mm) for 1.5 m/s, 1800 RPM (0.23 m^3/s) test. Notice the lack of vibrations when the air blower is off, even when the model is moving.

strate that the vibration present in the tow force measurement is directly related to the air blower (Fig. 21). Because the vibration is only present when the air blower is on, it is possible that the air blower itself is causing the tow carriage to shake, but it is not possible to form a conclusion with the available data. No tests were run with the blower on and the HSC-SES model out of the water (e.g., to see if the noise is caused by an airflow instability), and the sampling frequency of the available data (50 Hz) is not high enough to separate possible sources (e.g., fan rotation rate, acoustic resonance).

1.5 Discussion

A few observations can be made about the results. The effects of the finite depth of the towing tank are first considered, which is sometimes an important consideration

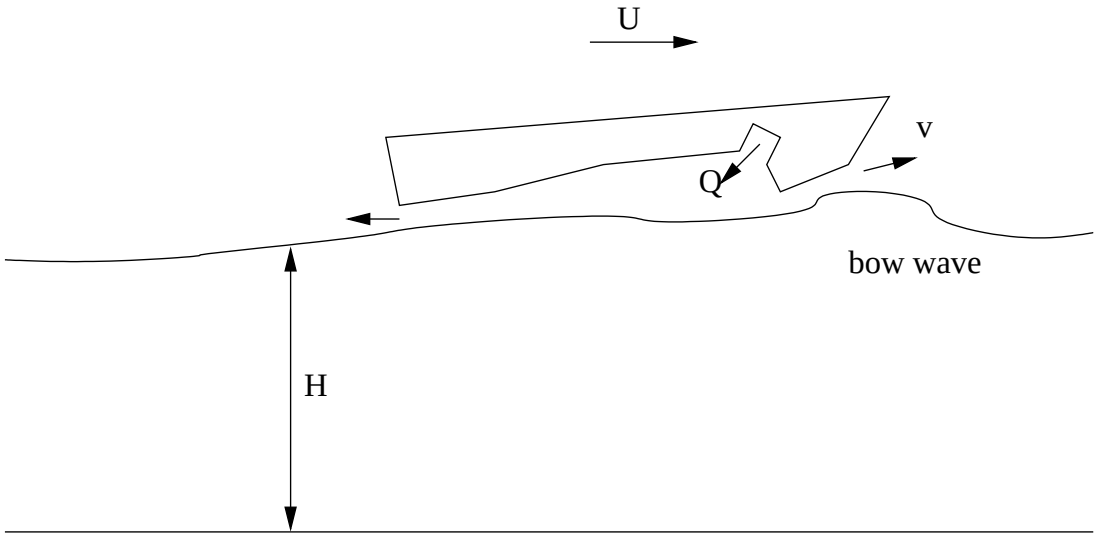

Figure 22. Hypothesized bow wave caused by supercritical flow conditions.

in high speed tests. Then the wavemaking drag is estimated and the power requirements for a prototype vessel are extrapolated from the available data.

1.5.1 Shallow water effects

The critical speed for the towing tank at IMD was 8.3 m/s. This can have a number of effects (e.g., changes in surface wave pattern, ship trip) for results at speeds near the critical speed. While it is not possible to tell from the limited dataset whether there is an effect on the overall resistance, a few effects are noticable that do seem related to the critical speed.

For several of the resistance tests, the wake measured within the air cushions is raised with respect to the undisturbed free-surface (Table 8). At high Froude number, though, the slope of the wake within the air cushion is nearly constant, and this slope corresponds to wavemaking drag. A raised wake would suggest either a negative wavemaking drag, which never happens at steady-state, or that the water surface is raised at the leading edge of the air cushion (Fig. 22).

Because the raised surface only happens at high speed or high airflow, it is likely

related to a high differential speed between the air and water. Supercritical conditions could be the cause. It is not possible with the limited information available, though, to determine the airflow conditions required to create this bow wave. Notice also that when this bow wave is formed, the normal trends of the HSC-SES behavior, such as decreasing trim angle with increasing airflow, are reversed (Table 5).

Consider, for instance, the 8 m/s, 36 kg (356 N) displacement data (Tables 6,8). While the wake varies from -5.7 mm to +4.6 mm (a difference of 10.3 mm), the draft at the bow decreases from 20.7 mm to 12.7 mm (a difference of 8.0 mm); essentially, the free-surface slope within the air cushions changes little, but the free-surface elevation rises.

1.5.2 Wavemaking drag

By using the measured free-surface, it is possible to estimate the wavemaking drag of the resistance tests at high Froude number, by assuming a constant slope within the air cushions:

$$D_W = -W\frac{\Delta R}{x_{rf}} \tag{17}$$

where ΔR is the wake measured from the range finder, and x_{rf} is the distance between the start of the cushion and the range finder, or 42 cm (Fig. 23). Because of issues with high airflow, only the lowest airflow and highest displacement tests are used to determine the wavemaking drag (Table 10). Unfortunately, the 2 m/s data is for a low Froude number (0.52), and the 9 m/s data did not provide an accurate reading of the wake within the air cushion.

Assuming all residual drag is due to wavemaking, the WSA is then simple to compute from (1) (Table 1.5.2):

$$S_W = \frac{D_{meas} - D_M - D_A - D_W}{\frac{1}{2}\rho C_f U^2}. \tag{18}$$

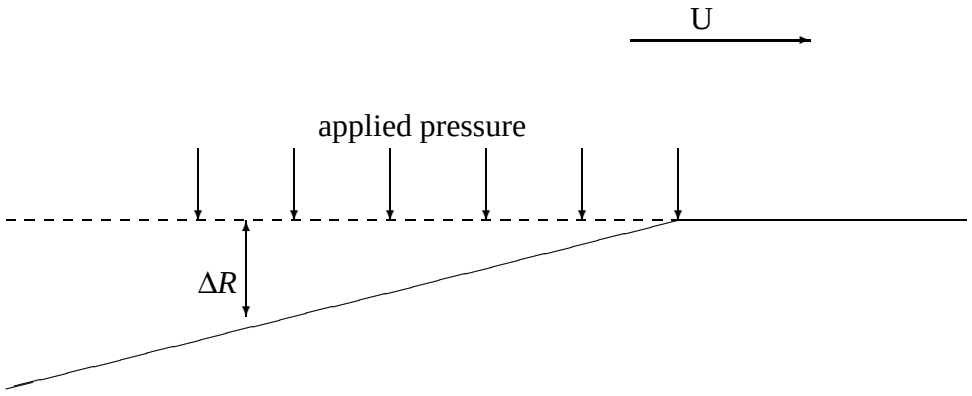

Figure 23. Schematic of free-surface caused by HSC-SES at a high speed, U; ΔR is the change in free-surface elevation.

Table 10. Estimated wavemaking drag (N) for 445 N displacement tests. Clearly additional data would be useful.

U (m/s)	4	6	8
D_W (N)	28.7	16.4	9.3

In order to also handle other displacements (i.e., the 36 and 29 kg tests), an additional assumption is required. If linear free-surface boundary conditions are also assumed, then changes in free-surface slope and free-surface pressure will scale with displacement (i.e., wavemaking drag scales with the square of displacement).

Notice that these estimates give WSA similar to the cushion area ($S_c = 0.68$ m^2). Therefore the minimization of WSA provided by an SES hull is mostly negated by being a catamaran.

1.5.3 Prototype extrapolation

The *Gladius* was a proposed 25 m prototype, which was supposed to be a total of 60 MT, travel at 31 m/s (60 kts), and was powered by 2984 kW (4000 hp) of propulsion power and 746 kW (1000 hp) of lift power. Because of the slight change in WSA with increasing cushion airflow (Table 1.5.2), the lowest airflow conditions measured are the most efficient.

Table 11. WSA (m^2) estimates for selected tests.

W (N)	RPM	4 (m/s)	6 (m/s)	8 (m/s)
	4140	0.65	0.64	0.42
445	3000	0.42	0.56	0.40
	2400	0.43	0.63	0.49
	4140	0.61	0.52	0.38
356	3000	0.40	0.46	0.34
	2400	0.34	0.50	0.39
	4140	0.59	0.47	0.35
289	3000	0.36	0.44	0.31
	2400	0.32	0.44	0.34

Table 12. Estimated power requirements of the *Gladius*.

U (m/s)	D_R (kN)	D_F (kN)	D_A (kN)	D_M (kN)	P_P (kW)	P_L (kW)
13.	37.5	9.44	1.28	3.13	954.	1142.
20.	21.4	30.7	2.88	4.82	1709.	1325.
26.	12.2	38.9	5.12	6.26	2321.	1311.

Combining the components of drag, and assuming an efficiency of 70%, a resistance extrapolation can be computed (Table 12). An air drag coefficient of 0.3 is assumed due to the fine lines of the superstructure.

While this drag extrapolation is based on a number of conjectures that cannot be proven without more study, it certainly seems plausible that the performance of the prototype would have met expectations had it been built. Clearly, the fan power needs to be decreased, and there will be a corresponding increase in propulsion power. Note that for the 26 m/s case, the transport efficiency is 4.2.

1.6 Summary

Ships are supported through some combination of hydrostatic, hydrodynamic, aerodynamic, or aerostatic lift. The most efficient of these for high Froude numbers is the

aerostatic lift. In order to limit wavemaking drag of an air cushion vehicle, a high length-to-breadth vessel is required. Since the center of gravity is high on a SES because much of the mass is above the air cushion, this limits the stability of the hull. In order to retain lateral stability, a twin-cushion design is required.

Typical SESs have had flexible seals fore and aft, but this can become inherently complicated, especially for a twin-cushion design. Despite claims that this is a new technology, in the first years of SES development, similar craft were built. While seal-less designs were abandoned for a low L/B vessel, a high L/B vessel has a smaller leakage area, so the lack of flexible seals is less of a concern.

This line of reasoning has resulted in the HSC-SES. Using the best scale model resistance tests available, it appears that wavemaking drag is dependent mainly on weight and speed, not airflow, and that the WSA is a function of only the wavemaking drag and trim; the trim, in turn, is a function of airflow.

By adjusting the hullform, or adding control surfaces to the bottom of the hull, WSA and leakage area could both be decreased further, but existing tests suggest that the design is feasible. Higher design speeds for the HSC-SES are limited by the large WSA expected for such a seal-less twin-cushion design. The low draft advantage of an SES over other hullforms, however, remains true.

The most credible quantitative results of the HSC-SES were conducted at IMD in 2002 with a 2.3 m model. These results were evaluated in this manuscript. Near the critical speed of the tank, it seems likely a bow wave is produced. More importantly, resistance estimates are made at a variety of speeds and displacements. Because the wetted surface area of the model was not measured, extrapolating the resistance measurements to full-scale required a crude estimate of wavemaking drag. In this manuscript, this estimate was made using range finder measurements of the free-surface within the air cushions. An alternative estimate of wavemaking drag could be made using a numeri-

cal model. The utility of these results is questionable because the airflow used during the model-scale tests was unrealistically high, but the overall power requirements of a HSC-SES should be good enough for an order-of-magnitude estimate.

Future model testing should use less airflow and have a higher sampling frequency; the air blowers were overpowered in the IMD tests, resulting in data that may not actually correspond to ideal test conditions, and the resonance frequencies of the air cushions were much higher than the sampling frequency. Also, the results are strongly dependent on how the model-scale momentum drag is computed.

Because the skin friction drag depends on the trim angle and no towing tank data exists to conjecture the behavior of the HSC-SES in waves, it isn't clear how well the design would fare on the open ocean. Historically, though, similar designs have been considered for transoceanic service, and the HSC-SES could be suitable if built at large scales. To develop the design further, additional tests at both model- and full-scales must be conducted.

List of References

[1] C. B. McKesson, "Hull form and propulsor technology for high speed sealift," in *High-Speed Sealift Technology Workshop*. Center for the Commercial Deployment of Transportation Technology, 1998.

[2] E. Butler, "The surface effect ship," *Naval Engineers Journal*, vol. 97, pp. 200–260, 1985.

[3] P. Mantle, "Development of the USN surface effect ship, SES-100B," *Naval Engineers Journal*, vol. 85, no. 5, pp. 65–77, October 1973.

[4] P. Mantle, *Air cushion craft development*. David Taylor Naval Ship Research and Development Center, 1980, no. 80/012.

[5] N. Madavan, S. Deutsch, and C. Merkle, "Reduction of turbulent skin friction by microbubbles," *Physics of Fluids*, vol. 27, no. 2, pp. 356–363, February 1984.

[6] H. Legner, "A simple model for gas bubble drag reduction," *Physics of Fluids*, vol. 27, no. 12, pp. 2788–2790, December 1984.

[7] L. Yun and A. Bliault, *Theory and design of air cushion craft*. John Wiley and Sons, 1999.

[8] J. Chung, "Skirt-material damping effects on heave dynamics of an air-cushion-vehicle bag-and-finger skirt," *Canadian Aeronautics and Space Journal*, vol. 48, no. 3, pp. 201–212, 2002.

[9] D. Bertin, S. Bittanti, and S. Savaresi, "Decoupled cushion control in ride control systems for air cushion catamarans," *Control Engineering Practice*, vol. 8, pp. 191–203, 2000.

[10] A. Skolnick, "Transoceanic surface effect ships," in *Proceedings of the Institute of Electrical and Electronics Engineers*, vol. 56, no. 4, 1968, pp. 700–712.

[11] "The surface effect ship: advanced design and technology," Prepared for the Surface Effect Ship Program Office, PM-17, 1974.

[12] K. Knüpffer and J.C. Frambourg and J.C. Lewthwaite and J.D. Adams, *The Federal Republic of Germany's fast test craft*. American Institute of Aeronautics and Astronautics, 1989, no. 89-1471-CP.

[13] J. Wessel, "Review on German SES developments and the government funded R+D programme SUS C," in *Proceedings of the International Conference on Fast Sea Transportation (FAST 1995)*, vol. 12, 1995, pp. 917–930.

[14] M. Bebar and D. Liberatore, *U.S. Navy high performance ship concept formulation*. American Institute of Aeronautics and Astronautics, 1983, no. 626.

[15] F. Wilson, P. Viars, and J. Adams, *Feasibility design for a surface effect catamaran corvette escort*. American Institute of Aeronautics and Astronautics, 1983, no. 619.

[16] F. Wilson and P. Viars, *The surface effect catamaran - a sea capable small ship*. American Institute of Aeronautics and Astronautics, 1981, no. 2076.

[17] F. Wilson, P. Viars, and J. Adams, "Surface effect catamaran – progress in concept assessment," *Naval Engineering Journal*, vol. 95, no. 3, pp. 301–311, May 1983.

[18] J. Durkin and N. Paraskevas, *Progress in the development of the surface effect catamaran (SECAT)*. American Institute for Aeronautics and Astronautics, 1986, no. 2364.

[19] L. Doctors and S. Sharma, "The wave resistance of an air-cushion vehicle in steady and accelerated motion," *Journal of Ship Research*, vol. 16, pp. 248–260, 1972.

[20] H. Harley, "Surface effect vessel hull," U.S. Patent 5 570 650, 1996.

[21] R. Latorre, A. Miller, and R. Philips, "Micro-bubble resistance reduction for high speed craft," *Society of Naval Architects and Marine Engineers Transactions*, vol. 110, pp. 259–277, 2002.

[22] B. Allenström and H. Liljenberg and U. Tudem, "An airlifted catamaran – hydrodynamical aspects," in *International Conference of Fast Sea Transportation (FAST 2001)*. Southampton, UK: Royal Institution of Naval Architects, Sept 2001.

[23] U. Tudem, A. Eilertsen, J. G. Eide, H. Liljenberg, and M. Lindholm, "Design development of 24 m air supported vessel (ASV) catamaran demonstrator, suitable for fast passenger ferries and various naval / paramilitary applications," in *High Speed Craft: Design & Operation*. London, UK: Royal Institution of Naval Architects, 2004.

[24] A. Bengston, *Laboratory experiments to determine the dynamic response of a ship-to-shore causeway system*. Master's thesis, University of Rhode Island, 2001.

[25] M. Shultz, *Simulation of a ship-to-shore causeway system in waves*. Master's thesis, University of Rhode Island, 2005.

[26] "Testing and extrapolation methods high speed marine vehicles resistance test," International Towing Tank Conference Recommended Procedures 7.5-02-05-01, 2002.

[27] E. Tuck, D. Scullen, and L. Lazauskas, "Wave patterns and minimum wave resistance for high-speed vessels," in *Proceedings of the 24th Symposium on Naval Hydrodynamics*, Kukuoka, Japan, 2002.

[28] J. Moulijn, *Scaling of air cushion dynamics*. Delft University of Technology, July 1998, no. Report 1151, Project Code 961.

[29] R. von Mises, *Theory of Flight*. Dover Publishing, 1959.

[30] O. Ritter and M. Templeman, *High-speed sealift technology Volume 1*. Carderock Division Naval Surface Warfare Center, September 1998, no. CDNSWC-TSSD-98-009, technology Projection Report.

[31] C. Bradley, *Surface effect ship air cavity pressure gauges*. David Taylor Naval Ship R&D Center, July 1981, no. DTNSRDC/CID-81/1.

MANUSCRIPT 2

On the wavemaking drag of a twin-cushion surface effect ship

2.1 Introduction

In recent years there has been broad interest in high speed ships, not only for special purpose military craft, but also for passenger ferries and commercial sealift [1]. One of the most promising hullforms for high speeds is the Surface Effect Ship (SES). SES designs are often limited by wavemaking drag caused by the air cushion, which acts as a moving pressure patch on the free-surface of the water. This manuscript presents selected results of a fully-nonlinear potential flow wave model that was applied to a twin cushion SES in order to estimate its wavemaking drag.

SES designs have been in existance since 1960, when the concept was proposed by Allen Ford [2]. They are essentially specialized and more efficient versions of hovercrafts used for traveling over water. SES designs are among the most efficient at high Froude numbers. With a very shallow draft, the SES wavemaking drag is low, yet unlike dynamically supported crafts such as hydrofoils, an SES also has a small wetted surface area (WSA) and therefore a low friction drag. The disadvantage is that a SES does require extra power, weight, and machinery, to operate the lift fans generating the airflow in the cushions.

A typical SES consists of a single rectangular cushion (called a pressure patch) contained by two slender sidehulls and fore and aft flexible seals [3]. This air cushion is a region of nearly uniform air pressure, which is actively created and maintained by a number of lift fans providing sufficient air flow. In operation, air continuously leaks out underneath the fore and aft seals. While the sidehulls (that a hovercraft lacks) slightly add to the ship's hydrodynamic resistance, they decrease air leakage and typically provide for an increase in overall energy efficiency.

In the 1980s, U.S. Navy SES research focused on studying the surface effect cata-

maran (SECAT) concept [4] under the Surface Ship Continuing Concept Formulation (CONFORM) Program [5]. The SECAT design was essentially two air cushions placed side-by-side (a catamaran), connected by a bridging structure. The project included both theoretical studies into the wavemaking resistance [6, 7], as well as measurements on a 10 m prototype that was constructed [8]. The advantage of the SECAT over other designs at the time was that two high length-to-beam (L/B) air cushions have much lower wave resistance than a single low L/B air cushion, while maintaining the roll stability and high structural height.

2.1.1 Harley SES: a case study

The Harley SES was proposed by Howard Harley of Harley Shipbuilding Corporation (HSC) of Bartow, Florida, and was patented in 1996. The HSC-SES, as it is referred to in this paper, is a catamaran with rigid hulls having two air cavities (i.e., cushions), each pressurized from air inlets at the bow. Each demihull of the ship consists of a deep-V bow, with a step separating it from the air cushion, a lift fan at the bow which forces pressurized air into the cushion, two thin sidehulls or fins, which contain the air cushion, and an inverted-V transom stern (Fig. 24) [9].

Although HSC built several large scale models, including 7.9 m and 16.8 m prototypes, and a fast ferry, further development and refinement of the Harley design has mainly been conducted by Ocean Dynamics Inc., a former collaboration of HSC and Vibtech Inc., of Wickford, Rhode Island. As a result, since the initial patent, several changes have been made to the relative dimensions of the hull, particularly in regards to the cushions. It is thus currently thought that the optimal spacing between the demihulls is equal to their width, with both air cushions having a length-beam (L/B) ratio of 6.5, and extending from the stern to a point 65% of the way to the bow (i.e., 65% of the length overall).

A number of tow tank tests were performed on the HSC-SES design. Among these,

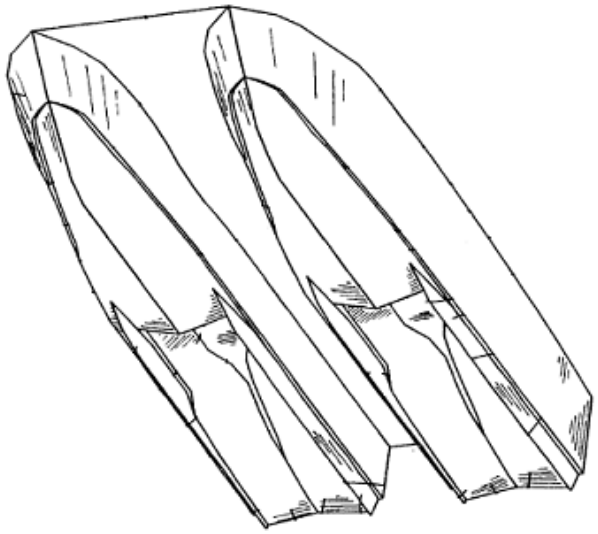

Figure 24. Harley SES concept hullform, patented 1996.

the more comprehensive and accurate results were obtained at the Institute for Marine Dynamics (IMD; now Institute for Ocean Technology), using a 2.2 m long SES model, in a 7.0 m deep, 12 m wide and 200 m long tank (see mansucript one). The model's air cushions are 1.49 m long (i.e. 67% of the model length), 0.23 m wide, and separated by 0.23 m. Reliable data was obtained from tests run at 4, 6, and 8 m/s, with a 445.4 N (100 lbs) model displacement. Using a high frequency acoustic range finder, located 1.07 m from the stern, it was possible to calculate an approximate free-surface angle within the air cushions. This required assuming that the free-surface was not significantly disturbed at the leading edge of the air cushions and that the free-surface within the cushions was flat. In this way, wavemaking drags of 28.7, 16.4, and 9.3 N were measured for the 4, 6, and 8 m/s cases, respectively (see mansucript one). Because wetted surface area (hence, frictional drag) was not directly measured in the IMD tests, confirmation of these wavemaking drag estimates would be helpful, for supporting the total resistance extrapolations we made for the HSC-SES to prototype scale (see manuscript one).

2.1.2 Background

Wave generation by a moving disturbance (pressure or solid hull), is well understood and acurately modeled in terms of inviscid fluid theory. Besides, in the time domain, when starting simulations from a state of rest, as we will do here, Kelvin's theorem ensures that the generated flow is and remains irrotational. Therefore, Fully Nonlinear Potential Flow (FNPF) theory is nearly exact for modeling the ship-wave problem and has historically been the set of governing equations used in most studies, both analytical and numerical. In a number of cases of practical interest, however, FNPF equations can be linearized, which has led to a large body of classical litterature on analytical and numerical results of ship wave resistance. There are even many applications where linear wave theory provides reasonably accurate results up to the point of wave breaking, where FNPF models also break down, unless some damping is included. Still, there are also many cases of practical importance, for which linear wave theory is significantly inaccurate, for instance in shallow water, at very low speeds, or for high displacement ships.

Within the inviscid fluid flow realm, many numerical methods of computing ship wave resistance have been proposed, for over a century. Michell's [10] thin-ship theory dates back to the late 19th century, and the representation of a ship's wake as a sum of Havelock sources (related to the pressure distribution on the free-surface) from the early 20th century [11]. The best known work on wave resistance for a moving pressure patch is the computations by Doctors and Sharma [12], who studied both the steady and unsteady wavemaking resistance of moving pressure patches, using a linearized theory. Linear wave theory, especially steady-state linear wave theory, has the significant advantage of being computationally very fast. For instance, using a piecewise polynomial approximation of a Havelock source by Newman [13] (closely related to the velocity potential of a moving punctual pressure on the free-surface), Tuck et al. [14] devel-

oped a model, which evaluates wave resistance of a ship in mere milliseconds and the free-surface elevation in minutes, using a standard PC.

More recently, many ship-wave simulation works have solved FNPF equations, and their various linearized versions, using a Boundary Element Method (BEM), based on free space or more specialized Green's functions, (see, notably Hess and Smith [15] and Dawson [16], and more recently, e.g., by Huang and Sclavounos, 1993 [17]). The principle advantages of a BEM is that the discretization – and approximation it leads to – is limited to the boundary and makes no additional assumptions about the solution within the domain. Hence, for a given accuracy, the number of discretization nodes, and hence discretization effort, is much smaller than with other methods (e.g., finite-difference and finite-element). The BEM solution can be further accelerated when using a fast multipole algorithm (FMA) that aproximates the Green's function for regions far of a given collocation node. Originally described by Greengard and Rokhlin [18], the FMA can compute the interactions between a large number N of particles in $O(N)$ time, a problem which traditionally takes at best $O(N^2)$ time with other methods. BEMs have been shown to be very accurate for highly nonlinear ship-wave problems [19]. Over time, the increasing computational power available, combined with FMAs, have allowed BEM techniques to be applied on a larger scale. In 1989, Jensen and others were using around 1000 collocation nodes for a steady state model [20], whereas in 1997, Scorpio used around 5000 collocation nodes [21]. Even more nodes were recently used in the FMA-accelerated model of Fochesato and Dias (2006).

Most BEM models applied to nonlinear wave (FNPF) modeling use a mixed Eulerian-Lagrangian (MEL) time-stepping algorithm, combined with an implicit predictor-corrector scheme, that was first introduced by Longuet-Higgins and Cokelet [22]. Results of such models, however, typically show a variety of numerical instabilities (e.g., Sen et al. [23]), that are usually eliminated by applying a smoothing

filter over the free-surfaces (Longuet-Higgins and Cokelet used a higher-order polynomial smoothing [22], or Xue et al. who used a second-order 13-point Savitzky-Golay filter [24]). The type and order of the elements used in a BEM model often have an effect on its stability. Janson [25], for instance, showed that higher-order elements are more stable than lower-order approximations when tested in their own formulation, and other authors reached similar conclusions [26]. Another approach that was shown to eliminate the occurrence of sawtooth instabilities is the use of higher-order explicit Taylor series expansions in the MEL time stepping, together with a higher-order representation of the free surface geometry and unknowns, that has a sufficiently high degree of inter-element continuity (typically second-order). Thus, following Dold and Peregrine (1984), Grilli et al. [27, 28, 26] developed a very accurate and stable two-dimensional explicit higher-order BEM model, that was applied to many different problems of wave generation by solid moving boundaries, propagation, transformation over complex bottom topography and to wave overturning ([29, 30, 31, 32, 33, 34]). This model, which did not require smoothing and results did not show any kind of instability, even after thousands of time steps, was extended to three-dimensions with similar success by Grilli et al. [35], who used bi-cubic overlapping elements for the discretization. Recently Fochesato and Dias (2006) implemented a FMA in this model and showed accelerations of the solution of up to one-order of magnitude [36]. Some authors have started using even more complicated and accurate BEM elements such as NURBS (Non-Uniform Rational B-Spline), to represent copmplex ship surfaces, which seems to result in an overall smaller number of panels required. Other, though have had difficulties with preventing the increased computational requirements of NURBS geometry from slowing down their models [37].

Another method to limit sawtooth instabilities is to use a desingularized BEM model. This in fact has been quite common for modeling ship waves [38], and such models have been shown by Raven [39] to be more stable than non-desingularized BEM

models using simple elements.

Besides instabilities discussed above, which usually occur in free surface regions of high curvature, the most significant numerical instabilities occur at or near corners or edges of the computational domain, where different boundaries with different boundary conditions intersect, such as radiation boundaries (i.e., offshore or far field boundaries) and intersection between a surface piercing solid boundary and the free surface (such as a ship). Some of the problems at corners can be due to ill-posed boundary conditions and these can be removed by expressing extended continuity or compatibility conditions (e.g., Grilli and Svendsen [28]; Grilli and Subramanya [26]; Grilli et al. [35]).

For fully FNPF flows, there is no known general appropriate far-field condition to absorb outgoing waves. Hence, damping layers or absorbing beaches have been used instead. Cointe [40], for instance, made use of wave absorbers based on a free surface counter-acting pressure, which can be tuned to a particular wavelength, and Grilli and Horrillo have used an absorbing beach [31] combining such wave absorbers on the free surface and actively absorbing wavemakers on lateral boundaries. In light of this work, many authors have in fact used some portion of their computational domain to damp out spurious sawtooth instabilites that occurred near the domain edges, in a manner similar to simulating radiation of physical wave. Liu et al. [41], for instance, used a so-called sponge layer, which is similar to techniques that have been used since the early 1990s [42].

For completeness, other attempts at solving ship-wave problems have made use of the Navier-Stokes equations, but research using these techniques has developed more slowly, because of their much greater computational requirements. Notable early work includes Hino [43], who used a finite-difference approach to find the flow around various hullforms.

The model used in this study is similar to that used by Sung and Grilli [44], i.e.,

originally a two-dimensional FNPF model for water waves [27, 26], that was later extended to three-dimensions [35] and added a FMA by Fochesato and Dias [36]. As a Numerical Wave Tank (NWT), the model was used to study such problems as the breaking of three-dimensional (3D) shoaling waves [45], Guyenne and Grilli [46] and tsunami generation [47]. Expressing the governing equations in a coordinate system moving at the disturbance's speed, Sung and Grilli used the model to study waves caused by a moving pressure patch or a Wigley hulls [44]. They implemented and tested a variety of free-surface updating schemes [48] and tested the FMA as well. Here, we present similar wave simulations, with the difference that we concentrate on waves caused by a twin cushion, in much deeper water. Moreover, numerical results are interpreted with respect to our current understanding of the HSC-SES design, in order to both better understand and validate earlier results of tow tank experiments.

2.2 Methodology

The 3D-NWT domain is a rectangular box, with a free surface (Fig. 25), and length X_0, width W_0, and depth H_0. Each side of the NWT is discretized by a regular grid, with uniform node spacing in each direction (i.e., Δx, Δy, Δz). FNPF equations are modeled using a MEL time-updating scheme based on second-order explicit Taylor series expansions [35]. Thus, a first Laplace's equation is solved to compute the velocity potential at each boundary gridpoint, or collocation node, and then the position of the free surface nodes, as well their velocity potential, are updated in time using the Taylor series. As we shall see, this will require solving for the time derivatives of the potential, using a second Laplace's equations, whose boundary conditions will be obtained from the solution of the first problem.

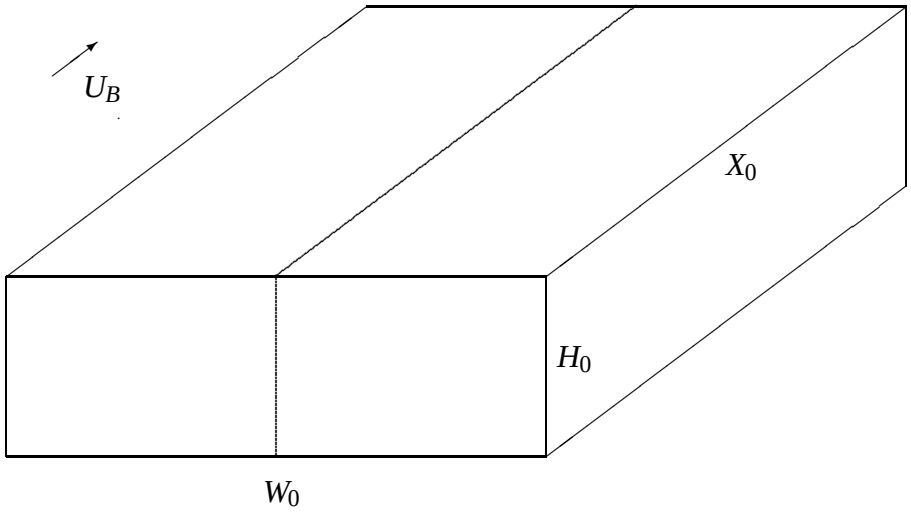

Figure 25. Schematic of 3D-NWT of length X_0, width W_0, and depth H_0, moving at speed $U_B(t)$ with the specified free surface disturbance.

2.2.1 Solving Laplace's equation

Laplace's equation is solved using a BEM approach, which has the advantage of only requiring the boundaries (i.e. free-surface, lateral boundaries, and the floor of the tank) to be discretized. The BEM is then accelerated using a FMA, which reduces the computation time to $O(N_\Gamma)$, where N_Γ is the number of discretized points (collocation nodes) over the boundary.

Boundary integral equation

According to FNPF equations, the fluid within the NWT is assumed to be incompressible, inviscid, and the motion to be irrotational. Hence, a velocity potential, Φ, is introduced such that the velocity field $\mathbf{u}$ is given by

$$\mathbf{u} = \nabla\Phi. \tag{19}$$

This velocity potential, because of mass conservation (i.e., continuity equation for incompressible fluids), obeys Laplace's equation

$$\nabla^2\Phi = 0 \tag{20}$$

within the domain, Ω.

This equation can be transformed usng Green's second identity into a Fredholm equation, which is the boundary integral equation (BIE) for this problem:

$$\alpha(\mathbf{x}_l)\Phi(\mathbf{x}_l) = \int_\Gamma \left(\frac{\partial \Phi(\mathbf{x})}{\partial n} G(\mathbf{x}, \mathbf{x}_l) - \Phi \frac{\partial G(\mathbf{x}, \mathbf{x}_l)}{\partial n} \right) d\Gamma(\mathbf{x}) \tag{21}$$

where n is the (outward) local normal direction at the boundary of the domain, Γ. The points, $\mathbf{x}_l$ at which the BIE is evaluated are the collocation nodes over the boundary. In 3D, the free-space Green's function for Laplace's equation is found as:

$$G(\mathbf{x}, \mathbf{x}_l) = \frac{1}{4\pi ||r||} \tag{22}$$

$$\frac{\partial G}{\partial n} = \frac{-1}{4\pi} \frac{\mathbf{r} \cdot \mathbf{n}}{||r||^3} \tag{23}$$

where $\mathbf{r} = \mathbf{x} - \mathbf{x}_l$, the vector between the collocation node and point $\mathbf{x}$, and $||r||$ is the distance between these points.

Mid-interval interpolation

In order to evaluate the BEM integrals over the boundary, the velocity potential, the normal derivative of the velocity potential, and the geometry are all expressed as polynomial functions, based on the mid-interval interpolation (MII) method, previously developed by Grilli and Submramanya [26] for two-dimensional problems. For 3D problems [35], s 3D-MII elements consists in a bidirectional isoparametric cubic interpolation (Fig. 26), based on the nearest 4-by-4 grid of nodes. In the integrations, only the middle segment of 4 nodes (black dots in the figure) is used at a time, and the element is slid to the next 4-by-4 node patch for further integrations. When reaching an edge, the MII segment becomes non-central and takes one of the other possible 8 positions on the element, depending on the case. As in the classical BEM, 3D-MII elements are expressed based on polynomial shape functions, defined in a curvilinear reference element $\Gamma_e(\xi, \eta)$, and nodal values of field variables (e.g. Φ, $d\Phi/dn$) or geometry (e.g. x, y, z),

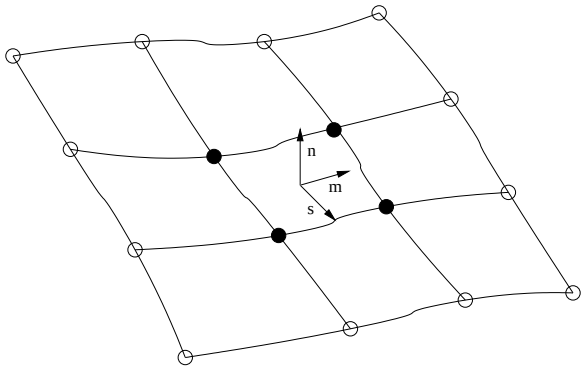

Figure 26. Definition of a 3D-MII element in Cartesian boundary coordinate system with indication of tangential and normal vectors at an arbitrary point., with : $(\circ)$ 4x4 overlapping element; $(\bullet)$ middle interval used in the integrations.

where typically the domain of variation (and hence limits of integration for a boundary integral) for both intrinsic coordinates, ξ and η, are from -1/3 to 1/3.

Integration techniques

Boundary integrals are primarily evaluated using a N_r-point Gauss-Legendre quadrature rule, over the arbitrary kernel F:

$$\int_{-1}^{+1}\int_{-1}^{+1} F(\xi,\eta)d\xi d\eta = \sum_{g=1}^{N_r}\sum_{h=1}^{N_r} w_g w_h F(\lambda_g,\lambda_h) \tag{24}$$

where w and λ refer to the Gauss weights and abscissa and where the limits of integration have been here remapped to be -1 to +1.

Weakly singular integrals, of the form

$$\int_{-1}^{+1}\int_{-1}^{+1} f(\xi,\eta)G(\mathbf{x}(\xi,\eta),\mathbf{x}_l)d\xi d\eta \tag{25}$$

are evaluated using a modified coordinate system [35], which gives:

$$\int_{-1}^{+1}\int_{-1}^{+1} f(\xi,\eta)G(\mathbf{x}(\xi,\eta),\mathbf{x}_l)d\xi d\eta = \frac{1}{64}\sum_{g=1}^{N_r}\sum_{h=1}^{N_r} w_g w_h \{r'^{12}_m F(r'^{12},\varphi^{12}) + r'^{23}_m F(r'^{23},\varphi^{23})\} \tag{26}$$

$$\varphi^{12} = \frac{\pi}{8}(1+\lambda_g) \tag{27}$$

$$\varphi^{23} = \frac{\pi}{8}(3+\lambda_g) \tag{28}$$

$$r'^{12}_m = \frac{2}{\cos\varphi^{23}} \tag{29}$$

$$r'^{23}_m = \frac{2}{\sin\varphi^{12}} \tag{30}$$

$$r'^{12} = \frac{r'^{12}_m}{2}(1+\lambda_h) \tag{31}$$

$$r'^{23} = \frac{r'^{23}_m}{2}(1+\lambda_h) \tag{32}$$

This singular integration technique is in contrast to the PART (project and angular and radial transformation) method of Hayami and Matsumoto [49].

A third, adaptive, integration technique is required to improve the accuracy of quasi-singular integrals, which may occur depending on the distance and intercept angle between the collocation node and boundary element [50]. Depending on the distance and angle between a given collocation node and element, the element is split S times into 4^S parts, where $S \leq S_{max}$. Each sub-boundary integral over the element is then evaluated using regular Gauss-Legendre quadrature. See Grilli et al. [35] for more detail. A similar quasi-singular integral technique was first developed by Grilli and Svendsen [28] and later more extensively tested by Grilli and Subramanya [50], who showed that numerical errors, particularly in corners, can be decreased by orders of magnitude when a quasi-singular integral technique is used.

Fast multipole acceleration

The FMA used here follows from the work of Yoshida [51], which is similar to the FMA described and implemented by Fochesato [52] and Fochesato and Dias (2006) in this 3D model. The fast multipole method involves calculating the influence of different groups of elements using multipole expansions, which for the free-space Green's function are spherical harmonics:

$$G(\mathbf{x},\mathbf{x}_l) \approx \frac{1}{4\pi}\sum_{k=0}^{p}\sum_{m=-k}^{k}\rho^k Y_k^{-m}(\alpha,\beta)\frac{Y_k^m(\theta,\phi)}{r^{k+1}} \tag{33}$$

$$Y_k^{-m}(\alpha,\beta) = \sqrt{\frac{(k-|m|)!}{(k+|m|)!}}P_k^{|m|}(\cos\alpha)e^{-im\beta}, k \geq 0, |m| \leq k \tag{34}$$

$$P_k^m = \frac{(-1)^m}{2^k k!}(1-x^2)^{m/2}\frac{d^{k+m}(x^2-1)^k}{dx^{k+m}}, k \geq 0, 0 \leq m \leq k \tag{35}$$

where (ρ,α,β) and (r,θ,ϕ) are here the spherical coordinates for $\mathbf{x}$ and $\mathbf{x}_l$ (for the rest of the manuscript, ϕ will represent a velocity potential). This representation of the Green's function is used to compute far-field interactions between different parts of the computational domain.

The computational efficiency of a FMA is strongly dependent on grouping boundary elements so that distance criteria for deciding on near- or far-field comuputations is automated. The computational domain, which fits within a cube, is split into eight sub-domains, and each of those sub-domains are further divided, up to some level l; this hierarchical structure is called an octree. Near-field interactions, between nodes and elements of the same leaf of the octree, are as described before, i.e., based on the free space Green's function and its direct integration. Interactions located further away involve integrations using the multipole expansions, which do not involve any ingularity. See Fochesato [52] and Fochesato and Dias [36], for more details.

The BIE for N_Γ points, when discretized, forms a linear system of equations which is solved using a restarted version of Saad and Schultz's GMRES method [53], which, when memory requirements are unimportant, is the fastest known iterative matrix solver.

Like any iterative solver, GMRES stops when the residual of the solution is less than a pre-specified error ε. GMRES-*m* (which is restarted every *m* iterations) does not require manipulation of the system matrix itself but only relies on products of the system matrix with arbitrary vectors. When the FMA is applied, then, it replaces these matrix-vector products with evaluations using FMA approximations. In this way, the standard $O(N_\Gamma^2)$ memory storage requirement of a linear system is avoided, and the largest memory requirement becomes the size of SSOR (with relaxation parameter ω), the preconditioning matrix. The use of a preconditioning scheme for the GMRES reduces the calculation time for the problem enough to outweigh any disadvantage of the added memory requirements.

2.2.2 Time-updating the free-surface

The position of the free-surface nodes is updated by applying the FNPF free surface boundary conditions and applying an explicit second-order time integration scheme. After each time step, the nodes are regridded to the original regular grid in order to prevent node clustering.

Free-surface boundary conditions

The kinematic and dynamic boundary conditions on the free-surface are

$$\frac{D\mathbf{x}}{Dt} = \nabla\Phi \tag{36}$$

$$\frac{D\Phi}{Dt} = -gz + \frac{1}{2}|\nabla\Phi|^2 - \frac{p}{\rho} \tag{37}$$

respectively, where $\mathbf{x}$ is a point on the free-surface, g is the acceleration of gravity, p is the applied (air) pressure, and ρ is the density of the water. The Lagrangian or material time derivative is given by:

$$\frac{D}{Dt} = \frac{\partial}{\partial t} + \nabla\Phi \cdot \nabla \tag{38}$$

which is a natural representation for a BEM model, since each collocation node can be advected with the flow, using a time-integration, to be discussed below.

Sliding elements

Using the free-surface boundary conditions, the position of the collocation nodes on the free-surface are updated after evaluating the local gradients of quantities such as the velocity potential. To be computationally efficient, this is not done using another boundary integral, but rather with a 4th-order sliding polynomial, first introduced in their two-dimensional model by Grilli et al. [27] and later used in the 3D-NWT [35].

The sliding elements are a different discretization than the MII elements, in that the nearest 5-by-5 grid of collocation nodes is used derivatives, the isoparameters ξ and η are used to setup a new set of coordinates (s,m,n) (Fig. 26):

$$\mathbf{s} = \frac{\partial \mathbf{x}/\partial \xi}{|\partial \mathbf{x}/\partial \xi|} \tag{39}$$

$$\mathbf{m} = \frac{\partial \mathbf{x}/\partial \eta}{|\partial \mathbf{x}/\partial \eta|} \tag{40}$$

$$\mathbf{n} = \frac{\mathbf{s}\times\mathbf{m}}{|\mathbf{s}\times\mathbf{m}|} \tag{41}$$

Expressions for the tangential $(\mathbf{s},\mathbf{m})$ vectors and other tangential derivatives were first given in [35] for orthogonal systems (s,m,n), and later extended to non-orthogonal systems by Fochesato et al.[54].

Second-order time integration

Time integration for the model uses a second-order Taylor's expansion, both for the collocation node position and the velocity potential [27, 35]:

$$\mathbf{x}(t+\Delta t) = \mathbf{x}(t) + \Delta t \frac{D\mathbf{x}}{Dt} + \frac{(\Delta t)^2}{2}\frac{D^2\mathbf{x}}{Dt^2} + O\left((\Delta t)^3\right) \tag{42}$$

$$\Phi(t+\Delta t) = \Phi(t) + \Delta t \frac{D\Phi}{Dt} + \frac{(\Delta t)^2}{2}\frac{D^2\Phi}{Dt^2} + O\left((\Delta t)^3\right) \tag{43}$$

In order to compute the acceleration of a fluid particle, though, it is necessary to

evaluate ϕ_{nn}, the second-order partial derivative with respect to the normal of the free-surface, which is not a priori known from the velocity potential and its normal derivative. This can be done by applying Laplace's equation on a sliding element:

$$\phi_{nn} \approx -\phi_{ss} - \phi_{mm} + \phi_s(\mathbf{x}_{ss} \cdot s + \mathbf{x}_{mm} \cdot s) + \phi_m(\mathbf{x}_{ss} \cdot m + \mathbf{x}_{mm} \cdot m) + \phi_n(\mathbf{x}_{ss} \cdot n + \mathbf{x}_{mm} \cdot n) \quad (44)$$

which is an orthogonal approximation of the complete formula derived by Fochesato et al [54]. The approximation used here requires that the free-surface elements are not highly distorted, which is suitable for a ship wave problem, particularly since regridding is applied after each time step.

Translated coordinate system

In order to reduce the size of the computational domain and speed up calculations, the free-surface boundary conditions are applied to a domain moving at the same speed as the pressure patch. Similarly, rather than using the true velocity potential, Φ, we classically define ϕ, as the disturbance potential such that:

$$\Phi = U_B(t)x + \phi \quad (45)$$

so the appropriate far-field boundary conditions on the upstream, downstream, and side-wall boundaries (Γ_u, Γ_d, Γ_s), as well as the bottom boundary (Γ_h) are

$$\frac{\partial \phi}{\partial n} = 0 \quad (46)$$

The *xyz*- and *t*-coordinates are thus replaced by x', $y' = y$, $z' = z$ and $t' = t$, where

$$x'(t') = x(t') + \int_0^{t'} U_B(t)dt \quad (47)$$

From here on, the primes will be dropped for convenience.

Following Sung and Grilli [44], a pseudo-Lagrangian derivative is used so that collocation nodes maintain their position relative to the *x*-axis of the NWT (i.e., the

representation is Eulerian in x, and z and Lagrangian in y); this pseudo-Lagrangian operator is defined as

$$\frac{\tilde{D}}{\tilde{D}t} = \frac{\partial}{\partial t} + w_f^y \frac{\partial}{\partial y} + w_f^z \frac{\partial}{\partial z} \tag{48}$$

$$w_f^x = U_B(t) \tag{49}$$

$$w_f^y = \frac{\partial \phi}{\partial y} \tag{50}$$

$$w_f^z = \frac{\partial \phi}{\partial z} + \zeta_x \{U_B - \frac{\partial \phi}{\partial x}\} \tag{51}$$

where ζ is the free-surface elevation.

The appropriate free-surface boundary conditions using pseudo-Lagrangian updating is then:

$$\frac{\tilde{D}\mathbf{x}}{\tilde{D}t} = w_f^y \mathbf{j} + w_f^z \mathbf{k} \tag{52}$$

$$\frac{\tilde{D}\phi}{\tilde{D}t} = -gz - \frac{1}{2}|\nabla\phi|^2 - \frac{p_a}{\rho} + \mathbf{w}_f \cdot \nabla\phi \tag{53}$$

where $\mathbf{j}$, $\mathbf{k}$ are the unit vectors in the y and z directions, respectively.

Damping and regridding

If the model is run as described, instabilities spontaneously form at the leading edge of the domain, which need to be locally damped in order to provide meaningful results. Since earlier work with the model has shown that it is very stable for highly nonlinear wave computations [35], these instabilities are interpreted here as artifacts due to the moving coordinate system, which upstream, in the near absence of waves, leads to specifying that nodes essentially move horizontally with velocity $u = U_B$, thus creating a very unstable situation similar to the initiation of a Kelvin-Helmholtz instability.

The appearance of instabilities at the leading edge of the domain is eliminated using an adjustment of the velocity potential for all points where $x < x_d$:

$$\frac{\tilde{D}^d}{\tilde{D}^d t} = \left(\frac{\tilde{D}}{\tilde{D}t} - \nu^d\right) \tag{54}$$

which is known as a sponge layer or damping pressure (analytically, in a linear framework, the $-\nu^d$ would provide exponential damping in time of the solution). Note that such an adjustment of the solution will have minimal effects when instabilities are nearly inexistent and will only affect the solution upstream of the disturbance where results are of no practical interest.

Also, at each time step, the free-surface nodes are regridded using MII elements, by resetting the *y*-axis position of all of the nodes and recalculating all the field variables by interpolation on the BEM elements; hence the shape of the free surface is not modified and this does not constitute smoothing proper, but just a suitable reinterpolation of the same solution. For all nodes on the interior, regridding involves a simple interpolation. For nodes on the sidewalls, it could result in an extrapolation (e.g., if the sidewall nodes are moving inwards).

2.2.3 Evaluation of integral properties

Wave resistance

For a simple pressure patch, wave resistance can be computed simply from the free surface elevation based on integrating the specified cushion pressure, projected in the *x* direction [12]:

$$D_W = \int p \frac{\partial \zeta}{\partial x} dS \tag{55}$$

where $\partial\zeta/\partial x$ denotes the free surface slope in the *x* direction. D_W is often expressed as a wave resistance coefficient, C_W defined as:

$$C_W = \frac{D_W}{W} \frac{\rho g a}{p_0} \tag{56}$$

where W is the displacement of the SES, $\bar{p}$ the spatially averaged cushion pressure and a the cushion half length. Note that for twin rectangular patches of dimension $(2a, 2b)$, we have $W = 8\bar{p}ab$.

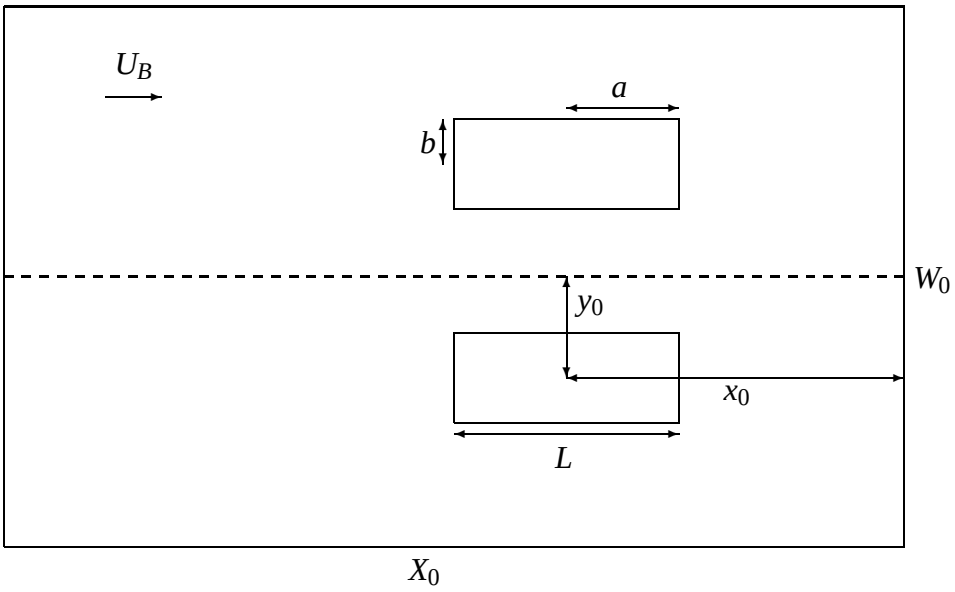

Figure 27. Parameters for twin moving pressure patch problem.

Energy and volume conservation

Once achieving steady-state, the 3D-NWT should have a constant potential energy, U, and kinetic energy, K; in potential flow theory, these are simply calculated as:

$$U = \frac{1}{2}\rho \int\int z^2 dxdy \tag{57}$$

$$K = \int \phi \frac{\partial \phi}{\partial n} dS \tag{58}$$

where S denotes the free surface.

Volume conservation can be checked by calculating the total volume of the NWT as:

$$V = \int\int (z + H_0) dxdy \tag{59}$$

which should remain nearly constant.

2.3 Results

Three test cases were considered, corresponding to three main configurations of the HSC-SES tow tank tests performed at IMD (see first mansucript). The applied pressure

in the modeled twin cushions was defined similar to Doctors and Sharma's [12], as (Fig. 27):

$$p_a = M(t)\frac{p_0}{4}\left(\tanh\alpha(x-x_0+a)-\tanh\alpha(x-x_0-a)\right) \times \left(\tanh\beta(|y|-y_0+b)-\tanh\beta(|y|-y_0-b)\right) \tag{60}$$

where $M(t)$ is a time ramp-up function $\in [0,1]$, p_0 is nearly the maximum pressure at steady state, x_0 and y_0 refer to the coordinates of the cushion centers, a and b are the half-length and width of the pressure patches in the x and y directions, respectively, and α and β are fall off parameters (related to how sharp the pressure gradients are on the edges of the moving pressure patches).

In order to reduce the transient waves that are generated at the start of computations, both the maximum pressure and the velocity of the pressure patches were smoothly varied from zero to steady-state test conditions over a time T_m as:

$$M(t) = \frac{1}{2}\left(1-\cos\frac{\pi t}{T_m}\right) \tag{61}$$

$$U_B = U_B^{max} M(t) \tag{62}$$

The maximum pressure p_0 was similarly varied. Based on numerical tests, we specified $T_m = 40\Delta t$, i.e., equal to the first 40 time steps of computations after which both velocity U_B and pressure p_0, remained steady.

The NWT parameters, such as size, discretization, and solution method, were specified identical for each test case (Table 13), and between test cases, only the pressure patch velocity and time-step magnitude were altered. For the computations, all parame-

Table 13. Main NWT parameters used for numerical test cases (dimensionless values)

Geometry	X_0	18.0
	W_0	3.077
	H_0	9.42
Discretization	Δx	0.222
	Δy	0.0684
	Δz	0.3768
	N_Γ	14,996
BEM	N_r	4
	S_{max}	2
FMA	p	8
	l	5
	cube center	(12.0, 0.0, 0.0)
	cube length	24.0
GMRES-m	m	100
	ε	10^{-10}
	ω	0.6

ters were nondimensionalized, specifying $a = 1$, $g = 1$, and $\rho = 1$:

$$x^* = x/a \tag{63}$$

$$t^* = t\sqrt{g/a} \tag{64}$$

$$\phi^* = \frac{\phi}{a\sqrt{ga}} \tag{65}$$

$$p^* = \frac{p}{\rho g a} \tag{66}$$

Using the cushion dimensions from experiments performed at IMD, i.e., $a_m = 0.745$ m and $b_m = 0.115$ m (see manuscript one), we find in dimensionless form, $a = 1$ and $b = 0.1538$. For the IMD model, we had, for a displacement of $W_m = 445$ N, a wave-making drag of $D_W = 28.7$, 16.4, and 9.3 N at speeds $U = 4$, 6 and 8 m/s respectively, which correspond to non-dimensional speeds of 1.48, 2.22, and 2.96; these speeds will be selected as pressure patch velocities for our three test cases. The average pressure needed to support the IMD model's displacement, using only the cushions, is $p_0 = 649.3$

Table 14. Main dimensionless variables for moving pressure patches used for test cases.

	Case 1	Case 2	Case 3
p_0	0.090	0.090	0.090
a	1.000	1.000	1.000
b	0.1538	0.1538	0.1538
α	5	5	5
β	10	10	10
W	0.08	0.08	0.08
x_0	5.4362	5.4362	5.4362
y_0	0.3077	0.3077	0.3077
Δt	0.06	0.04	0.03
U_B	1.48	2.22	2.96
x_d	3.0	3.0	3.0
ν^d	10.0	10.0	10.0

N/m^2 or 0.090 in non-dimensional form.

For each case, the transient NWT free-surface shows a classic Kelvin wave pattern (ref. Newman) within the first couple hundred timesteps (Figs. 28,29,30). Notice that because of the finite depth, changes in patch velocity induce changes in the angle of the Kelvin wake. For case 1, we also see that the wake intersects the sidewalls of the NWT at large time (Fig. 31).

The quasi-steady wave resistance coefficient was computed as $C_W = 0.909$, 0.667, and 0.469, for test case 1, 2, and 3, respectively (Fig. 32).

The NWT never achieved a fully stable steady-state for case 1; in fact, the model was initially set to run for 500 timesteps for each test case, but case 1 stopped after 341, because of numerical instabilities growing near the sidewalls (Fig. 33). Before then, however, the kinetic and potential energies achieved quasi-steady state for all test cases (Figs. 34,35). Volume conservation in the NWT was quite accurate (for $t \leq 5.0$), at better than 0.01% in relative absolute value (Fig. 36).

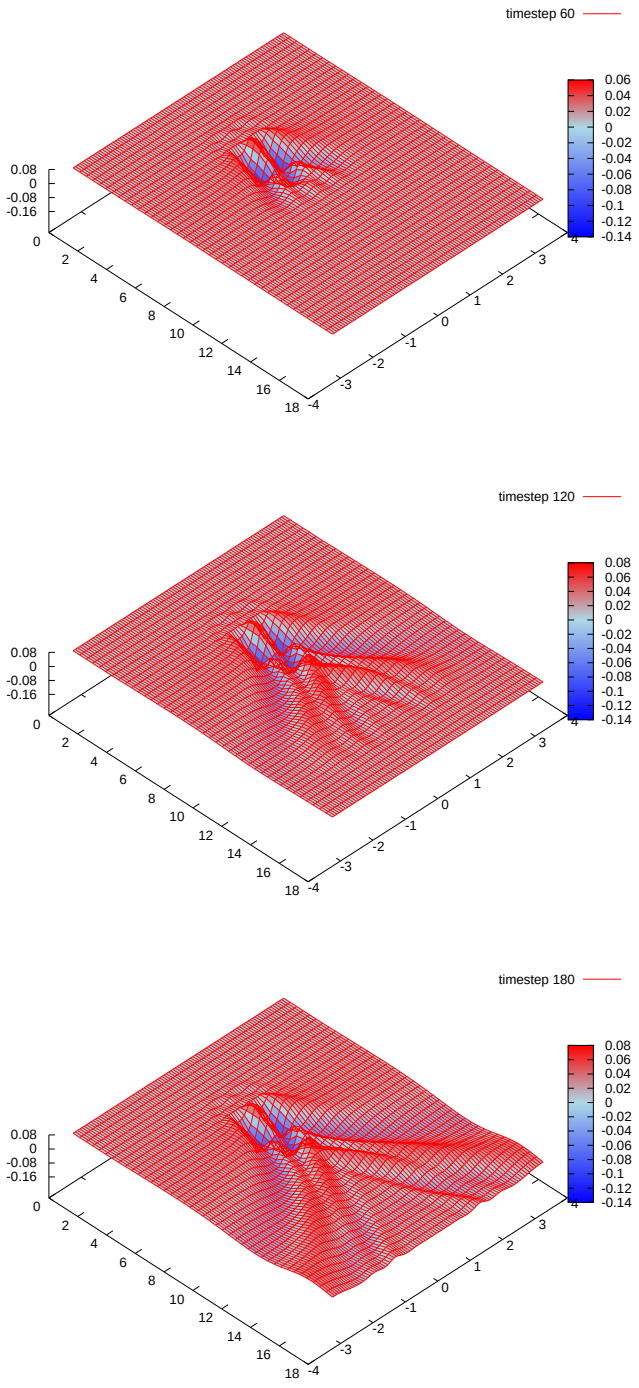

Figure 28. Evolution of free-surface for case 1 for t= 3.6, 7.2, and 10.8.

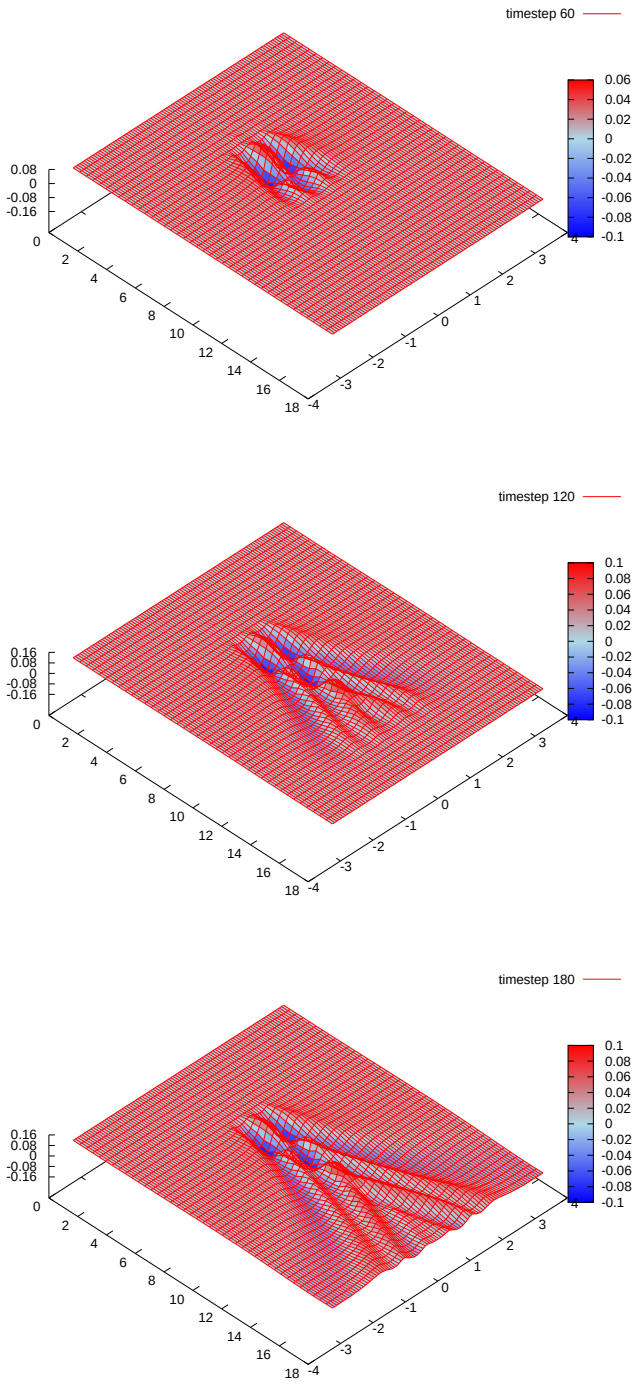

Figure 29. Evolution of free-surface for case 2 for t= 2.4, 4.8, and 7.2.

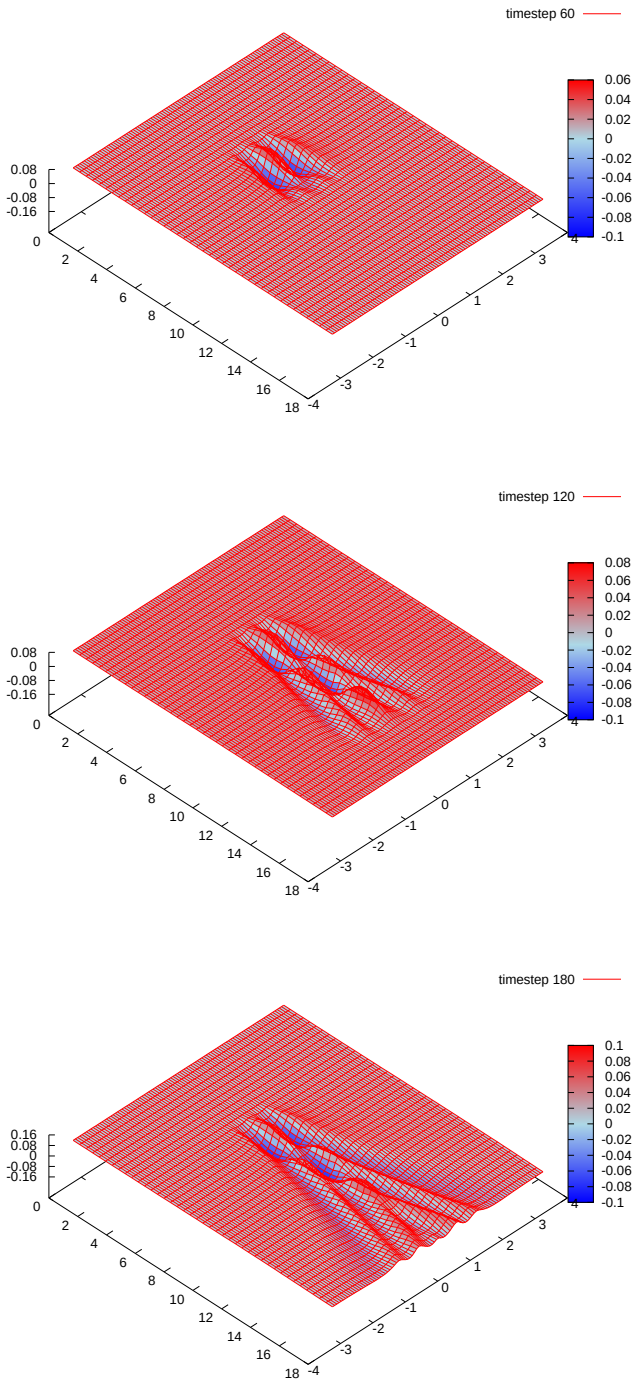

Figure 30. Evolution of free-surface for case 3 for t= 1.8, 3.6 and 5.4.

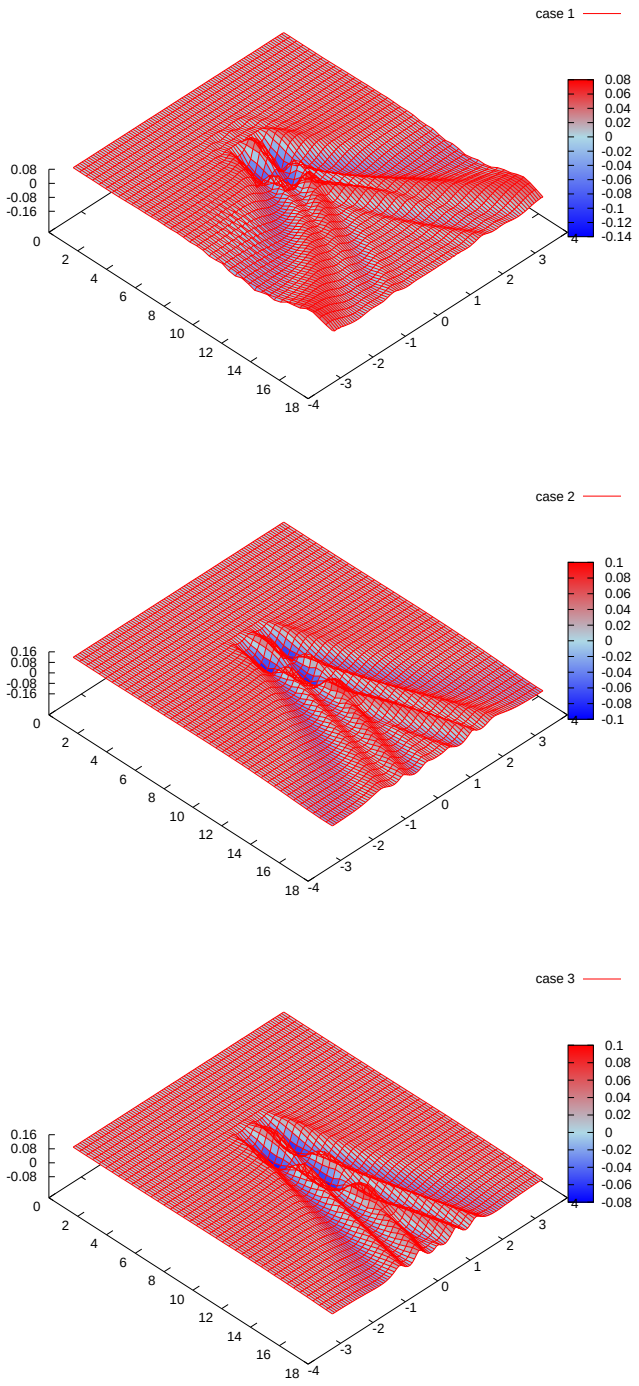

Figure 31. Quasi-steady free-surface established after 300 timesteps for each case (for t= 18, 12, and 9, respectively).

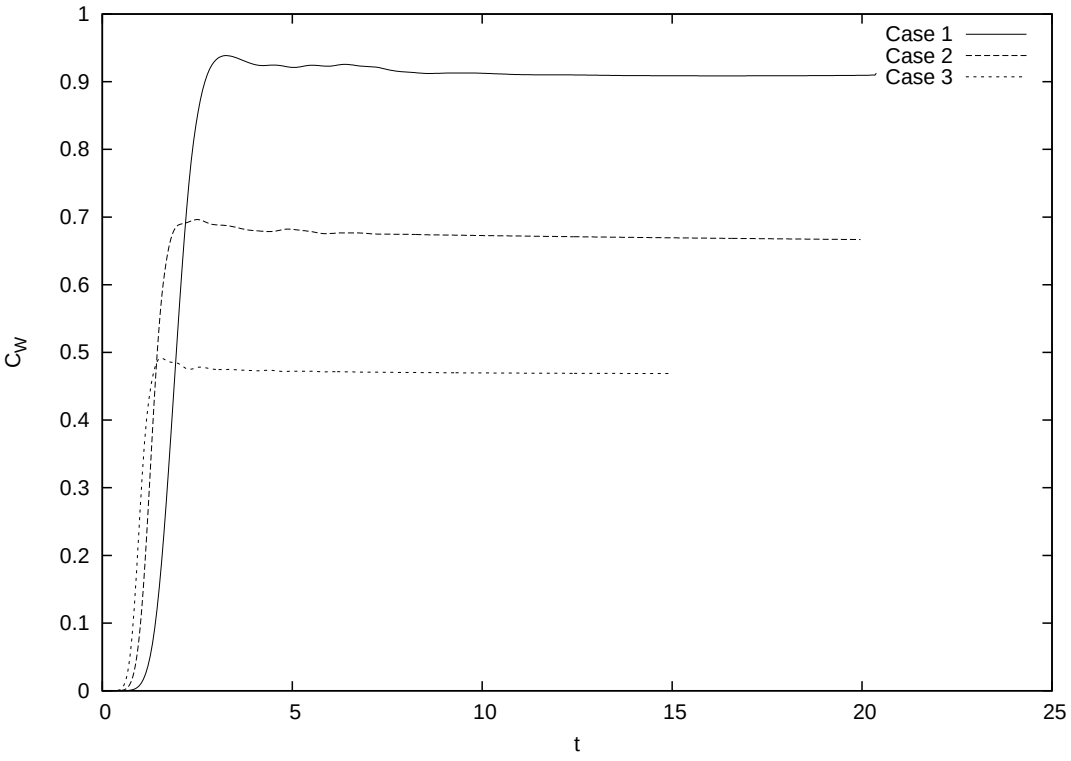

Figure 32. Wave resistance coefficient for each test case.

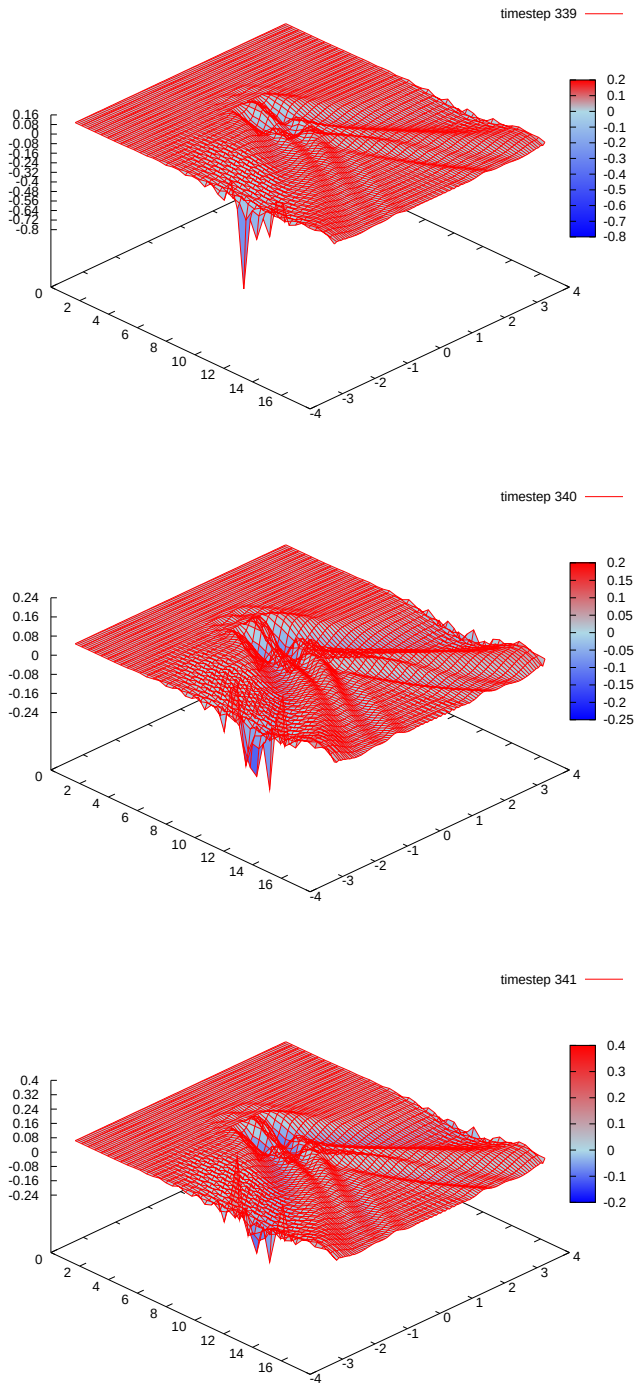

Figure 33. Close-up of instabilities for the last three timesteps (339–341) of case 1.

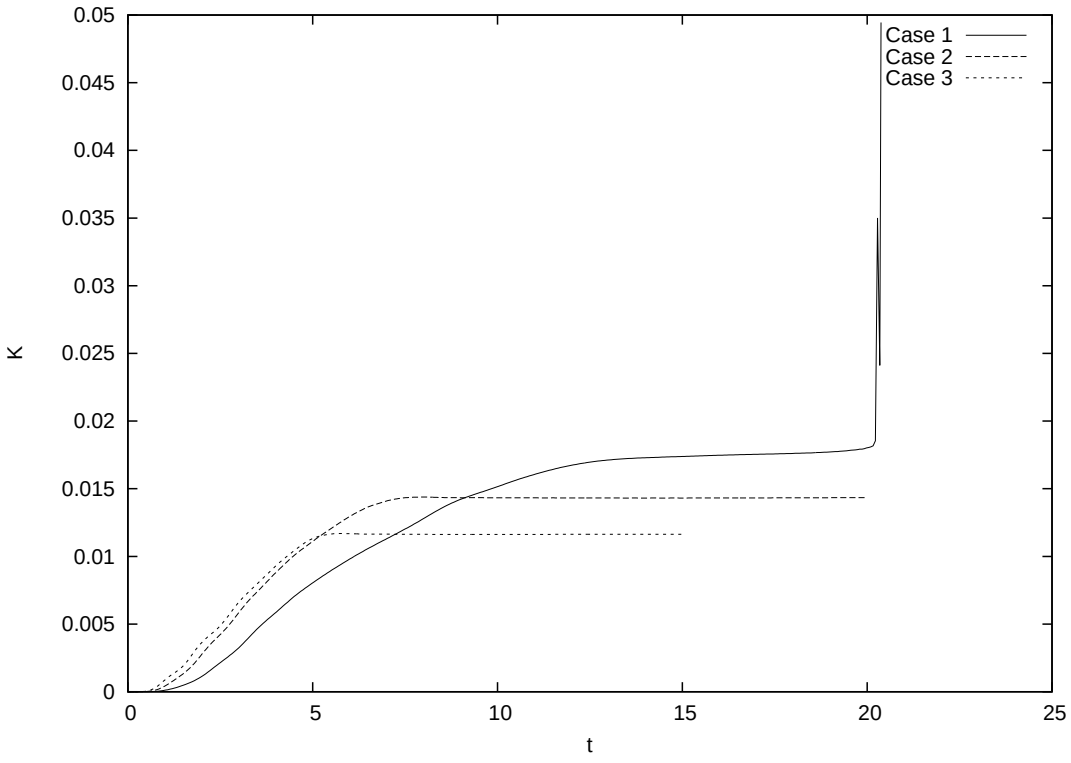

Figure 34. Kinetic energy of NWT for each test case. Note the instability in case 1 at the end of the test run.

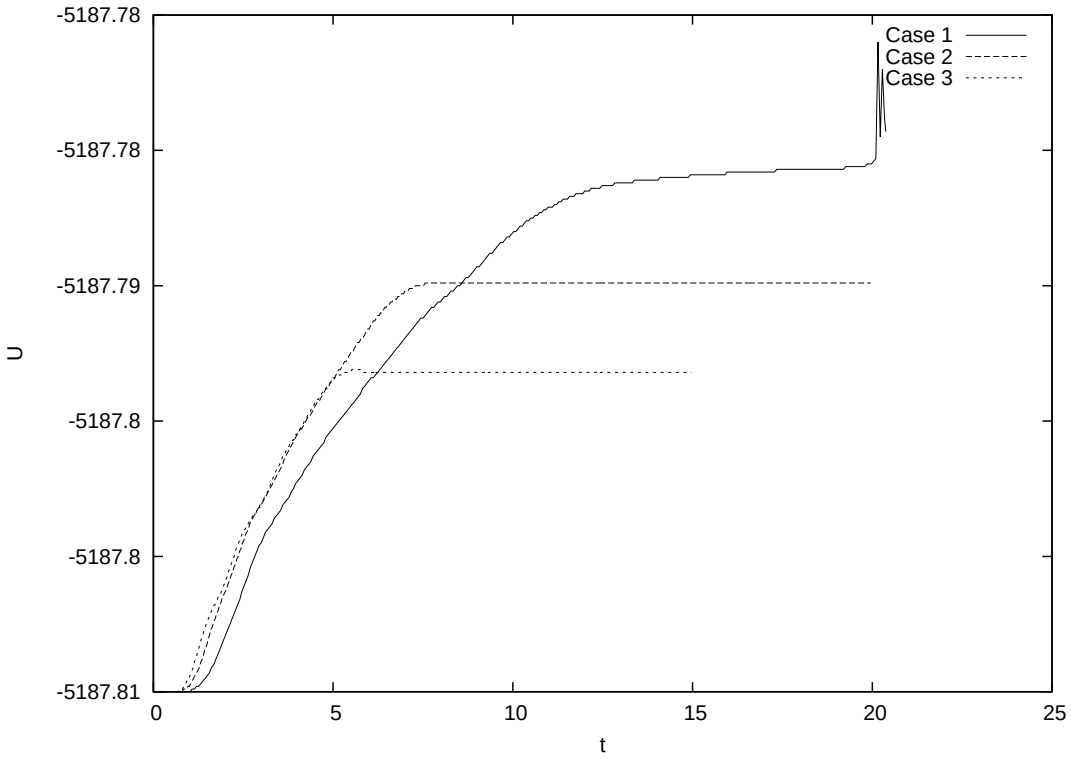

Figure 35. Potential energy of NWT for each test case. Note the instability in case 1 at the end of the test run.

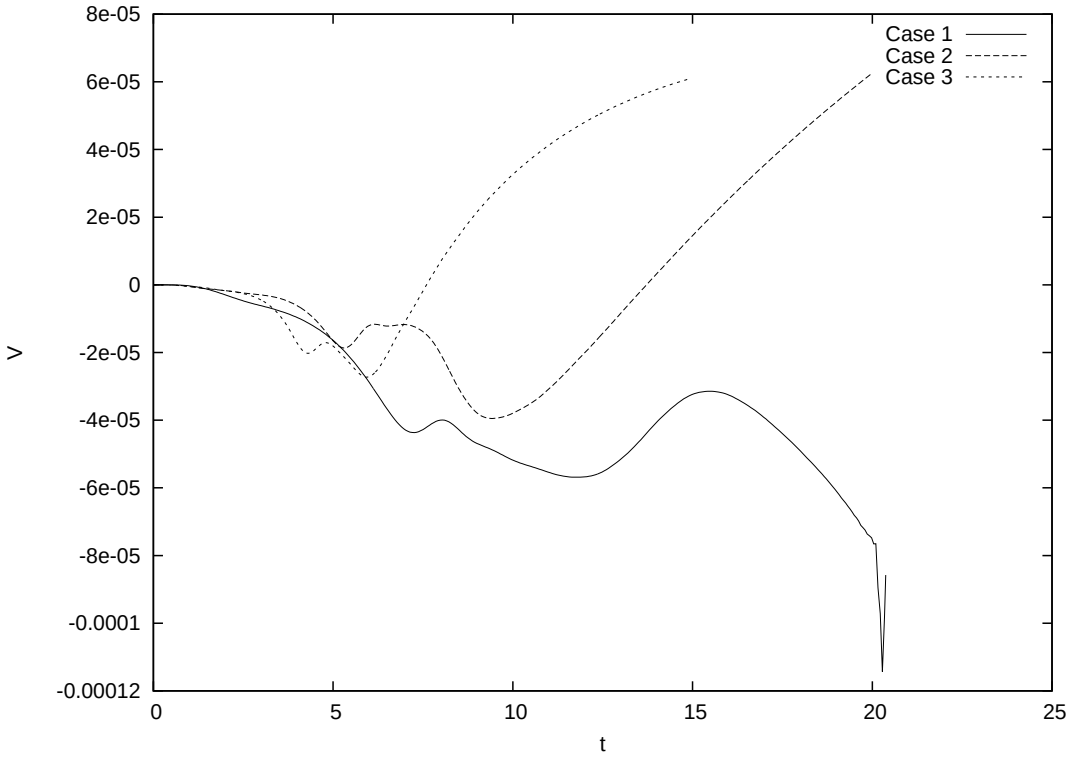

Figure 36. Relative volume change to NWT for each test case (i.e., ratio of difference in NWT volume from initial conditions to the initial NWT volume).

2.4 Discussion

2.4.1 Model spin-up

In all three cases, we see that the NWT becomes quasi-steady around $t = 5T_m$ (or 200 time steps), after the pressure patch reaches a steady speed. The Kelvin wave patterns produced seem physically reasonable, and vary with speed because of the finite depth of the tank. The total energy of the NWT also reaches quasi-steady state (until instabilities become an issue for case 1).

The numerical calculations for this problem are particularly demanding, since the depth of the tank is so great (i.e., nearly 10 m deep) and the resolution desired for the free-surface solution is quite fine (i.e., between 1 and 10 cm). The memory required for one of these simulations is approximately 3 GB.

2.4.2 Long-term stability

For case 1, the model becomes unstable during the simulation. Case 1 is the slowest of the test cases, and has the widest wake, which intersects with the NWT sidewalls. One possible explanation is that the MII regridding procedure at the sidewalls causes a slight extrapolation, amplifying small disturbances, should the sidewall nodes be trying to move towards the interior of the domain. Also a free-surface translating at the patch velocity near a fixed sidewall could cause instabilities of the sort seen at the leading edge of the domain, due to Kelvin-Helmholtz instabilities, which are damped using the sponge layer. Perhaps numerical dissipation added to the time-stepping scheme near sidewalls would provide a more stable solution.

These numerical instabilities were not seen by Sung and Grilli [44]. One possible explanation is that because for the cases in this manuscript, the discretization of the sidewalls is much finer; the coarse discretization of Sung and Grilli's work may have resulted in the inability of short waves to be numerically modeled. Sung and Grilli [55] studied the accuracy of the BEM model used here, and found that short wavelengths

were less accurate.

Inaccuracies in volume conservation are more difficult to explain, but it is possible that longer test runs, combined with finer discretization, would resolve the problem. Memory and computational requirements for a finer discretization, however, are substantial.

2.4.3 Experimental comparison

The free-surface elevation is the most straightforward variable to compare between the numerical and experimental HSC-SES results (Fig. 37). A simple visual comparison shows that the two are relatively similar, though in every case the numerical results have a free surface that is not as depressed as the experimental result. This could be a result of using a mostly constant pressure within the air cushions in the numerical computation as opposed to the real situation, where the air pressure would be higher at the bow. The difficulty in fixing the numerical model would be determining the appropriate pressure distribution to use.

Wave resistances can be calculated from NWT results for the three cases, taken at steady state using the cushion dimensions. In dimensional form, we find $D_W = 18.3$, 13.4, and 9.5 N, respectively. compared to the IMD results of $D_W = 28.7$, 16.4, and 9.3 N. Despite some approximations in the computational parameters (such as the average pressure), and the absence of a hull in computations, the wave resistances calculated match quite well those calculated from IMD test data, especially considering no attempt was made to match the NWT pressure patch distribution to that occurring within an actual HSC-SES, beyond geometrical constraints.

Also notice that the pressure distribution used had a smoothly-varying y-axis distribution, whereas for an HSC-SES, with rigid sidewalls, the pressure dropoff would be much sharper. This cannot be modeled with a FNPF model lacking sidewalls, because an infinitely sharp pressure gradient would cause the free-surface to break.

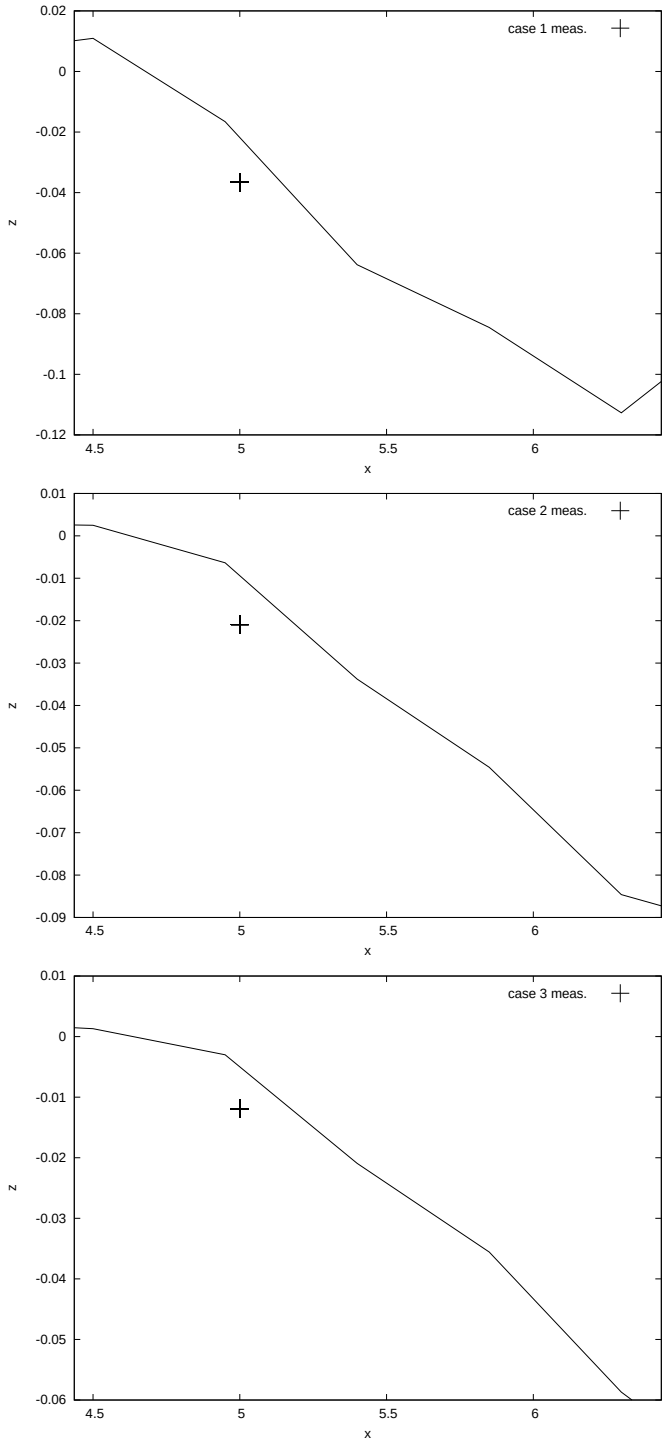

Figure 37. Comparison of quasi-steady state NWT free-surface elevation (z) within starboard pressure patch with experimentally measured water surface wave height (at $x = 5.0$) for cases 1–3. Notice the coarseness of the discretization.

The results of this comparison show the importance of including all elements of an HSC-SES into any computational model. While the wave resistance of a moving pressure patch may be calculated correctly, details such as sidewalls and correct pressure distributions are needed to properly understand the physics of an HSC-SES.

2.5 Summary

Numerical wave tank results for twin moving pressure patches were obtained which roughly correspond to towing tank test data for the Harley surface effect ship. Using a pseudo-Lagrangian formulation, combined with a fast multipole algorithm, memory and computational requirements were reduced to permit test cases of nearly 15,000 nodes. Experimental results showed reasonable agreement for the quasi-steady results of the numerical tests.

The importance of these results is that the wavemaking drag is the one aspect of ship resistance that is nontrivial to estimate for an SES, even crudely. Other aspects of the drag (e.g., frictional, air) can be estimated once basic pieces of information about the ship are known (e.g., wetted surface area). However wavemaking drag of a ship is extremely difficult to estimate without experimental or numerical modeling of the specific hullform.

In these calculations, the nonlinearity of the NWT was not particularly important, and in fact the additional complexity probably hindered getting results, particularly in computational time. However, if a more complete model of the HSC-SES was made (i.e., including a rigid hull with a correct pressure distribution), then a nonlinear free-surface boundary condition would be important – this manuscript represents continuing progress in developing a fully-nonlinear potential flow model that can be used in a variety of applications.

List of References

[1] C. B. McKesson, "Hull form and propulsor technology for high speed sealift," in *High-Speed Sealift Technology Workshop*. Center for the Commercial Deployment of Transportation Technology, 1998.

[2] E. Butler, "The surface effect ship," *Naval Engineers Journal*, vol. 97, pp. 200–260, 1985.

[3] P. Mantle, *Air cushion craft development*. David Taylor Naval Ship Research and Development Center, 1980, no. 80/012.

[4] F. Wilson, P. Viars, and J. Adams, *Feasibility design for a surface effect catamaran corvette escort*. American Institute of Aeronautics and Astronautics, 1983, no. 619.

[5] M. Bebar and D. Liberatore, *U.S. Navy high performance ship concept formulation*. American Institute of Aeronautics and Astronautics, 1983, no. 626.

[6] F. Wilson and P. Viars, *The surface effect catamaran - a sea capable small ship*. American Institute of Aeronautics and Astronautics, 1981, no. 2076.

[7] F. Wilson, P. Viars, and J. Adams, "Surface effect catamaran – progress in concept assessment," *Naval Engineering Journal*, vol. 95, no. 3, pp. 301–311, May 1983.

[8] J. Durkin and N. Paraskevas, *Progress in the development of the surface effect catamaran (SECAT)*. American Institute for Aeronautics and Astronautics, 1986, no. 2364.

[9] H. Harley, "Surface effect vessel hull," U.S. Patent 5 570 650, 1996.

[10] J. Michell, "The wave resistance of a ship," *Philosophical Magazine*, vol. 45, pp. 106–123, 1898, series 5.

[11] T. Havelock, "Wave resistance," in *Proceedings of the Royal Society of London*, vol. A118, 1928, pp. 24–33.

[12] L. Doctors and S. Sharma, "The wave resistance of an air-cushion vehicle in steady and accelerated motion," *Journal of Ship Research*, vol. 16, pp. 248–260, 1972.

[13] J. Newman, "Evaluation of the wave-resistance green function: Part 1 – the double integral," *Journal of Ship Research*, vol. 31, pp. 79–90, 1987.

[14] E. Tuck, D. Scullen, and L. Lazauskas, "Wave patterns and minimum wave resistance for high-speed vessels," in *Proceedings of the 24th Symposium on Naval Hydrodynamics*, Kukuoka, Japan, 2002.

[15] J. Hess and A. Smith, "Calculation of nonlinear potential flow about arbitrary three-dimensional bodies," *Journal of Ship Research*, vol. 8, no. 2, pp. 22–44, 1964.

[16] C. Dawson, "A practical computer method for solving ship-wave problems," in *Proceedings of the Second International Conference on Numerical Ship Hydrodynamics*, Berkeley, CA, USA, 1977, pp. 30–38.

[17] Y. Huang and P. Sclavounos, "Nonlinear ship motions," *Journal of Ship Research*, vol. 42, pp. 120–130, 1998.

[18] L. Greengard and V. Rokhlin, "A fast algorithm for particle simulations," *Journal of Computational Physics*, vol. 73, pp. 325–348, 1987.

[19] D. Sen, "Numerical simulation of motions of two-dimensional floating bodies," *Journal of Ship Research*, vol. 37, pp. 307–330, 1993.

[20] G. Jensen and V. Bertram and H. Söding, "Ship wave-resistance computations," in *Proceedings of the Fifth International Conference on Numerical Ship Hydrodynamics*, Hiroshima, Japan, 1989.

[21] S. Scorpio, *Fully nonlinear ship-wave computations using a multipole accelerated desingularized method*. Ann Arbor: Ph.D. dissertation, University of Michigan, 1997.

[22] M. Longuet-Higgins and E. Cokelet, "The deformation of steep surface waves on water. i. a numerical method of computation." in *Proceedings of the Royal Society of London*, vol. A350, 1976, pp. 1–26.

[23] D. Sen, J. Pawlowski, J. Lever, and M. Hinchey, "Two-dimensional numerical modelling of large motions of floating bodies in waves," in *Proceedings of the Fifth International Conference of Numerical Ship Hydrodynamics*, Hiroshima, Japan, 1989, pp. 351–373.

[24] M. Xue and H. Xü and Y. Liu and D.K.P. Yue, "Computations of fully nonlinear three-dimensional wave-wave and wave-body interactions. part 1. dynamics of steep three-dimensional waves." *Journal of Fluid Mechanics*, vol. 438, pp. 11–39, 2001.

[25] C.-E. Janson, *Potential flow panel methods for the calculation of free-surface flows with lift*. Göteborg, Sweden: Ph.D. dissertation, Chalmers Univ., 1997.

[26] S. Grilli and R. Subramanya, "Numerical modeling of wave beraking induced by fixed or moving boundaries," *Computational Mechanics*, vol. 17, pp. 374–391, 1996.

[27] S. Grilli, J. Skourup, and I. Svendsen, "An efficient boundary element method for nonlinear water waves," *Engineering Analysis with Boundary Elements*, vol. 6, no. 2, pp. 97–107, 1989.

[28] S. Grilli and I. Svendsen, "Corner problems and global accuracy in the boundary element solution of nonlinear wave flows," *Engineering Analysis with Boundary Elements*, vol. 7, no. 4, pp. 178–195, 1990.

[29] I. Svendsen and S. Grilli, "Nonlinear waves on steep slopes," *Journal of Coastal Research*, vol. SI 7, pp. 185–202, 1990, special issue on rational design of mound structures.

[30] S. Grilli, R. Subramanya, I. Svendsen, and J. Veeramony, "Shoaling of solitary waves on plane beaches," *Journal of Waterway, Port, Coastal and Ocean Engineering*, vol. 120, pp. 609–628, 1994.

[31] S. Grilli and J. Horrillo, "Numerical generation and absorption of fully nonlinear periodic waves," *Journal of Engineering Mechanics*, pp. 1060–1069, 1997.

[32] S. Grilli, I. Svendsen, and R. Subramanya, "Breaking criterion and characteristics for solitary waves on slopes," *Journal of Waterway, Port, Coastal and Ocean Engineering*, vol. 123, pp. 102–112, 1997.

[33] S. Grilli and P. Watts, "Modeling of waves generated by a moving submerged body. applications to underwater landslides." *Engineering Analysis with Boundary Elements*, vol. 23, pp. 645–656, 1999.

[34] S. Grilli and J. Horrillo, "Shoaling of periodic waves over barred-beaches in a fully nonlinear numerical wave tank," *International Journal of Offshore and Polar Engineering*, vol. 9, pp. 257–263, 1999.

[35] S. Grilli, P. Guyenne, and F. Dias, "A fully nonlinear model for three-dimensional overturning waves over arbitrary bottom," *International Journal for Numerical Methods in Fluids*, vol. 35, pp. 829–867, 2001.

[36] C. Fochesato and F. Dias, "A fast method for nonlinear three-dimensional free-surface waves," in *Proceedings of the Royal Society A*, 2006, pp. 2715–2735, doi:10.1098/rspa.2006.1706.

[37] A. Subramani, R. Beck, and W. Schultz, "Suppression of wave-breaking in nonlinear water wave computations," in *13th International Workshop on Water Waves and Floating Bodies*, Alphen a/d Rijn, Netherlands, March 1998.

[38] M.S. Çelebi, "Computation of transient nonlinear ship waves using an adaptive algorithm," *Journal of Fluids and Structures*, vol. 14, pp. 281–301, 2000.

[39] H. Raven, "Inviscid calculations on ship wave making – capabilities, limitations, and prospects," in *22nd Symposium on Naval Hydrodynamics*, Washington D.C., USA, 1998.

[40] R. Cointe, "Nonlinear simulation of transient free surface flows," in *Proceedings of the Fifth International Conference on Numerical Ship Hydrodynamics*, Hiroshima, Japan, 1989, pp. 239–250.

[41] Y. Liu, M. Xue, and D. Yue, "Computations of fully nonlinear three-dimensional wave-wave and wave-body interactions. Part 2. Nonlinear waves and forces on a body." *Journal of Fluid Mechanics*, vol. 438, pp. 41–66, 2001.

[42] D. Nakos, D. Kring, and P. Sclavounos, "Rankine panel methods for transient free surface flows," in *Proceedings of the Sixth International Conference Numerical Ship Hydrodynamics*, 1993.

[43] T. Hino, "Computation of a free surface flow around an advancing ship by the Navier-Stokes equations," in *Proceedings of the Fifth International Conference on Numerical Ship Hydrodynamics*, Hiroshima, Japan, 1989.

[44] H. Sung and S. Grilli, "Numerical modeling of nonlinear surface waves caused by surface effect ships. dynamics and kinematics," in *Proceedings of the 15th Offshore and Polar Engineering Conference*. Seoul, Korea: International Society of Offshore and Polar Engineering (ISOPE05), June 2005.

[45] B. Biausser, S. Grilli, and R. Marcer, "Numerical analysis of the internal kinematics and dynamics of three-dimensional breaking waves on slopes," in *Proceedings of the 14th Offshore and Polar Engineering Conference*. International Society of Offshore and Polar Engineering (ISOPE04), 2004, pp. 247–256.

[46] P. Guyenne and S. Grilli, "Numerical study of three-dimensional overturning waves in shallow water," *Journal of Fluid Mechanics*, vol. 547, pp. 361–388, 2006.

[47] S. Grilli, S. Vogelmann, and P. Watts, "Development of a 3D Numerical Wave Tank for modeling tsunami generation by underwater landslides," *Engineering Analysis with Boundary Elements*, vol. 26, pp. 301–313, 2002.

[48] H. Sung and S. Grilli, "Combined Eulerian-Lagrangian or pseudo-Lagrangian descriptions of waves caused by an advancing free surface disturbance," in *Proceedings of the 16th Offshore and Polar Engineering Conference*. San Francisco, California: International Society of Offshore and Polar Engineering (ISOPE06), June 2006.

[49] K. Hayami and H. Matsumoto, "A numerical quadrature for newly singular boundary element integrals," *Engineering Analysis with Boundary Elements*, pp. 143–154, 1994.

[50] S. Grilli and R. Subramanya, "Quasi-singular integrals in the modeling of nonlinear water waves in shallow water," *Engineering Analysis with Boundary Elements*, vol. 13, no. 2, pp. 181–191, 1994.

[51] K. Yoshida, *Applications of Fast Multipole Method to boundary integral element method*. Ph.D. dissertation, Kyoto University, 2001.

[52] C. Fochesato, *Modelèles numériques pour les vagues et les ondes internes*. Ph.D. dissertation, Ecole Normale Superieure de Cachan, 2004.

[53] Y. Saad and H. Schultz, "GMRES: a generalized minimal residual algorithm for solving nonsymmetric linear systems," *Society for Industrial and Applied Mathematics Journal of Scientific Computation*, vol. 7, pp. 856–869, 1986.

[54] C. Fochesato, S. Grilli, and P. Guyenne, "Note on non-orthogonality of local curvilinear co-ordinates in a three-dimensional boundary element method," *International Journal for Numerical Methods in Fluids*, vol. 48, pp. 305–324, 2005.

[55] H. Sung and S. Grilli, "A note on accuracy and convergence of a third-order boundary element method for three dimensional nonlinear free surface flows," *Journal of Ships and Ocean Engineering*, vol. 40, pp. 31–41, 2005.

APPENDIX

Experimental information

A.1 IMD test matrix

Test	Date	Time	W (N)	U (m/s)	Fan (rpm)	Notes
2	21-Aug-02	19:00	?	1.5	1800	ducts fwd
3		19:05		4.5	1800	
4		19:14		4.5	1800	
5		19:23		4.5	3000	
6		19:31		9.0	3000	
7		19:40		9.0	3000	
8		19:53		9.0	4140	
9	22-Aug-02	8:40		9.0	4140	
10		8:55		9.0	3600	
11		9:35		4.5	3000	
12		9:47		9.0	4140	
RPM-2		13:48		0.0	various	
RPM-3		14:13		0.0	various	
13		14:54		2.0	4140	
14		15:00		4.0	4140	
15		15:09		6.0	4140	
16		15:22		8.0	4140	
17		15:28		9.0	4140	
18		15:56		2.0	3000	
19		16:05		4.0	3000	
20		16:13		6.0	3000	
21		16:21		8.0	3000	
RPM-4		19:59		0.0	various	ducts aft
22		20:07		2.0	3000	
23		20:25		4.0	3000	
24		20:33		6.0	3000	
25		20:40		8.0	3000	
26		20:51		9.0	3000	
RPM-5	23-Aug-02	?		0.0	various	no grasshopper
27				9.0	4140	
28				2.0	4140	
29				4.0	4140	
30				6.0	4140	
31				8.0	4140	

Test	Date	Time	W (N)	U (m/s)	Fan (rpm)	Notes
32			in air	6.0	0	with grasshopper
33			in air	?	0	
34			in air	?	0	
35			in air	?	0	
36			in air	?	0	
37			in air	?	0	
38			in air	?	0	
39			in air	?	0	
40			in air	?	0	
41			in air	?	0	
42		13:27	?	9.0	4140	ducts reinforced
43		15:05	in air	2.0	0	
44		15:12	in air	4.0	0	
45		15:17	in air	6.0	0	
46		15:29	in air	8.0	0	
47		15:35	in air	9.0	0	
48		16:08		9.0	4140	
49		16:22		8.0	4140	
50		16:30		6.0	4140	
51		16:36		4.0	4140	
52		16:43		2.0	4140	
53		18:08	133.	9.0	3000	
54		18:14	133.	8.0	3000	
55		18:19	133.	6.0	3000	
56		18:27	133.	4.0	3000	
57		18:33	133.	2.0	3000	
58		19:15	445.	2.0	4140	bow up
59		19:21	445.	2.0	4140	bow up
60		19:32	445.	9.0	4140	bow up
61		19:38	445.	4.0	4140	bow up
62		19:44	445.	6.0	4140	bow up
63		19:51	445.	8.0	4140	bow up
64	24-Aug-02	9:21	445.	9.0	4140	
65		9:29	445.	8.0	4140	
66		9:37	445.	6.0	4140	
67		9:45	445.	4.0	4140	
68		9:55	445.	2.0	4140	
69		10:02	445.	7.0	4140	
70		10:09	445.	5.0	4140	
71		10:25	445.	2.0	3000	
72		10:36	445.	9.0	3000	

Test	Date	Time	W (N)	U (m/s)	Fan (rpm)	Notes
73		10:42	445.	8.0	3000	
74		10:48	445.	6.0	3000	
75		10:53	445.	4.0	3000	
76		10:59	445.	7.0	3000	
77		11:06	445.	8.0	2400	
78		11:14	445.	6.0	2400	
79		11:20	445.	4.0	2400	
80		11:24	445.	2.0	2400	
81		11:42	445.	9.0	4140	same as 64
82		11:49	445.	9.0	4140	same as 81
83		12:23	356.	8.0	4140	
84		12:28	356.	6.0	4140	
85		12:34	356.	4.0	4140	
86		12:41	356.	8.0	3000	
87		12:46	356.	6.0	3000	
88		12:52	356.	4.0	3000	
89		13:01	356.	8.0	2400	
90		13:06	356.	6.0	2400	
91		13:14	356.	4.0	2400	
92		13:18	356.	8.0	4140	same as 83
93		13:48	289.	8.0	4140	
94		13:52	289.	6.0	4140	
95		13:59	289.	4.0	4140	
96		14:03	289.	2.0	4140	
98		14:17	289.	9.0	4140	
99		14:27	289.	9.0	4140	
100		14:42	289.	9.0	4140	bow down
101		14:56	289.	8.0	3000	
102		15:07	289.	6.0	3000	
103		15:13	289.	4.0	3000	
104		15:19	289.	8.0	2400	
105		15:25	289.	6.0	2400	
106		15:29	289.	4.0	2400	
107		16:13	in air	various	0	

A.2 Photos of IMD test setup

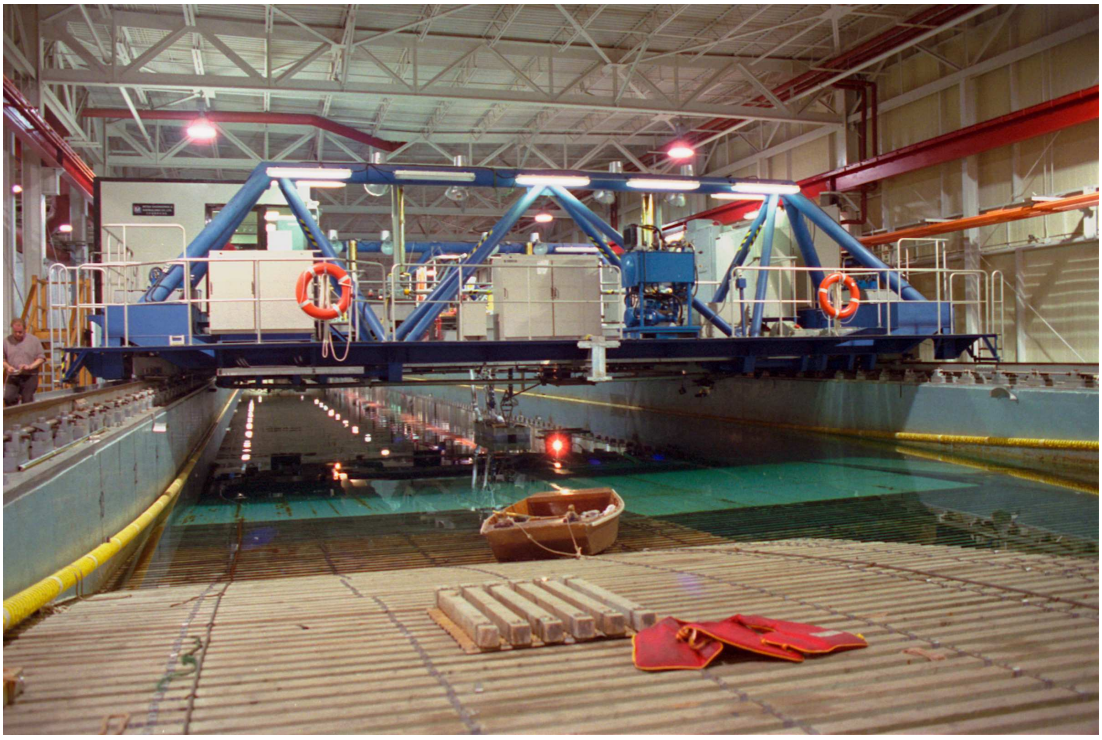

Figure A.1. Tow carriage used at IMD. Note model attached underneath.

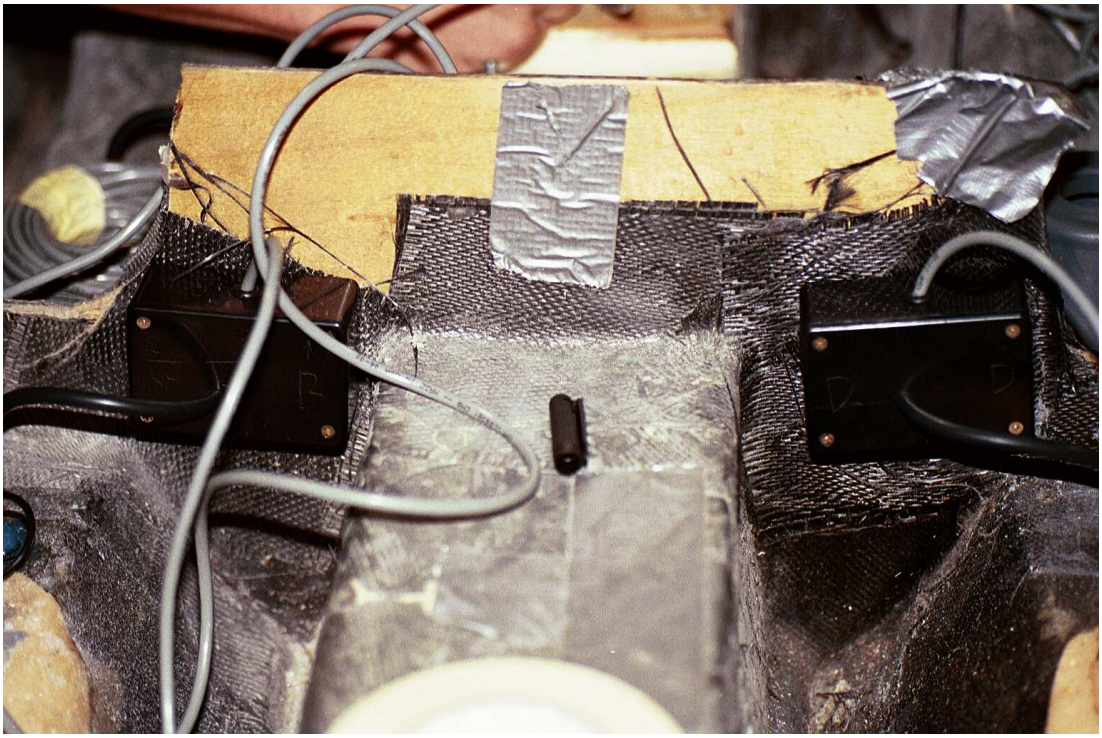

Figure A.2. Close-up of pressure sensor attachment on 2.3 m model. Sensors are within the black boxes, electrical cabling is grey, and the pressure sensors are connected to pressure ports on the model with the black tubing.

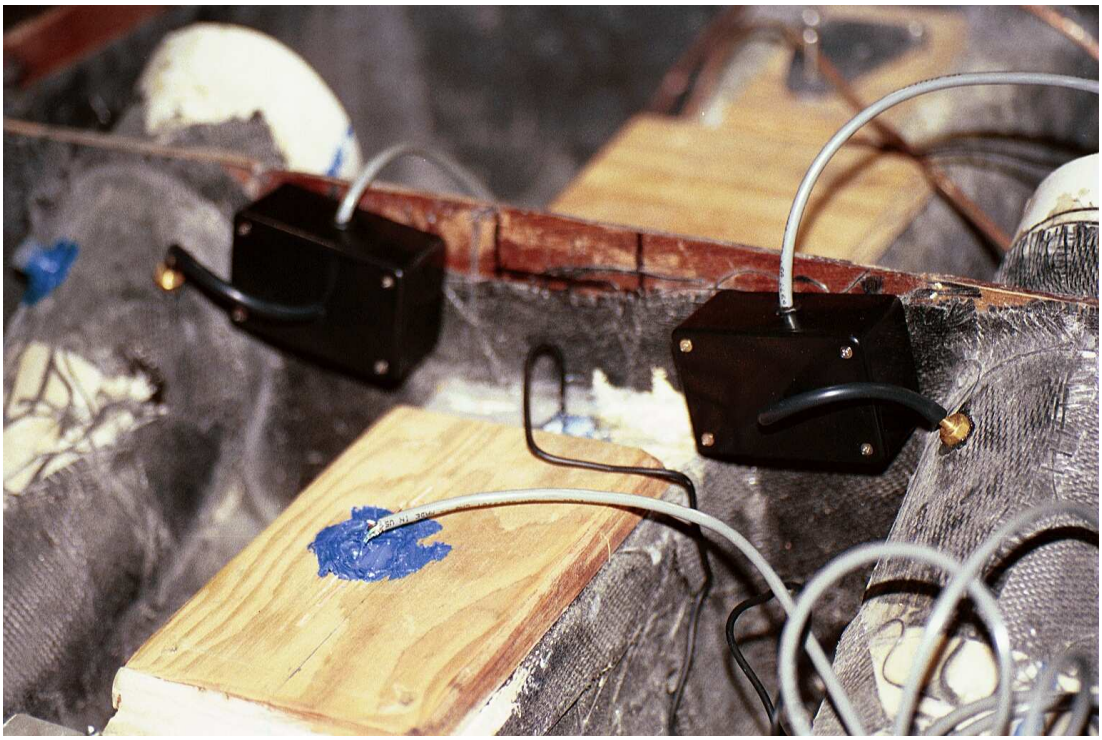

Figure A.3. Close-up of the pressure sensor attachment on 2.3 m model. Sensors are within the black boxes, electrical cabling is grey, and the pressure sensors are connected to pressure ports on the model with the black tubing. Notice the cushion inlets without the attached ducting on each side.

Figure A.4. Stern view of the 2.3 m model, with lines marking draft. Note the grasshopper attachment amidships, and the cord attached in the corners to help pick up the model for adjustments.

Figure A.5. Close-up of the starboard bow of the 2.3 m model, with lines marking draft, and numbering indicating distance from the bow. Note the ducting attached (top) and the cord attached in the corner to help pick up the model for adjustments (top right).

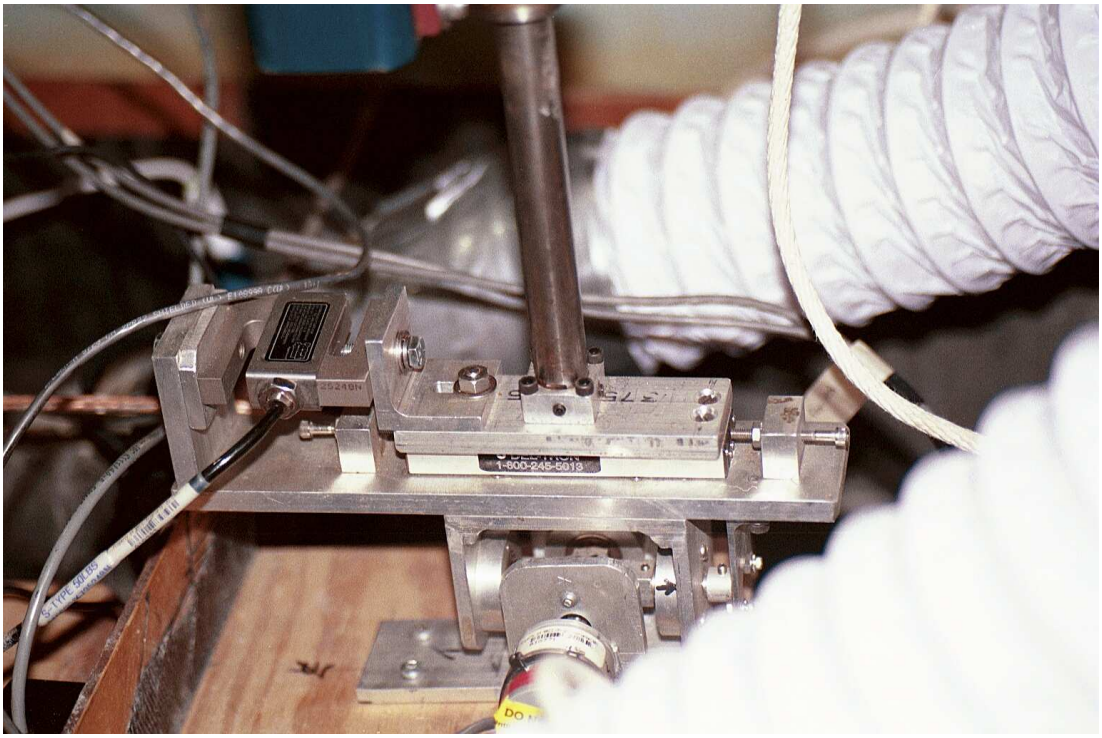

Figure A.6. Close-up of the tow mount, with sensors to measure trim, roll, sinkage, and tow force. Note flexible ducting attached to air cushion inlets.

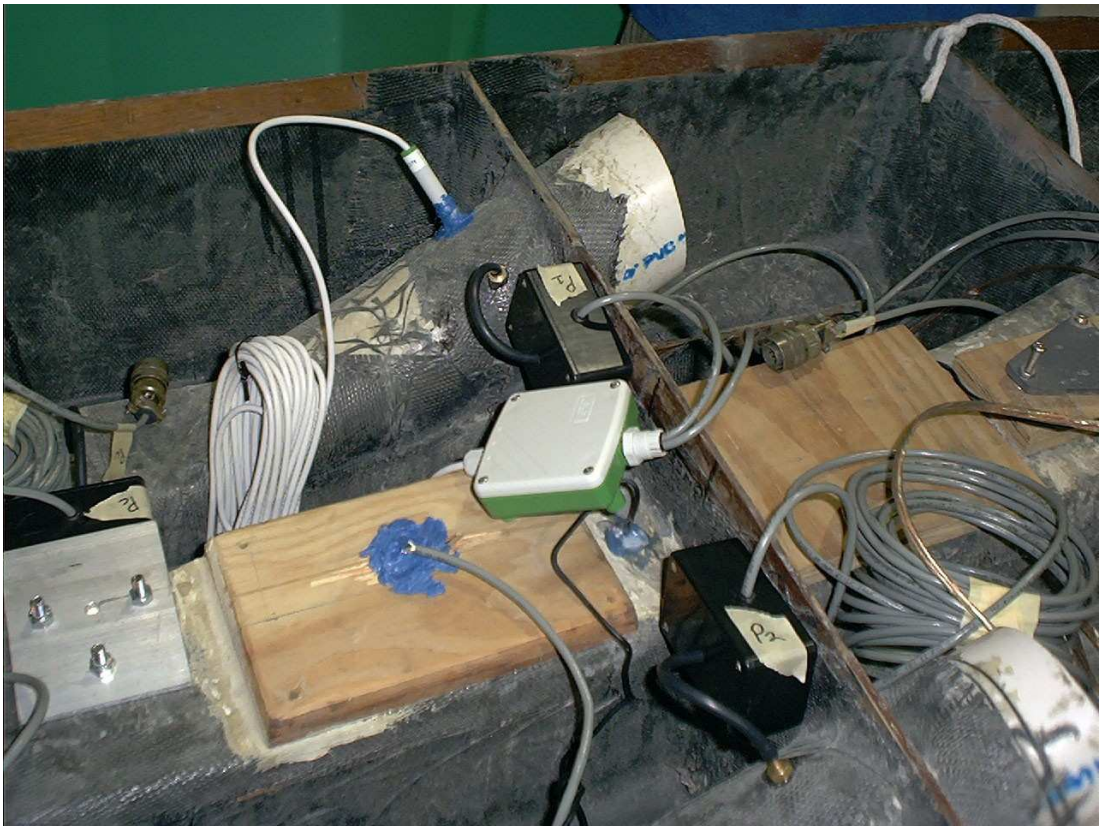

Figure A.7. View of the sensors used at the bow, including a hot film anemometer attached to the port air cushion inlet, and pressure sensors P_1, P_2, and P_c. Note the plate used for attaching the tow mount (right).

Figure A.8. View of the sensor setup of the 2.3 m model, including pressure sensors P_1, P_2, P_c, as well as the installation point for the range finder (bottom left). Note the air cushion inlets are not attached to ducting (top right).

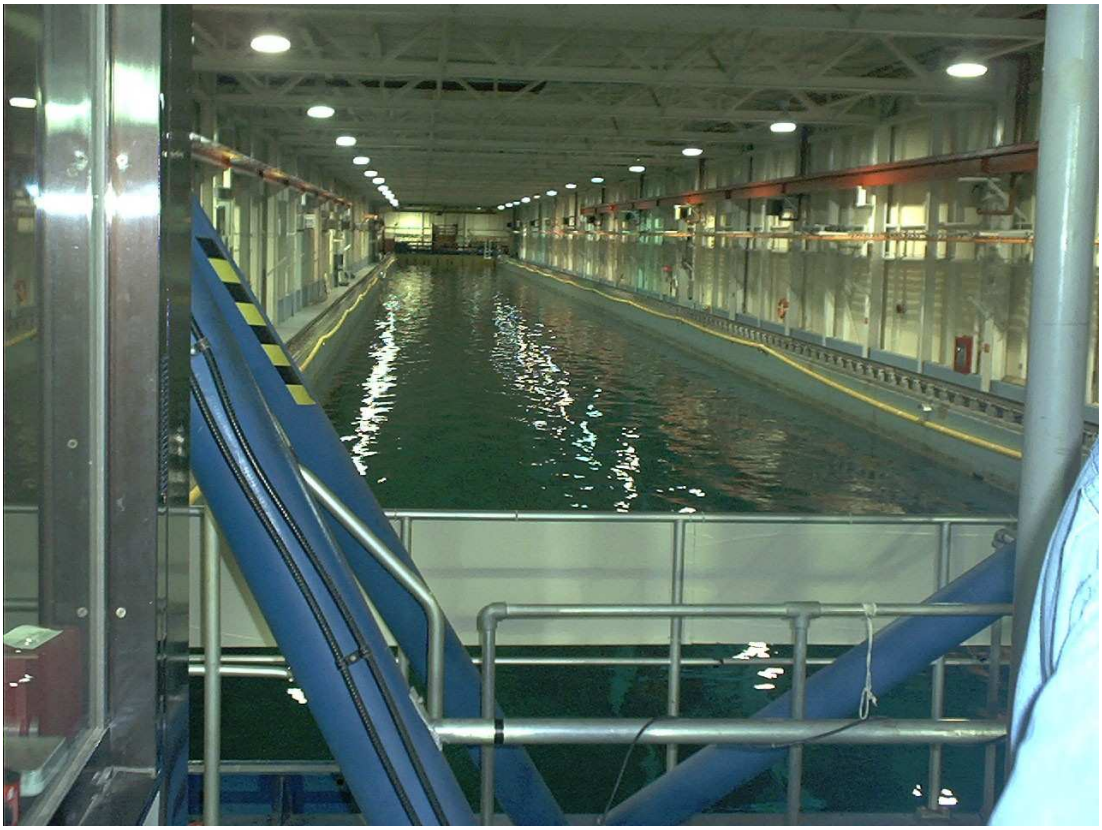

Figure A.9. View of the 200 m Clearwater towing tank at IMD from the tow carriage.

Figure A.10. Measurement of the model weight (foreground). Note the lab setup for data acquisition (background).

Figure A.11. 2.3 m model in position underneath the tow carriage. Note the ducting between the blower (not seen) and the air cushions.

Figure A.12. Front view of the 2.3 m model, with tow mount, air cushion ducting, pressure sensors, and range finder attached. Note the model is being held out of the water by cord attached to the four corners of the model.

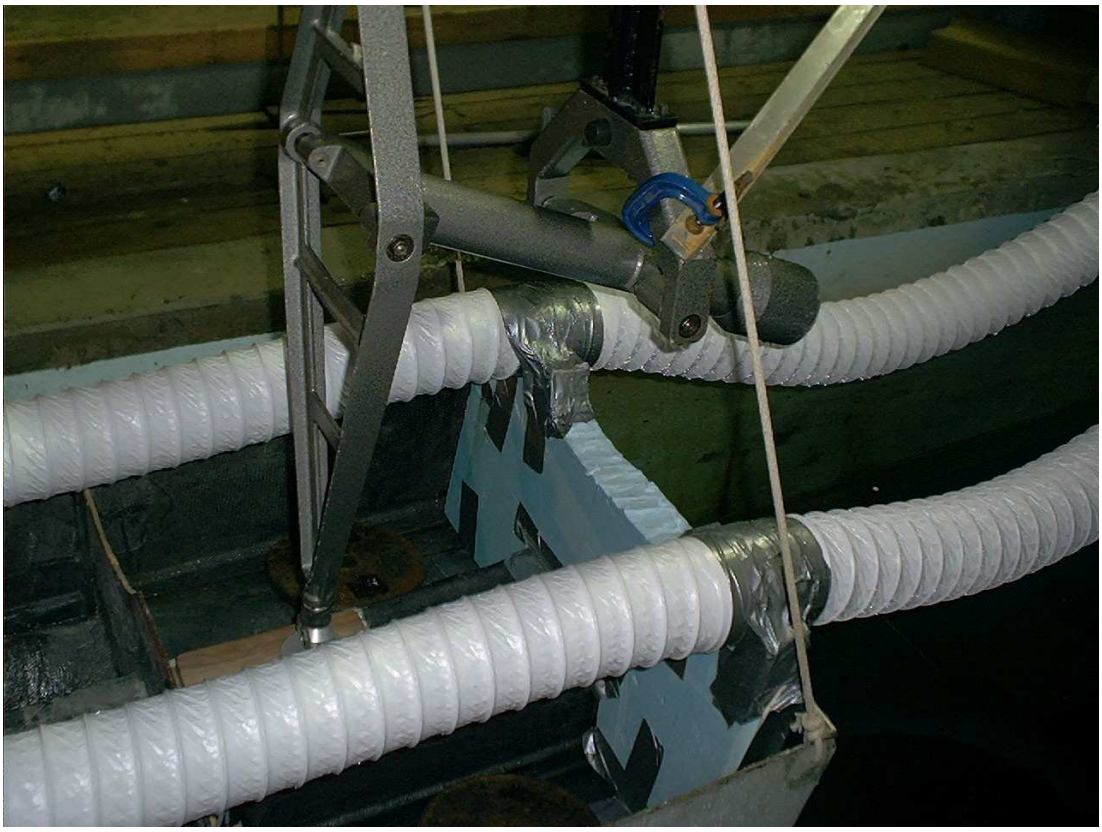

Figure A.13. Rear view of the 2.3 m model, with air cushion ducting and grasshopper attached.

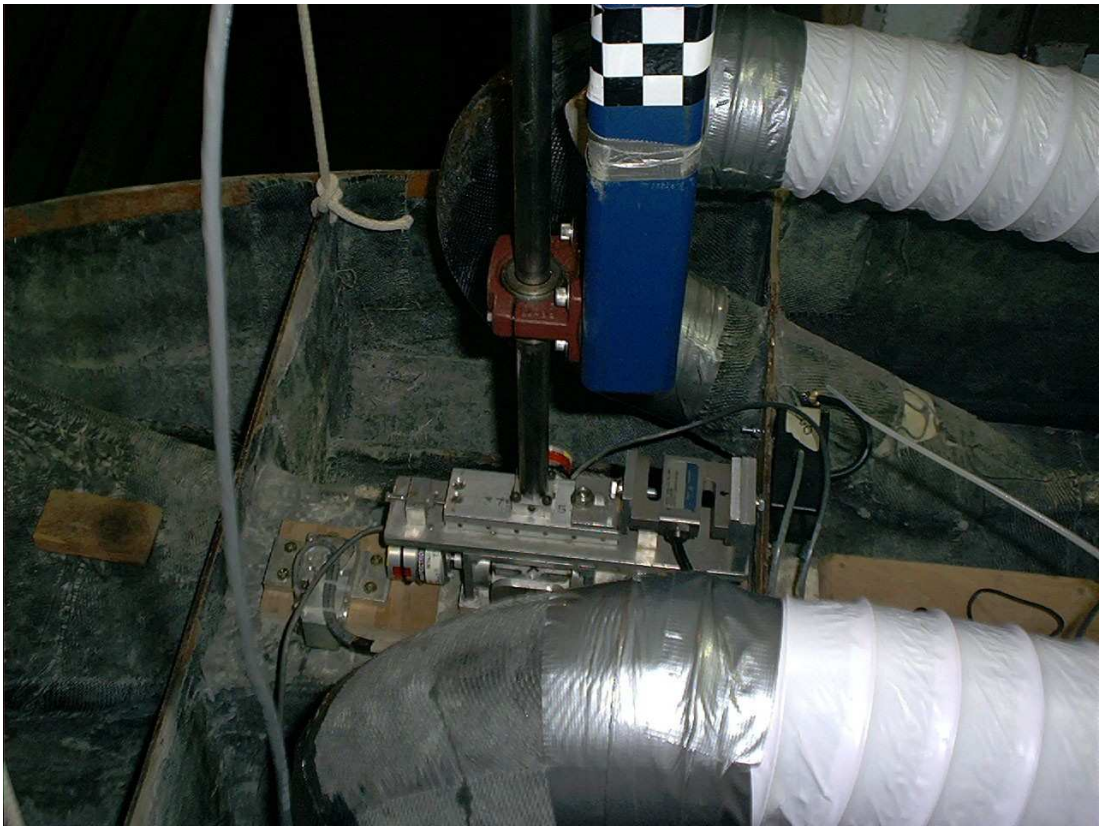

Figure A.14. Close up of tow mount an air cushion ducting attachment.

Figure A.15. Top view of model from tow carriage, showing how the ducting reaches between the blower (not seen, bottom right), and the model (top left).

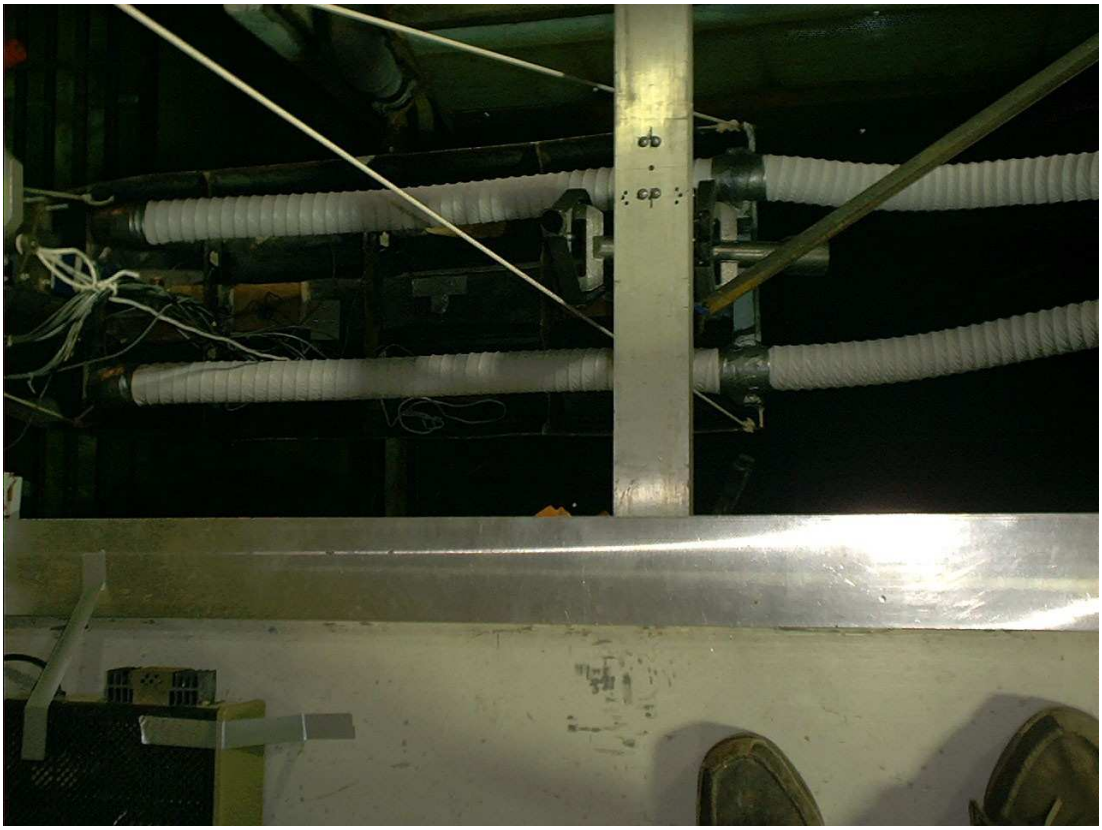

Figure A.16. Top view of 2.3 m model, showing instrument cabling (left), and air cushion ducting.

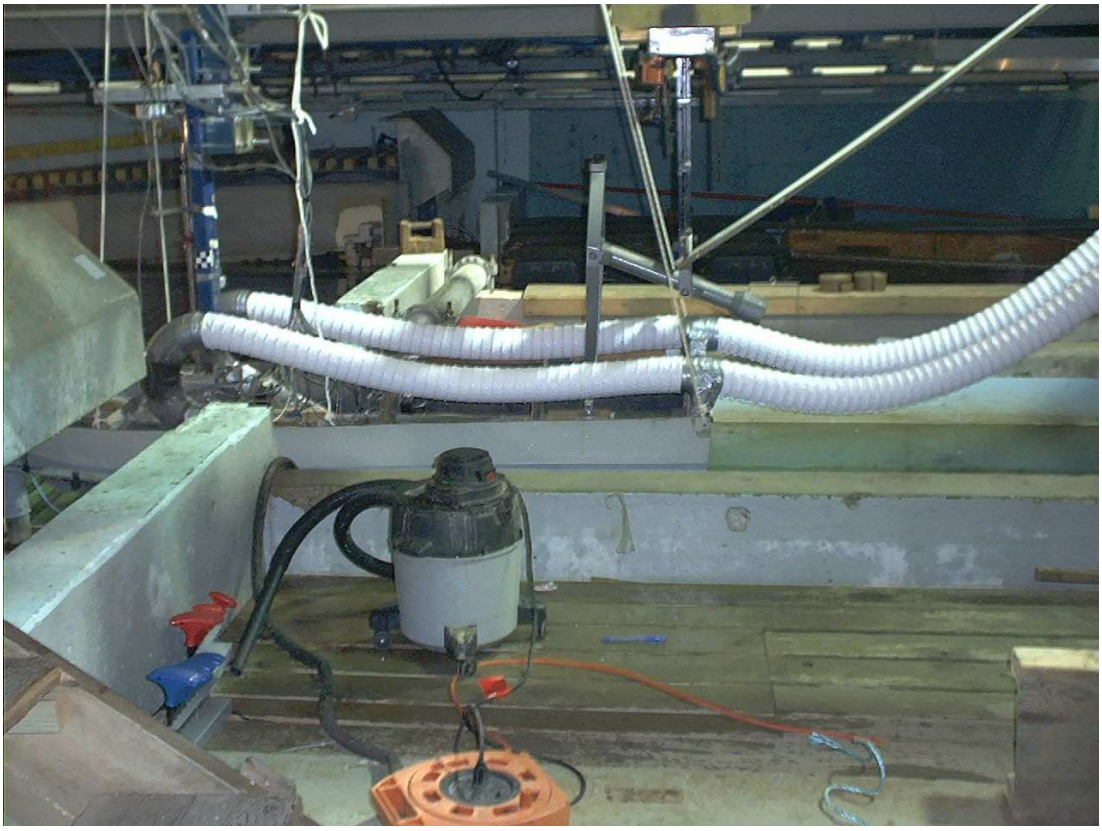

Figure A.17. Side view of model setup used during tests considered in manuscript, with air cushion ducting aft.

A.3 Photos of *Gladius* construction

A plug and mold construction technique was used to make the 25 m (82 ft) composite hull of the *Gladius* in 2004 (Figs. A.20,A.21,A.22,A.23,A.24).

Figure A.18. Close up of tow mount and instrument cabling between model and tow carriage.

Figure A.19. Side view of model setup used in early tests not considered in manuscript, where air cushion ducting was attached from the bow. Note tow mount (left), instrument cabling (center), and grasshopper (right).

Figure A.20. Fore end of the wooden frame (i.e., plug) for building a demihull of the *Gladius*.

Figure A.21. Fore end of the wooden frame (i.e., plug) for building a demihull of the *Gladius* (center), and aft end of the mold (bottom).

Figure A.22. Fore end of the wooden frame (i.e., plug) for a demihull of the *Gladius*.

Figure A.23. Fore end of the wooden frame (i.e., plug) for a demihull of the *Gladius* (foreground), and resulting mold (right background).

Figure A.24. Close-up of part of the wooden frame (i.e., plug) for a demihull of the *Gladius*.

BIBLIOGRAPHY

B. Allenström and H. Liljenberg and U. Tudem, "An airlifted catamaran – hydrodynamical aspects," in *International Conference of Fast Sea Transportation (FAST 2001)*. Southampton, UK: Royal Institution of Naval Architects, Sept 2001.

Bebar, M. and Liberatore, D., *U.S. Navy high performance ship concept formulation*. American Institute of Aeronautics and Astronautics, 1983, no. 626.

Bengston, A., *Laboratory experiments to determine the dynamic response of a ship-to-shore causeway system*. Master's thesis, University of Rhode Island, 2001.

Bertin, D., Bittanti, S., and Savaresi, S., "Decoupled cushion control in ride control systems for air cushion catamarans," *Control Engineering Practice*, vol. 8, pp. 191–203, 2000.

Biausser, B., Grilli, S., and Marcer, R., "Numerical analysis of the internal kinematics and dynamics of three-dimensional breaking waves on slopes," in *Proceedings of the 14th Offshore and Polar Engineering Conference*. International Society of Offshore and Polar Engineering (ISOPE04), 2004, pp. 247–256.

Bradley, C., *Surface effect ship air cavity pressure gauges*. David Taylor Naval Ship R&D Center, July 1981, no. DTNSRDC/CID-81/1.

Butler, E., "The surface effect ship," *Naval Engineers Journal*, vol. 97, pp. 200–260, 1985.

Chung, J., "Skirt-material damping effects on heave dynamics of an air-cushion-vehicle bag-and-finger skirt," *Canadian Aeronautics and Space Journal*, vol. 48, no. 3, pp. 201–212, 2002.

Cointe, R., "Nonlinear simulation of transient free surface flows," in *Proceedings of the Fifth International Conference on Numerical Ship Hydrodynamics*, Hiroshima, Japan, 1989, pp. 239–250.

Dawson, C., "A practical computer method for solving ship-wave problems," in *Proceedings of the Second International Conference on Numerical Ship Hydrodynamics*, Berkeley, CA, USA, 1977, pp. 30–38.

Doctors, L. and Sharma, S., "The wave resistance of an air-cushion vehicle in steady and accelerated motion," *Journal of Ship Research*, vol. 16, pp. 248–260, 1972.

Durkin, J. and Paraskevas, N., *Progress in the development of the surface effect catamaran (SECAT)*. American Institute for Aeronautics and Astronautics, 1986, no. 2364.

Fochesato, C., *Modelèles numériques pour les vagues et les ondes internes*. Ph.D. dissertation, Ecole Normale Superieure de Cachan, 2004.

Fochesato, C. and Dias, F., "A fast method for nonlinear three-dimensional free-surface waves," in *Proceedings of the Royal Society A*, 2006, pp. 2715–2735, doi:10.1098/rspa.2006.1706.

Fochesato, C., Grilli, S., and Guyenne, P., "Note on non-orthogonality of local curvilinear co-ordinates in a three-dimensional boundary element method," *International Journal for Numerical Methods in Fluids*, vol. 48, pp. 305–324, 2005.

G. Jensen and V. Bertram and H. Söding, "Ship wave-resistance computations," in *Proceedings of the Fifth International Conference on Numerical Ship Hydrodynamics*, Hiroshima, Japan, 1989.

Greengard, L. and Rokhlin, V., "A fast algorithm for particle simulations," *Journal of Computational Physics*, vol. 73, pp. 325–348, 1987.

Grilli, S., Guyenne, P., and Dias, F., "A fully nonlinear model for three-dimensional overturning waves over arbitrary bottom," *International Journal for Numerical Methods in Fluids*, vol. 35, pp. 829–867, 2001.

Grilli, S. and Horrillo, J., "Numerical generation and absorption of fully nonlinear periodic waves," *Journal of Engineering Mechanics*, pp. 1060–1069, 1997.

Grilli, S. and Horrillo, J., "Shoaling of periodic waves over barred-beaches in a fully nonlinear numerical wave tank," *International Journal of Offshore and Polar Engineering*, vol. 9, pp. 257–263, 1999.

Grilli, S., Skourup, J., and Svendsen, I., "An efficient boundary element method for nonlinear water waves," *Engineering Analysis with Boundary Elements*, vol. 6, no. 2, pp. 97–107, 1989.

Grilli, S. and Subramanya, R., "Quasi-singular integrals in the modeling of nonlinear water waves in shallow water," *Engineering Analysis with Boundary Elements*, vol. 13, no. 2, pp. 181–191, 1994.

Grilli, S. and Subramanya, R., "Numerical modeling of wave beraking induced by fixed or moving boundaries," *Computational Mechanics*, vol. 17, pp. 374–391, 1996.

Grilli, S., Subramanya, R., Svendsen, I., and Veeramony, J., "Shoaling of solitary waves on plane beaches," *Journal of Waterway, Port, Coastal and Ocean Engineering*, vol. 120, pp. 609–628, 1994.

Grilli, S. and Svendsen, I., "Corner problems and global accuracy in the boundary element solution of nonlinear wave flows," *Engineering Analysis with Boundary Elements*, vol. 7, no. 4, pp. 178–195, 1990.

Grilli, S., Svendsen, I., and Subramanya, R., "Breaking criterion and characteristics for solitary waves on slopes," *Journal of Waterway, Port, Coastal and Ocean Engineering*, vol. 123, pp. 102–112, 1997.

Grilli, S., Vogelmann, S., and Watts, P., "Development of a 3D Numerical Wave Tank for modeling tsunami generation by underwater landslides," *Engineering Analysis with Boundary Elements*, vol. 26, pp. 301–313, 2002.

Grilli, S. and Watts, P., "Modeling of waves generated by a moving submerged body. applications to underwater landslides." *Engineering Analysis with Boundary Elements*, vol. 23, pp. 645–656, 1999.

Guyenne, P. and Grilli, S., "Numerical study of three-dimensional overturning waves in shallow water," *Journal of Fluid Mechanics*, vol. 547, pp. 361–388, 2006.

Harley, H., "Surface effect vessel hull," U.S. Patent 5 570 650, 1996.

Havelock, T., "Wave resistance," in *Proceedings of the Royal Society of London*, vol. A118, 1928, pp. 24–33.

Hayami, K. and Matsumoto, H., "A numerical quadrature for newly singular boundary element integrals," *Engineering Analysis with Boundary Elements*, pp. 143–154, 1994.

Hess, J. and Smith, A., "Calculation of nonlinear potential flow about arbitrary three-dimensional bodies," *Journal of Ship Research*, vol. 8, no. 2, pp. 22–44, 1964.

Hino, T., "Computation of a free surface flow around an advancing ship by the Navier-Stokes equations," in *Proceedings of the Fifth International Conference on Numerical Ship Hydrodynamics*, Hiroshima, Japan, 1989.

Huang, Y. and Sclavounos, P., "Nonlinear ship motions," *Journal of Ship Research*, vol. 42, pp. 120–130, 1998.

"Testing and extrapolation methods high speed marine vehicles resistance test," International Towing Tank Conference Recommended Procedures 7.5-02-05-01, 2002.

Janson, C.-E., *Potential flow panel methods for the calculation of free-surface flows with lift*. Göteborg, Sweden: Ph.D. dissertation, Chalmers Univ., 1997.

K. Knüpffer and J.C. Frambourg and J.C. Lewthwaite and J.D. Adams, *The Federal Republic of Germany's fast test craft*. American Institute of Aeronautics and Astronautics, 1989, no. 89-1471-CP.

Latorre, R., Miller, A., and Philips, R., "Micro-bubble resistance reduction for high speed craft," *Society of Naval Architects and Marine Engineers Transactions*, vol. 110, pp. 259–277, 2002.

Legner, H., "A simple model for gas bubble drag reduction," *Physics of Fluids*, vol. 27, no. 12, pp. 2788–2790, December 1984.

Liu, Y., Xue, M., and Yue, D., "Computations of fully nonlinear three-dimensional wave-wave and wave-body interactions. Part 2. Nonlinear waves and forces on a body." *Journal of Fluid Mechanics*, vol. 438, pp. 41–66, 2001.

Longuet-Higgins, M. and Cokelet, E., "The deformation of steep surface waves on water. i. a numerical method of computation." in *Proceedings of the Royal Society of London*, vol. A350, 1976, pp. 1–26.

M. Xue and H. Xü and Y. Liu and D.K.P. Yue, "Computations of fully nonlinear three-dimensional wave-wave and wave-body interactions. part 1. dynamics of steep three-dimensional waves." *Journal of Fluid Mechanics*, vol. 438, pp. 11–39, 2001.

Madavan, N., Deutsch, S., and Merkle, C., "Reduction of turbulent skin friction by microbubbles," *Physics of Fluids*, vol. 27, no. 2, pp. 356–363, February 1984.

Mantle, P., "Development of the USN surface effect ship, SES-100B," *Naval Engineers Journal*, vol. 85, no. 5, pp. 65–77, October 1973.

Mantle, P., *Air cushion craft development*. David Taylor Naval Ship Research and Development Center, 1980, no. 80/012.

McKesson, C. B., "Hull form and propulsor technology for high speed sealift," in *High-Speed Sealift Technology Workshop*. Center for the Commercial Deployment of Transportation Technology, 1998.

Michell, J., "The wave resistance of a ship," *Philosophical Magazine*, vol. 45, pp. 106–123, 1898, series 5.

Moulijn, J., *Scaling of air cushion dynamics*. Delft University of Technology, July 1998, no. Report 1151, Project Code 961.

M.S. Çelebi, "Computation of transient nonlinear ship waves using an adaptive algorithm," *Journal of Fluids and Structures*, vol. 14, pp. 281–301, 2000.

Nakos, D., Kring, D., and Sclavounos, P., "Rankine panel methods for transient free surface flows," in *Proceedings of the Sixth International Conference Numerical Ship Hydrodynamics*, 1993.

Newman, J., "Evaluation of the wave-resistance green function: Part 1 – the double integral," *Journal of Ship Research*, vol. 31, pp. 79–90, 1987.

Raven, H., "Inviscid calculations on ship wave making – capabilities, limitations, and prospects," in *22nd Symposium on Naval Hydrodynamics*, Washington D.C., USA, 1998.

Ritter, O. and Templeman, M., *High-speed sealift technology Volume 1*. Carderock Division Naval Surface Warfare Center, September 1998, no. CDNSWC-TSSD-98-009, technology Projection Report.

Saad, Y. and Schultz, H., "GMRES: a generalized minimal residual algorithm for solving nonsymmetric linear systems," *Society for Industrial and Applied Mathematics Journal of Scientific Computation*, vol. 7, pp. 856–869, 1986.

Scorpio, S., *Fully nonlinear ship-wave computations using a multipole accelerated desingularized method*. Ann Arbor: Ph.D. dissertation, University of Michigan, 1997.

Sen, D., "Numerical simulation of motions of two-dimensional floating bodies," *Journal of Ship Research*, vol. 37, pp. 307–330, 1993.

Sen, D., Pawlowski, J., Lever, J., and Hinchey, M., "Two-dimensional numerical modelling of large motions of floating bodies in waves," in *Proceedings of the Fifth International Conference of Numerical Ship Hydrodynamics*, Hiroshima, Japan, 1989, pp. 351–373.

"The surface effect ship: advanced design and technology," Prepared for the Surface Effect Ship Program Office, PM-17, 1974.

Shultz, M., *Simulation of a ship-to-shore causeway system in waves*. Master's thesis, University of Rhode Island, 2005.

Skolnick, A., "Transoceanic surface effect ships," in *Proceedings of the Institute of Electrical and Electronics Engineers*, vol. 56, no. 4, 1968, pp. 700–712.

Subramani, A., Beck, R., and Schultz, W., "Suppression of wave-breaking in nonlinear water wave computations," in *13th International Workshop on Water Waves and Floating Bodies*, Alphen a/d Rijn, Netherlands, March 1998.

Sung, H. and Grilli, S., "A note on accuracy and convergence of a third-order boundary element method for three dimensional nonlinear free surface flows," *Journal of Ships and Ocean Engineering*, vol. 40, pp. 31–41, 2005.

Sung, H. and Grilli, S., "Numerical modeling of nonlinear surface waves caused by surface effect ships. dynamics and kinematics," in *Proceedings of the 15th Offshore and Polar Engineering Conference*. Seoul, Korea: International Society of Offshore and Polar Engineering (ISOPE05), June 2005.

Sung, H. and Grilli, S., "Combined Eulerian-Lagrangian or pseudo-Lagrangian descriptions of waves caused by an advancing free surface disturbance," in *Proceedings of the 16th Offshore and Polar Engineering Conference*. San Francisco, California: International Society of Offshore and Polar Engineering (ISOPE06), June 2006.

Svendsen, I. and Grilli, S., "Nonlinear waves on steep slopes," *Journal of Coastal Research*, vol. SI 7, pp. 185–202, 1990, special issue on rational design of mound structures.

Tuck, E., Scullen, D., and Lazauskas, L., "Wave patterns and minimum wave resistance for high-speed vessels," in *Proceedings of the 24th Symposium on Naval Hydrodynamics*, Kukuoka, Japan, 2002.

Tudem, U., Eilertsen, A., Eide, J. G., Liljenberg, H., and Lindholm, M., "Design development of 24 m air supported vessel (ASV) catamaran demonstrator, suitable for fast passenger ferries and various naval / paramilitary applications," in *High Speed Craft: Design & Operation*. London, UK: Royal Institution of Naval Architects, 2004.

von Mises, R., *Theory of Flight*. Dover Publishing, 1959.

Wessel, J., "Review on German SES developments and the government funded R+D programme SUS C," in *Proceedings of the International Conference on Fast Sea Transportation (FAST 1995)*, vol. 12, 1995, pp. 917–930.

Wilson, F. and Viars, P., *The surface effect catamaran - a sea capable small ship*. American Institute of Aeronautics and Astronautics, 1981, no. 2076.

Wilson, F., Viars, P., and Adams, J., *Feasibility design for a surface effect catamaran corvette escort*. American Institute of Aeronautics and Astronautics, 1983, no. 619.

Wilson, F., Viars, P., and Adams, J., "Surface effect catamaran – progress in concept assessment," *Naval Engineering Journal*, vol. 95, no. 3, pp. 301–311, May 1983.

Yoshida, K., *Applications of Fast Multipole Method to boundary integral element method*. Ph.D. dissertation, Kyoto University, 2001.

Yun, L. and Bliault, A., *Theory and design of air cushion craft*. John Wiley and Sons, 1999.